UNIVERSITY OF OKLAHOMA

GRADUATE COLLEGE

EXAMINING SEISMIC AMPLITUDE RESPONSES OF GASEOUS MEDIA USING UNSUPERVISED MACHINE LEARNING

A THESIS

SUBMITTED TO THE GRADUATE FACULTY

in partial fulfillment of the requirements for the

Degree of

MASTER OF SCIENCE

By

JULIAN CHENIN

Norman, Oklahoma

2020

EXAMINING SEISMIC AMPLITUDE RESPONSES OF GASEOUS MEDIA USING UNSUPERVISED MACHINE LEARNING

A THESIS APPROVED FOR THE

SCHOOL OF GEOSCIENCES

BY THE COMMITTEE CONSISTING OF

_____

Dr. Heather Bedle, Chair

_____

Dr. Kurt J. Marfurt

_____

Dr. Megan E. Elwood Madden

To my family and friends like family

ACKNOWLEDGEMENTS

These past two years have been a life-changing journey filled with lessons and most importantly, plenty of joy. These experiences, lessons, and growth could not have been possible without the amazing people that I have met along the way. I would like to begin by thanking my committee members, Dr. Heather Bedle, Dr. Kurt J. Marfurt and Dr. Megan E. Elwood-Madden, for all of their valuable guidance and insights throughout these projects. You taught have taught me so much within the realm of geosciences and my research could not have been possible with you all.

Next, I would like to express my sincerest gratitude to my friends and mentors within the Attribute Assisted Seismic Processing and Interpretation (AASPI) and the Subsurface Detective Agency (SDA) research groups. The amount of care, knowledge, and brilliance within these groups has been a humbling experience. You have all taught me more than I could have imagined and consider you all to be my second family.

To my mom, late father and brother Sebastien, I thank you for all of your love and for being my biggest supporters. Dad, you were my biggest inspiration and kindled my love for the geosciences as a child. I continue to cherish those memories of classifying minerals together, working on different projects and creating music. You truly gave me the world. While you may not be able to read this thesis, I know that I have made you proud while you read this from the skies above. To Farah, Sarah and Amani, I cannot thank you enough for being part of my family and for looking after us. You all mean the world to me and are the biggest reason why I could accomplish this chapter in my life. I love you all so dearly and cannot wait to begin writing the next chapter in my life with you all.

I would like to express my sincerest gratitude to my advisor, one of my biggest mentors and role models, Dr. Heather Bedle, for her amazing support, guidance and patience. There are no words that can express my sincerest gratitude for everything that you have given me. Meeting you at the University of Houston was one of the luckiest things that could have happened for me. The opportunity to have studied under you has taught me many life lessons and made me a better scientist. For that, I cannot thank you enough and will forever cherish these valuable memories and lessons.

To my mentors, thank you for your deeply appreciated advice and insights as I started this chapter and continue with the next. Without you, I would not have been able to pursue these many opportunities. I would like to also thank the many talented scientists at OXY and Bluware for teaching me many valuable lessons and giving me the opportunity to further hone my skills. Those were unforgettable summers and I will cherish them as I progress through my professional career.

Thank you to the University of Oklahoma for great memories and amazing friends that you have given me. You were there for me at every corner and through all of the highs and lows. So, thank you Clayton Silver, Roberto Clairmont, Hope Williams, Hannah Morgan, Abidin Caf, David Lubo, Dallas Cook, Sheridan Mullen, Brittney Tamborello, Karelia La Marca Molina (BPE), Javier Tellez, Alex Vera Arroyo, Laura Ortiz, Jordan Renner, Ryan Forrest, Mike Miller, Desiree Hullaster, Raymond Ng, Folarin Kolawole, Juan Camilo Acosta, and Jacob Clements. Thank you for your unconditional love, being there for me and for being you. I would also like to thank the wonderful staff and faculty within the School of Geosciences for their professional help and guidance. Thank you Dr. Pranter, Rebecca Fay, Leah Moser, Ginger Leivas, and Ashley Tullius.

Finally, I would like to thank my childhood friends and those from the University of Houston. Without you all, I would have never been ready to tackle this challenge. Thank you to Josh Binder, Garret Guarino, Michael Massey, Gabriel Griffard, Adrian Leonard, Adrien Lhemann, Michel Farhat, Marie Farhat, Hank Harrison, Bernd Faveere, Alex White, David Lankford-Bravo, Maziar Zarea, Benjamin Lartigue, Dorian Buijse, Carolina Ramon-Duenas, Jordan Dickenson, Rym Benchaabane, David Olivas Jr., Jon Solomon, Sean Jackson, Brooke Davis, Philip Jefferson, Yilhak Abebe, Kamlpret Kaur, Patricia Martinez, Blake Heckman, Guillermo Gonzalez, and Alex Banh. This truly could not have been possible without all of you.

Cheers to the next chapter in my life and I cannot wait for what the future holds!

TABLE OF CONTENTS

LIST OF FIGURES

LIST OF TABLES

ABSTRACT

The presence of gas in the rock's or sediment's pore space significantly affects its seismic amplitude response and modifies its subsurface signature. Gas hydrates in the subsurface are often difficult to image with reflection seismic data if the seismic data lack a strong bottom simulating reflector (BSR). High-amplitude BSRs are caused by a sharp decrease in acoustic impedance in the rocks as the hydrates transition from their solid form, to a free gas form due to changing pressure and temperature conditions with depth beneath the seafloor. Two key reasons for weak BSRs include 1) insufficient free gas below the hydrate to create the needed impedance contrast, and 2) stratigraphy-parallel BSRs that are subtle and can only be identified with advanced seismic analysis. In these cases, the imaging and detection of hydrates becomes difficult, as traditional detection methods rely heavily on BSRs, gas chimneys, or pockmarks on the seafloor and other contextual components. Additionally, differentiating between low-saturation gas (LSG) and high-saturation gas (HSG) reservoirs remains another subsurface imaging issue, as they will have similar seismic amplitude and rock physics responses.

To address and understand these challenging imaging problems, I employ an unsupervised machine learning multi-attribute analysis to reduce their significant uncertainty in hydrocarbon exploration. The hydrate study looks at two 2D seismic datasets in the Pegasus Basin, offshore New Zealand, where BSRs are not continuously or clearly imaged. The first LSG investigates the amplitude responses within the King Kong/Lisa Anne and Ursa producing fields within the deepwater Gulf of Mexico and within the Scarborough gas field, offshore Australia. These analyses use principal component analysis (PCA) methods applied to a selected set of seismic attributes to identify meaningful combinations of attributes which provide insight into the seismic data. I then use self-organizing maps (SOMs) to help visualize and interpret the multi-dimensional

PCA results. Several SOM hyperparameters were tested such as neuron count and the number of epochs (iterations) to create an optimized SOM that is computationally efficient, and effectively identifies the features of interest.

Optimized SOM results, which use a combination of attributes sensitive to attenuation, frequency, and small amplitude anomalies, help better resolve subtle hydrate response and can differentiate between LSG and HGS reservoirs. However, this method only proved to be successful within the Gulf of Mexico data volume and yielded disappointing results with the Carnarvon Basin. This difference is most likely due to the Carnarvon Basin having a different amplitude response resulting from a different burial history and fluid saturations than that of the Gulf of Mexico. Therefore, this method is non-transferrable, and a different combination of attributes may be needed in other LSG-prone basins.

Individually, some of these attributes have minimal success in identifying the seismically invisible hydrates and differentiating between low and high gas saturation reservoirs. However, when used together by employing multi-attribute analyses such as PCA and SOMs, these same attributes provide clearer insight into the subsurface responses needed to better identify the presence of hydrates and to distinguish between both reservoirs.

CHAPTER 1: Introduction

Over the last few years, machine learning techniques have gained a significant foothold within the geoscience community for seismic data processing, seismic attribute analysis and for efficiently interpreting 3D volumes. A myriad of recent studies (Roden et al., 2015; Roden and Chen, 2017; Roden et al., 2017; Chopra and Marfurt 2019) have shown promising applications of machine learning techniques that aid in the analysis and interpretation of geologic patterns. Since machine learning works on a sample interval basis, many of these applications are at the sub-seismic resolution scale as opposed to being limited by the seismic wavelet (Roden et al., 2015; Roden et al., 2017). For my methodology, I chose to use self-organizing maps (SOMs) as they are a proven method since the 1980s and are relative quick to calculate (Kohonen, 1990; Roden et al., 2015; Roden and Chen, 2017; Roden et al., 2017; Chopra and Marfurt 2019). However, SOMs are one method of dimensionality reduction and many others are still viable, such as generative topographic maps (GTM) (Roy et al., 2014). In these studies, we exploit the advances of machine learning and multi-attribute seismic analyses, such as principle component analysis (PCA) and SOMs, to test the limits and determine if subtle seismic waveform variations can be detected and properly attributed various gas responses in the subsurface.

The primary objective of seismic exploration is to identify, and map geologic features related to the deposition, generation, migration, and entrapment of hydrocarbons (Chopra and Marfurt, 2005). Taner (2001) defined seismic attributes as “all the information obtained from seismic data, either by direct measurements or by logical or experience-based reasoning”. A good seismic attribute helps highlight the desired geologic feature or reservoir property of interest or help to infer that feature of interest by illustrating the structural regime or depositional environment (Chopra and Marfurt, 2005).

Traditionally, potential gas prospects have been identified by using Direct Hydrocarbon Indicators (DHIs) (Brown, 2011). DHIs are an example of an attribute that measure large seismic amplitude anomalies, or bright spots, found within seismic reflection data (Chopra and Marfurt, 2005). Dozens of recognized DHIs exist, and they vary from basin to basin, based on factors such as depth, lithology, fluid type, and pressure. While these seismic DHIs often indicate the presence of gas, they are vulnerable to uncertainty as they cannot quantify gas saturation and, are only indicators that hydrocarbons could be present. Therefore, seismic interpreters use additional attributes to better characterize these amplitude anomalies.

Each attribute will highlight different properties of the seismic data, such as gas anomalies and bottom simulating reflectors (BSRs), and an iterative interpretation process is needed to capture the total extent of the hydrates. Individually, some of these attributes have limited success in identifying these anomalous responses in the subsurface. Color blending allows us to combine the information content of up to three attributes. In contrast, machine learning models can combine information content of multiple attributes into a single output volume to better characterize the geologic feature of interest.

In Chapter 2, I employ this multi-attribute, unsupervised machine method to further highlight both strong and weak BSRs within the Pegasus Basin, offshore New Zealand. I describe the method in detail and show how PCA is used to identify the most optimal attributes to be used within the SOM. I also discuss the significant SOM improvements for detecting weak BSRs when incorporating amplitude variation with angle (AVA) attributes with instantaneous attributes. My results and conclusions show that both types of BSRs are better identified when using instantaneous attributes such as instantaneous frequency, sweetness and thin bed indicator, which compliment AVA attributes such as gas indicator and fluid factor. Delving deeper into the

individual neuron results, AVA attributes such as the fluid factor and the far stack amplitude consistently ranked among the highest for the classifying the neuron datapoints. These results further support the Class 2n AVA response for hydrate presence in a brine case while also highlighting the Class 3 AVA responses for hydrates with trapped free gas beneath them (Bedle, 2019). Finally, I noted that the PCA and SOM results show that the model is applicable to different seismic surveys and can help resolve weak BSRs.

In Chapter 3, I apply this same methodology for discriminating between high saturation gas (HSG) and low saturation gas (LSG) reservoirs within the King Kong/Lisa Anne and Ursa producing fields in the deepwater Gulf of Mexico, and the Scarborough gas field, offshore Australia (Hilterman, 2001; O'Brien, 2004; Ray et al., 2014). The methodology proved to be successful with the deepwater Gulf of Mexico, however, the same methodology yielded limited results within the Carnarvon Basin. Overall, the clustering results for both Gulf of Mexico surveys showed similar attribute contributions within the anomalous neurons. However, upon further analyzing the neuron results, some attributes represented 0% of the independent data within the Scarborough SOM located in the Carnarvon Basin. Therefore, this suggests that the combination of attributes is unoptimized for the Scarborough SOM. These SOM differences could be attributed to different amplitude responses from two different basins, meaning that the amplitude responses with the Gulf of Mexico are different than the amplitudes in the Scarborough gas field. These differences could be due to different burial histories, pressure regimes and fluid saturations, such as gas and brine (Han and Batzle, 2004; Avseth et al., 2013; Chopra and Castagna, 2014). Although not currently available, future work will incorporate seismic gathers, angle stacks, and well data into this method to further improve these results.

Throughout these various case studies, I present a novel, unsupervised, multi-attribute machine learning workflow to better characterize the presence of gas in the subsurface. The method improves our understanding regarding the distribution of hydrates in the subsurface while also being successful for discrimination between HSG and LSG reservoirs within the deepwater Gulf of Mexico. In both studies, these results are further reinforced with in-context interpretation where the interpreter believes that a BSR or LSG interval could be present in that region. However, more work is still needed to refine the SOM model for the Scarborough, Carnarvon Basin gas field.

REFERENCES

Avseth, P., H. Flesche, and A. J. Van Wijngaarden, 2003, AVO classification of lithology and pore fluids constrained by rock physics depth trends: The Leading Edge, **22**, 1004-1011.

Bedle, H., 2019, Seismic attribute enhancement of weak and discontinuous gas hydrate bottom-simulating reflectors in the Pegasus Basin, New Zealand: Interpretation, **7**, SG11-SG22.

Brown, A.R., 2011, Interpretation of Three-Dimensional Seismic Data: Society of Exploration Geophysicists and American Association of Petroleum Geologists.

Chopra, S., and K. J. Marfurt, 2019, Unsupervised machine learning applications for seismic facies classification: In Unconventional Resources Technology Conference, Denver, Colorado, 22-24 July 2019, 3135-3142.

Chopra, S., and J. P. Castagna, 2014, AVO: Society of Exploration Geophysicists.

Chopra S., and K. J. Marfurt, 2005, Seismic attributes—A historical perspective: Geophysics, **70,** no. 5, 3SO-28SO.

Han, D.H., and M. Batzle, 2002, Fizz water and low gas-saturated reservoirs: The Leading Edge, **21**, no. 4, 395-398.

Hilterman, F. J., 2001, Seismic Amplitude Interpretation: Society of Exploration Geophysicists and European Association of Geoscientists and Engineers.

Kohonen, T., 1990, The self-organizing map: Proceedings of the IEEE, **78**, no. 9, 1464-1480.

O'Brien, J., 2004, Seismic amplitudes from low gas saturation sands: The Leading Edge, **23**, no. 12, 1236-1243.

Ray, A., K. Key, T. Bodin, D. Myer, and S. Constable, 2014, Bayesian inversion of marine CSEM data from the Scarborough gas field using a transdimensional 2-D parametrization: Geophysical Journal International, **199**, no. 3, 1847-1860.

Roy, A., A. S. Romero-Peláez, T. J. Kwiatkowski, and K. J. Marfurt, 2014, Generative topographic mapping for seismic facies estimation of a carbonate wash, Veracruz Basin, southern Mexico: Interpretation, **2**, no. 1, SA31-SA47.

Roden, R., T. Smith, and D. Sacrey, 2015, Geologic pattern recognition from seismic attributes: Principal component analysis and self-organizing maps: Interpretation, **3**, no. 4, SAE59-SAE83.

Roden, R., T. A. Smith, P. Santogrossi, D. Sacrey, and G. Jones, 2017, Seismic interpretation below tuning with multiattribute analysis: The Leading Edge, **36**, no. 4, 330-339.

Roden, R., and C. W. Chen, 2017, Interpretation of DHI characteristics with machine learning: First Break, **35**, no. 5, 55-63.

Taner, M.T., 2001, Seismic attributes: CSEG Recorder, **26**, no. 7, 49-56.

CHAPTER 2: Multi-Attribute Machine Learning Analysis for Weak BSR Detection in the Pegasus Basin, Offshore New Zealand

Julian Chenin and Dr. Heather Bedle.

The University of Oklahoma, School of Geosciences.

This paper has been accepted within the Journal of Marine Geophysical Research, DOI: 10.1007/s11001-020-09421-x.

Keywords: offshore, seismic, hydrates, interpretation, machine learning

ABSRTACT

Gas hydrates that exist in the subsurface are often difficult to detect with reflection seismic data if the seismic data lack a strong bottom simulating reflection (BSR). High-amplitude BSRs are caused by a sharp decrease in acoustic impedance in the rocks as the hydrates transition from their solid form, to a free gas form due to changing pressure and temperature conditions with depth beneath the seafloor. Two key reasons for weak BSRs include 1) insufficient free gas below the hydrate to create the needed impedance contrast, and 2) stratigraphy-parallel BSRs that are subtle and can only be identified with advanced seismic analysis. In these cases, the imaging and detection of the gas hydrate stability zone (GHSZ) becomes particularly difficult, as hydrate detection relies heavily on contextual indicators such as the BSR, gas chimneys, or pockmarks on the seafloor. There are several motivations for better quantifying gas hydrate volumes in the subsurface as they can serve as an economic resource and as a geohazard. To address and improve upon these imaging complications, an unsupervised machine learning multi-attribute analysis is

performed on 2D seismic data in the Pegasus Basin in New Zealand where the BSR is not continuously or clearly imaged.

Rock physics analysis has demonstrated that the inclusion of methane gas hydrates in the pore space results in a slightly increasing amplitude at the base of the gas hydrate zone, regardless of the fluid (brine or gas) in the pore space below the hydrates. This increasing amplitude is quite weak and can be masked by noise. In the scenarios where a strong seismic impedance difference is lacking, a BSR is not typically observed in the seismic data, even though gas hydrates do exist in the subsurface. To enhance the detection of the presence of gas hydrates, a multi-attribute analysis is performed with a series of seismic attributes that can detect the minute changes in the seismic waveform due to the presence of gas hydrates. The successful attributes are those that are sensitive to attenuation, frequency, and small amplitude anomalies.

INTRODUCTION

As an energy producer, gas hydrates present not only a drilling hazard for deeper, economic targets, but also as a potential methane resource by themselves (Field and Barber 1993; Makogon et al. 2007; Faure et al. 2010). Additionally, gas hydrates store large quantities of methane, that if disturbed, could alter our climate (Kennett et al. 2000; Dickens 2003; Ruppel 2011). Gas hydrates (sometimes referred to as clathrate hydrates) are solid solutions where a host lattice is created though water molecules linking together via hydrogen bonding to enclose a diverse variety of molecules, most commonly methane (Englezos 1993). The formation of gas hydrates is only possible in high-pressure and low temperature environments such as permafrost and the shallow subsurface beneath continental slopes. This is the case below the continental slope, in the offshore New Zealand data volume examined in this paper, where hydrates are present (Katz 1981; Katz 1982; Riedel et al. 2010). While gas hydrates exist globally, there are no reliable and universal methods to identify their presence in the subsurface. Bottom simulating reflectors (BSRs) are the most common method of identifying hydrates in seismic data, as has been done in the Ulleung Basin within the East Sea, in the Krishna-Godavari Basin within the Bay of Bengal, and in the Blake Ridge, offshore South Carolina (Holbrook et al. 1996; Yoo et al. 2013; Dewangan et al. 2014). These BSRs are present at the base of the gas hydrate stability zone (GHSZ), which tends to parallel the seafloor due to the pressure and temperature requirements for gas hydrate stability. BSRs are identified by looking for high amplitude reflections that cross stratigraphy and are caused by a sharp decrease in acoustic impedance in the rocks as the hydrates transition from their solid form, to a free gas form due to changing pressure and temperature conditions with depth beneath the seafloor (Singh et al. 1993; Ecker et al. 2000; Griffin et al. 2015). Because of the underlying free gas, the BSRs will have a large negative reflection coefficient due to a decrease in the P-wave

velocity (Navalpakam 2012). However, BSRs are not always observed in areas where gas hydrates are believed to be present (e.g. Finley and Krason 1988; Wood and Ruppel 2000; He et al. 2007). Two key reasons for weak BSRs include 1) insufficient free gas below the hydrate to create the needed impedance contrast, and 2) stratigraphy-parallel BSRs that are subtle and can only be identified with advanced seismic analysis (Xu and Ruppel 1999; Plaza-Faverola et al. 2012). In these cases, the imaging and detection of the GHSZ becomes particularly difficult, since hydrate detection relies heavily on a large decrease in acoustic impedance due to a significant drop in P-wave velocity resulting from trapped gas below the BSR (Singh et al. 1993; Navalpakam et al. 2002). Additional methods to support the presence of hydrates include gas chimneys, or pockmarks on the seafloor that are indicative of gas migration (Plaza-Faverola et al. 2012). These 'missing' BSRs demonstrate that an improved understanding of the expected seismic response is needed in areas where no other hydrate identifier is present.

As BSRs are used to infer the presence of hydrates, it becomes difficult to infer the presence of hydrates where robust BSRs are lacking (Riedel et al. 2010). A clear BSR is observed through most of the Pegasus Basin, offshore New Zealand, but is observed to be weak, discontinuous, or absent in some regions. Therefore, do hydrates exist where no BSRs are present within the GHSZ, or are there no hydrate accumulations in these regions? This research question is highlighted in Figure 2-1a-b where a section of weak amplitude BSRs are separated by two, distinct high amplitude BSRs in Line 19 of the PEG09 seismic survey. There is a high amplitude contrast where high amplitude BSRs are observed due to the trapped free gas below the hydrate accumulations (Figure 2-1b). However, where there is no trapped free gas to create a high amplitude contrast, there could still be hydrates present. In these areas, a small amplitude contrast would still be observed (Figure 2-1b), however, not as pronounced compared to the surrounding background

amplitude responses due to lithology interfaces such as in Figure 2-1b. This figure highlights the relationship between acoustic impedance contrasts resulting from varying amounts of hydrate accumulations.

There are several motivations for better quantifying gas hydrate volumes in the subsurface as gas hydrates can serve as an economic resource as well as a geohazard. Hydrates can serve as an economic resource as they have the capability of behaving as a seal for conventional hydrocarbon reservoirs (Singh et al. 1993; Makogon et al. 2007; Walsh et al. 2009). They are also a geohazard, as sediments which contain gas hydrates can be destabilized through natural or man-made events eventually triggering landslides (Field and Barber 1993; Faure et al. 2010). Finally, they can contribute directly to climate change through the release of methane into the ocean and eventually into the atmosphere due to variations in Earth's temperature and sea level which could destabilize hydrates (Englezos 1993; Kennett et al. 2000; Dickens 2003; Ruppel 2011).

PEGASUS BASIN

Geologic Background

The Pegasus Basin, located offshore New Zealand, lies between two subduction systems with the Hikurangi margin and the East Coast Basin to the northwest and the extinct subduction of the Chatham Rise to the southeast (Figure 2-2a-c) (Plaza-Faverola et al. 2012; Kroeger et al. 2015). The formation of the basin is controlled by the convergence between the Australian and Pacific lates (Kroeger et al. 2015). The Hikurangi Margin, offshore eastern Wairarapa, is a sediment-rich active continental margin that is related to the westward subduction of the Pacific Plate beneath New Zealand's continental crust, where faulting transitions from subduction to oblique-slip (Plaza-Faverola et al. 2012; Kroeger et al. 2015).

The southern part of the imbricated accretionary wedge of the overriding Australian Plate extends 40 km off southeastern Wairarapa, where it gives way to the southern Hikurangi Trough (Pegasus Basin). The Pegasus Basin has an approximate water depth of 1000 to 2600 m but can exceed 3000 m along the Hikurangi Channel. Deeper water generally marks the location of the modern plate interface where the Hikurangi Plateau is subducting under the North Island of New Zealand, however, this is not as apparent in the Pegasus Basin except towards the north (Plaza-Faverola et al. 2012; Kroeger et al. 2015; Bland and Uruski 2015). From Neogene to modern time, approximately 6 km of clastic deposits have filled the basin sourced by the erosion of the uplifted North Island and thins southwards towards the Chatham Rise (Kroeger et al. 2015). A prominent geomorphologic feature in the Pegasus Basin is the Miocene-age Hikurangi Channel, a 2000 km long aggradational deep-sea channel which runs almost parallel to the accretionary prism. It is sourced from the south-west by the Southern Alps uplift and the sediments flow along the northern slope of the Chatham Rise (Lewis et al. 1998; Kroeger et al. 2015).

Hydrates in the Pegasus Basin

Gas hydrates have formed in sediments of Pliocene to modern age, occupying the shallowest portion of the basin at water depths greater than 600 m within the Pegasus Basin (Navalpakam et al. 2012; Kroeger et al. 2015). In order for these gas hydrates to form, there are three dominant geological controls on the thickness of the free-gas zone, as well as the free gas underlying gas hydrates: 1) the rate of upward fluid flow relative to the seabed, 2) the pressure and temperature conditions at the base of the GHSZ, and 3) tectonic uplift rate of the seabed (Haacke et al. 2007). Recent studies suggest that the hydrates in the Pegasus Basin are sourced from Quaternary microbial methane and upward migration of gas from beneath the GHSZ (Plaza-

Faverola et al. 2012; Kroeger et al. 2015). The migration pathways for the gas were along fault planes and laterally from less permeable hydrate bearing zones to more permeable areas (Henrys et al. 2009; Plaza-Faverola 2012, Kroeger et al. 2015).

There are three primary zones where hydrates are sustained by focused gas migration pathways and concentrated within the Pegasus Basin (Plaza-Faverola et al. 2012): close to the New Zealand shore along the Opouawe Bank, at the crest of the frontal anticline, and in the sands beneath the Hikurangi Channel (Figure 2-2b). A clear BSR is observed through most of the basin, but in some regions is observed to be weak, discontinuous, or absent (Figures 2-2b-c). Previous studies have linked clear BSRs to geological structures that promote fluid flow, such as anticlines or faults (Henrys et al. 2009; Plaza-Faverola et al. 2012; Crutchley et al. 2019). There are also instances where hydrates can fill open pores and fractures locally, thus creating a permeability barrier and causing free gas to migrate laterally towards structural highs (Nimblett and Ruppel 2003). Therefore, a majority of the weak BSRs in this study area are located where strata are laterally continuous with no significant degree of dip yet high-amplitude BSRs are observed where anticlinal features or other migration pathways are present.

Data

Within the Pegasus Basin, this study analyzes two 2D seismic datasets: the PEG09 and APB13 surveys (Figure 2-2a-c). There are no wells currently drilled in the Pegasus Basin. The PEG09 survey consists of several long-offset, multichannel seismic 2D profiles that cover approximately 3200 km and were collected in 2009. This survey was contracted by the New Zealand Ministry of Economic Development and shot by RV Reflect Resolution (now RPS Energy), between November 2009 and March 2010, to stimulate exploration interest within the

basin as it showed promising petroleum potential (Bland and Uruski 2015). The record length was 12 s using a 2 ms sampling interval and was processed by Gardline CGG PTE Ltd. This survey was later reprocessed by CGG Services in Singapore under contract to Anadarko New Zealand Company in 2014 (Anadarko New Zealand 2014). The more recent APB13 survey was similarly acquired and processed in 2014 by CGG Services in Singapore and also consists of wide-angle, multichannel seismic 2D profiles covering 4600 km. The recording length was 10.5 s using a 2 ms sampling interval. Both datasets are positive standard polarity with a shot interval of 37.5 and a group interval of 12.5 m (Anadarko New Zealand 2014). Both high and weak amplitude BSRs exist within both surveys, shown in Figures 2-3a-b as an example. These line pairs represent the two different 2D surveys yet show similar high amplitude and weak/discontinuous BSRs.

Figures 2-3a and 2-3b highlight a similar N-S vertical seismic profile from both 2D seismic datasets in the Pegasus Basin. In both lines, there are a few distinct, high-amplitude BSRs that are indicative of gas hydrates. Figures 2-3c-d take a closer look between the two high-amplitude BSRs from Figures 2-3a and 2-3b respectively. The BSRs' amplitude responses appear to dim horizontally between one another, reducing confidence in the interpretation that hydrates are present in this region. The dim, horizontal amplitude response between both strong BSRs imaged at each end of the line is interpreted to be a weak BSR which begs the question of whether a BSR is a sufficient condition for hydrates to exist? Are there also hydrates where the BSR is not clear and is discontinuous (Hillman et al. 2017; Bedle 2019)? Furthermore, is there a method for better characterizing stratigraphy-parallel BSRs? Are the BSRs actually there, but very subtle? Or are the BSRs not there? Previous studies have linked high-amplitude BSRs to geological structures such as anticlines and faults which promote fluid flow (Henrys et al. 2009; Plaza-Faverola et al. 2012; Crutchley et al. 2019). In these regions, the gas runs up strata and accumulates in a thicker

layer. However, in laterally continuous areas with no significant dip, the gas accumulation is quite thin, and it becomes difficult to create high-amplitude BSRs. The lack of trapped free gas to create a strong impedance contrast beneath the weak BSRs makes it difficult to determine if there is hydrate present there or not. Traditional geophysical gas hydrate identifications methodologies need to be further improved as they are limited in answering these questions. Previous studies conducted some rock-physics modeling analyses to further investigate the seismic response of gas hydrates (Dvorkin and Nur 1996; Dvorkin et al. 2003; Bedle 2019).

Gas Hydrate Stability Zone (GHSZ)

Previous rock physics modeling analyses have demonstrated that the inclusion of methane gas hydrates in the pore space results in a slightly increased amplitude at the base of the gas hydrate zone, regardless of the fluid (brine or gas) in the pore space below the hydrates (Spence et al. 2010; Lui and Lui 2018). However, laboratory results show that the Vp of the sediments with hydrate increases only after saturation reaches approximately 40% and the hydrate starts to cement the grains (Yun et al. 2007; Waite et al. 2009). This increased amplitude is quite weak in strength, particularly in shale-rich lithologies, or in sandier lithologies where the pore space contains brine. The seismic wavefield is particularly sensitive to the active migration of free gas, causing amplitude blanking due to significant attenuation (Guerin et al. 1999; Dewangan et al. 2014). This attenuation is well highlighted in Figure 2-3a-b where the faults become very difficult to image due to the significant attenuation caused by the migration of free gas, a complex faulting system and depth of signal penetration (Dewangan 2014). These attenuation mechanisms are due to both scattering and squirt flow (Guerin et al. 2002; Dvorkin and Uden 2004; Priest et al. 2006; Best et al. 2013). However, in the instance of hydrate-bearing sediments with no trapped free gas

underneath, there appears to be low attenuation when compared to the attenuation of background sediments (Dewangan 2014). Significant attenuation is therefore only expected where trapped free gas is present (Guerin 1999; Dewangan 2014) and no significant attenuation is observed for hydrate-bearing sediments with no trapped free gas beneath them. This attenuation effect caused by trapped free gas is clearly shown between the two high-amplitude BSRs from Figure 2-3c-d. Large saturations of hydrate within the rock will cause P- and S-wave velocities to increase substantially relative to the same rock with no hydrate inclusions within the pore space (Dvorkin et al. 2003; Spence et al. 2010). However, for small concentrations of hydrate within the rock, it becomes more difficult to observe this effect, especially as it relates to S-waves. This velocity increase depends on how the hydrates are distributed at the grain scale as S-wave velocities depend on the rigidity and shear modulus of the host rock (Yun et al. 2005; Yun et al. 2007; Spence et al. 2010; Kim et al. 2013).

Bedle (2019) formulated a series of rock-physics models to evaluate how various elastic properties change with different hydrate saturations and mediums. From these hydrate rock-physics models, amplitude versus angle (AVA) responses can be derived. This is important because AVA attributes can now be calculated to potentially better reveal the extent of the GHSZ. Bedle (2019) demonstrated that a Class 3 AVA response (low intercept value and a negative gradient where amplitude becomes increasingly more negative at larger angles) is observed for hydrocarbon accumulations where high amplitude BSRs are present (Chopra and Castagna 2014). In the instance of brine, a very weak Class 2n AVA response (has a low intercept value and a negative gradient where the amplitude becomes more negative at larger angles) is expected whether the BSR exists in a sand or shale (Chopra and Castagna 2014; Bedle 2019). Therefore, the rock-physics modeling demonstrates that in regions where hydrocarbons (or biogenic gas in

our study area) are not at significant enough saturation to cause a seismic anomaly, such as laterally in between high amplitude BSRs, hydrates would be best detected in the far angle stack because in these regions because the expected seismic response is a Class 2n AVA.

Several AVA attributes were then used to further identify the extent of hydrates in the Pegasus Basin. Bedle (2019) found that these attributes further increased ability to identify some previous seismically invisible BSRs. However, can this identification method be further improved to identify the full extent of the GHSZ? We have developed a new methodology, which uses an unsupervised machine learning multi-attribute analysis on 2D, full- and angle- stack seismic data within the Pegasus Basin with self-organizing maps (SOMs) is employed to better detect these seismically invisible/weak BSRs.

METHODOLOGY

Although AVA attributes help to enhance the extent of hydrates in the seismic data, individual attributes are limited in revealing their entire presence. Each attribute will highlight different properties of the BSRs, and an iterative process of interpreting multiple volumes is needed to capture the total extent of the hydrates. However, by using a machine learning approach that incorporates all of these attributes, this iterative attribute interpretation workflow can be reduced, and more time can be spent on quality control of the SOM results. The machine learning model can instead combine multiple attributes into one comprehensive attribute to highlight the extent of hydrates. This study uses principle component analysis (PCA) to analyze the multi-dimensional nature of these attribute combinations and visualizes these relationships using SOMs. There have been multiple geophysical studies using PCA and SOMs to better characterize the subsurface. Sacrey et al. (2014) looked at several conventional and unconventional case studies to

demonstrated how this methodology was able to optimize production through multi-attribute analysis by identifying anomalies within the seismic data. Another study by Roden and Chen (2017) showed how PCA and SOMs can better identify direct hydrocarbon indicator (DHI) characteristics. In another example, Chopra and Marfurt (2018) showed how unsupervised machine learning methods, such as PCA and SOMs, showed promising results in classifying seismic facies. By building off of these practical examples that use a multi-attribute machine learning approach to better characterize the subsurface, this study aims to use this methodology to improve our understanding of the constraints on the distribution of hydrates in the subsurface.

Principle Component Analysis (PCA)

PCA is a linear mathematical technique that reduces a set of variables, such as seismic attributes, to a set that represents the majority of variation in the multidimensional data (Jolliffe 2002; Sacrey and Roden 2014; Roden et al. 2015). The first principal component accounts for the most variability in the data with each succeeding orthogonal component best accounting for the remaining variability. Although the first principal component highlights the largest linear attribute combinations that best represents the variability of the bulk of the data, it may not identify specific features that are of interest to the interpreter (Sacrey and Roden 2014; Roden et al. 2015). Therefore, succeeding principal components were evaluated because they may be associated with BSR characteristics not identified with the first principal component. Applying PCA to a large set of seismic variables, such as seismic attributes aids in identifying meaningful combinations of attributes that best reveal the discontinuous BSRs. Additionally, attributes that are most likely to aid in locating the base of the GHSZ, such as attributes sensitive to the gas in the pore space or to acoustic impedance changes, were pre-selected to be used within the PCA.

Self-Organizing Maps (SOMs)

Following PCA analysis, the attributes deemed the most successful for revealing BSRs are then incorporated in a SOM. Due to the multidimensional nature of PCA results, SOMs are employed to help visualize these attribute relationships. A SOM is a collection of neurons that classify data samples into categories based on their various geological or geophysical properties. This is done by projecting the clusters onto a latent space for visualization (Kohonen 1990; Roy 2013). Several SOM hyperparameters were tested such as neuron count and the number of epochs (iterations). A detailed generalized schematic of the workflow is shown in Figure 2-4.

Full- and angle-stack seismic data were used within the seismic attribute analysis. Several AVA attributes were calculated and evaluated, including those studied by Bedle (2019). However, gas indicator and Shuey's fluid factor were the two primary AVA attributes that stood out from PCA. Gas indicator is a logarithmic AVA attribute that has traditionally been used to highlight gas sands with a Class 2 AVA response. It is defined as the intercept multiplied by the natural log of the gradient's absolute value (Veeken 2007). Gas indicator ranked as the only attribute in the ninth eigenvector, effectively representing the entire eigenvector, and is thus indicates unique variability in the dataset. Bedle (2019) suggests that gas indicator could be one of the better attributes for highlighting Class 2 AVA responses. This was verified by the PCA through its use in the SOM analysis to better visualize weak BSRs. Shuey's fluid factor (Shuey 1985; Smith and Gidlow 2003) is another AVA attribute useful in highlighting Class 2 AVA sands and is calculated using the seismic intercept and gradient. Fluid factor consistently ranked at over 80% in eigenvector contribution for the first three eigenvectors, meaning that fluid factor is a good representation of the independent variability in the seismic dataset and could be helpful in revealing the hidden

BSRs. Multiple instantaneous attributes were also evaluated with instantaneous frequency, sweetness, and thin bed indicator consistently ranking at over 80% in eigenvector contribution in the first three eigenvectors.

There was also a balance to be struck between clustering every detail within the seismic that excluded noise while also optimizing the number of neurons to render the model computationally efficient. Several different combinations of neuron and epoch (iteration) counts were created to determine the optimal value. This is shown in Figure 2-5a-f where we compare SOM models with different neuron and epoch counts. The first SOM model, shown in Figure 2-5a, used an 8x8 neuron count with 100 epochs. This SOM parameterization was found to be computationally inefficient as it classified the same feature, such as high amplitude BSRs, in different clusters (shown in Figure 2-5b). Furthermore, this model classified a significant amount of seismic noise within empty neurons (shown in Figure 2-5c). Upon overlapping both the redundantly classified, high amplitude BSRs with the classified seismic noise (shown in Figure 2-5d), it becomes apparent that the number of neurons should be reduced to optimize the model. The number of neurons was reduced down to 36 (shown in Figure 2-5e) and was trained for 100 epochs. Notice how this model was able to achieve near identical results to those observed in Figure 2-5a. Further analysis reduced the number of epochs down to 50 (shown in Figure 2-5f) and also achieved similar results to Figure 2-5a. This study found that a SOM model with 36 neurons and 50 epochs (shown in Figure 2-5f) was able to achieve nearly identical results to a SOM model which used 64 neurons and 100 epochs (shown in Figure 2-5a). However, SOM models that used less than 36 neurons returned results that did not detect as many of the weak BSR extents. Therefore, the optimized SOM model was run on a 6x6 neuron count (total of 36 neurons) with 50 epochs for both lines. These neuron dimensions and number of epochs were used because they are

robust enough to highlight minute changes and details within the seismic data, such as the base of the GHSZ, while also being computationally efficient.

RESULTS

After the number of neurons and epochs were optimized, I then evaluated the number of attributes to use within the optimized model. The number and combination of attributes to use in a SOM model were determined using a combination of PCA and different SOM runs. These SOM results were compared to the far angle stack amplitude section of Line 19 from the PEG09 survey (Figure 2-6a-b). One of the first SOM results (Figures 2-6c-d) used an 8x8 matrix as well as eight instantaneous attributes. These instantaneous attributes included: envelope, envelope slope, Hilbert transform of the amplitude data, instantaneous frequency, normalized amplitude, relative acoustic impedance, sweetness and thin bed indicator (Figures 2-6c-d). These attributes were chosen from PCA results and Table 2-1 describes the definitions and uses of these attributes.

These eight attributes all ranked over 70% in eigenvector contribution within the first three eigenvectors for the initial SOM results. When these attributes were used in conjunction with each other, the base of the GHSZ was better imaged in the SOM results. However, similar to previous analyses in Figure 2-5, several of the neurons were redundant and correlated to a significant amount of seismic noise. Also, several neurons needed to be displayed (shown in Figure 2-6d) to generate the same result seen in Figure 2-6e-f. Therefore, the model was computationally inefficient and was improved to achieve the same level of accuracy in a shorter time with less computational intensity. The optimized SOM ran with 36 neurons and five attributes: instantaneous frequency, sweetness, thin bed indicator, fluid factor and gas indicator (Figures 2-6e-f). Results found that the five attributes, which used a combination of both instantaneous and

AVA attributes, were sufficient in improving the detection of weak BSRs. A larger number of attributes tended to render the algorithm computationally inefficient and any fewer tended to not include the furthest extent of the indistinct BSRs.

Once the best SOM parameters were determined for the PEG09 Line 19, this parameterization was then applied to the PEG09 survey with the raw, uninterpreted results of Line 6 and 19 shown in Figure 2-7a. Once the raw SOMs neurons were interpreted, as shown in Figure 2-7b, the results helped enhance the lateral extent of weak BSRs and how they are potentially connected to the high amplitude BSRs within the Pegasus Basin. The green arrows in Figure 2-7b indicate the high amplitude BSRs whereas the orange arrows highlight the better detected weak BSRs within the seismic data. The SOM was able to resolve the previously hidden BSR, enhancing our understanding of the extent of hydrates within the PEG09 survey. After the SOM model was optimized for the PEG09 survey, an identical parametrization was applied to the APB13 survey to test if this gas hydrate detection method is transferable to other seismic surveys. The same SOM model and number of attributes were applied to the APB13 survey and the raw, uninterpreted and interpreted SOM results are displayed with Lines 17 and 38 as shown in Figure 2-8a-b. Similar to the results from the PEG09 survey, the optimized SOM model was able to better resolve the weak BSRs within the APB13 survey that were previously hidden in the amplitude sections, shown by the orange arrows in Figure 2-8b. It was also interesting to note that both surveys had the same specific neurons (23, 34 and 35) that classified the weak BSRs whereas the other neurons grouped different geologic features such as bedding, and other lithology variations. We interpret the orange arrows in both SOM results as weak BSRs because the clusters displayed from neurons 23, 34 and 35 are discontinuous and are heavily weighted towards Class 2n AVA attributes.

Neurons 23, 34 and 35 are most heavily weighted by a combination of fluid factor and far stack amplitude, fluid factor and instantaneous frequency, as well as far stack amplitude and instantaneous frequency. Overall, a combination of fluid factor and far stack amplitudes appears to be the most revealing for indistinct BSRs with a smaller influence in cluster weighting due to instantaneous frequency. AVA attributes such as fluid factor and gas indicator are helpful in identifying these weak BSRs as these attributes are particularly sensitive to the presence of gas within the pore space (Shuey 1985; Smith and Gidlow 2003; Veeken 2007). Instantaneous attributes such as instantaneous frequency, sweetness and thin bed indicator, are particularly helpful for analyzing bed thicknesses, identifying "sweet spots" in hydrocarbon exploration, and for locating the edges of low impedance thin beds (Taner et al. 1979; Hart 2008; Subrahmanyam and Rao 2008; Koson et al. 2014). These instantaneous attributes are especially helpful for better visualizing weak BSRs that have low impedance contrasts due to their slight increase in amplitude as a result of hydrates within the pore space (Spence et al. 2010; Lui and Lui 2018). Rather than using seismic attributes separately to identify BSRs with limited resolution, the SOM improves the imaging and understanding of gas hydrate presence by combining several seismic attributes. BSRs are better identified when using a multi-attribute analysis that complements AVA attributes sensitive to the presence of gas in the pore space with other instantaneous attributes highlighting bed thicknesses and low impedance contrasts.

PCA results for both surveys showed near identical eigenvalues across the different eigenvectors (Figure 2-9). Here, the "% Max" represents that same attribute variance displayed as a percentage of the largest eigenvector whereas "Percentage" represents how much each attribute contributed toward that eigenvalue. Attributes are ranked in similar orders throughout all of the eigenvectors for both surveys (shown by the black arrows in Figure 2-9). Additionally, the

eigenvalues from both surveys are nearly identical, demonstrating that the data clusters within the seismic surveys are also quite similar.

Notice how the maximum percentage contribution of the attributes rank in similar order with similar values for eigenvalue 2 (shown by the red arrows in Figure 2-9). For the PEG09 survey, these two attributes (instantaneous frequency and thin bed indicator) contributed approximately 33% to eigenvector 2 and represented a significant amount of the variance for the PEG09 dataset (shown under % Max in Figure 2-9). This same relationship for eigenvector 2 in the PEG09 survey was also observed for the APB13 survey. Attributes such as instantaneous frequency and thin bed indicator also shared similar percentage and percent max values. For this reason, these attributes were used in the final SOM model as they contributed a significant amount to the first few eigenvectors and represented the majority of the variance from each dataset (highlighted in green in Figure 2-9). These relationships illustrate that these attributes reveal identical distributions with the seismic data and that this method is transferable to other areas. SOM clusters were identical in both the PEG09 and APB13 surveys and successfully detected weak BSRs that were previously hidden within the seismic data. These results detected previously unknown gas hydrate accumulations where BSRs are indistinct, clearly showing that there are gas hydrate accumulations throughout the basin and not just where the high amplitude BSRs are observed. These observations are further supported by contextual interpretation, where the interpreter expects the BSRs to be present, and matches well with the previous observations and interpretations by Crutchley et al. (2016), Crutchley et al. (2018), and Kroeger et al. (2019).

DISCUSSION

The amplitude response strength of BSRs is related to the amount of trapped free gas beneath them (Henrys et al. 2009). There are still significant ongoing studies into better understanding the source of gas and its migration into the GHSZ (Kroeger et al. 2015; Kroeger et al. 2019). Xu and Ruppel (1999) illustrated how gas migrates upwards in solution along permeable fault pathways until it reaches the base of the GHSZ, where gas concentration surpasses solubility. This transition from gas in solution to free gas causes a sudden increase in velocity, or seismic impedance, thus creating the observed high-amplitude BSRs in the Pegasus Basin. This migration concept is further supported by Plaza-Faverola et al. (2012) where they investigated the accumulation and distribution of concentrated hydrate zones as a result of focused fluid flow within the basin. Many of the migration pathways for gas hydrates originated from gas chimneys that are related to underlying faults. These fluids can migrate vertically towards topographic highs, such as towards the frontal anticline, or towards traps, such as the triangular trap formed by the dipping Chatham Rise and other hydrate bearing sediments (Plaza-Faverola et al. 2012; Crutchley et al. 2019; Turko et al. 2020). This pattern is well observed in Figure 2-10 where the high amplitude BSRs overlap with structural elements in the study area and further illustrate the migration pathways for gas within the Pegasus Basin. This is further supported from significant attenuation observed along these migration pathways where free gas is present (shown in Figure 2-3a-d and 2-10). Additionally, gas was sampled at vent sites on the seafloor and revealed that the gas also had microbial origin (Kroeger et al. 2015).

However, in regions where strata are laterally continuous with no significant dip, it is difficult for free gas to become trapped and create high-amplitude BSRs, as there is no structure present to create a significant accumulation of gas. This inability for free gas to become trapped

below hydrate-bearing sediment in a flat lying sediment layer within a package of flat lying sediments that have relatively uniform lithology will create an amplitude response that is difficult to discern from other reflectors indicative of background geology. If neurons 23, 34 and 35 were to represent lithology in Figures 2-7a-b and 2-8a-b, the clusters would be laterally continuous in time and well defined across the survey. This assumption is only valid where lithology does not vary laterally and may not hold near the Hikurangi Channel in the Pegasus Basin where there are several phases of Pleistocene channel/levee complexes (Kroeger et al. 2019). However, the theoretical seismic response will be different for hydrate-bearing and non-hydrate-bearing sediments as the inclusion of hydrate in the pore space for a brine case would produce a weak Class 2n AVA response (Bedle 2019). By using this study's proposed multi attribute machine learning model, hydrate bearing sediments were able to be differentiated from non-hydrate bearing sediments at the base of the GHSZ. This differentiation is well highlighted in Figures 2-7 and 2-8 where we were able to infer where other hydrate-bearing sediments may be located where there is no significant geologic dip. The location of these features is also in accordance with the expected temperature and pressure conditions for gas hydrates to exist within the Pegasus Basin (Plaza-Faverola et al. 2012; Kroeger et al. 2015).

While seismic attributes on their own have limited success in identifying weak BSRs, combining attributes together helped to better characterize and visualize these often seismically transparent hydrate accumulations. SOM models that only combined instantaneous attributes were successful in teasing out some of the weak BSRs but were further improved once incorporated with AVA attributes such as fluid factor and gas indicator. Figure 2-11a-g displays the individual attributes that were used for the final SOM. The final SOM result (Figure 2-11a) is shown alongside the far angle stack of Line 19 from the PEG 09 survey (Figure 2-11b). Instantaneous

frequency in Figure 2-11c and gas indicator in Figure 2-11f seemed to highlight the other subtle responses related to the weak and discontinuous BSRs. Attributes such as thin bed indicator in Figure 2-11d and sweetness in Figure 2-11e seem to help image some of the weaker BSRs and further compliment the other attribute results. The fluid factor attribute in Figure 2-11g matched nearly exactly with the SOM results in Figure 2-11a. These observations are in accordance with the previously discussed cluster analysis where the three neurons (23, 34 and 35) were most heavily weighted by a combination of fluid factor in combination with far stack amplitude and instantaneous frequency. These neurons also had minor contributions from other attributes such as gas indicator, thin bed and sweetness which could be further complimenting the more dominant attributes to further reveal the extent of hydrates in the subsurface. Also, these results indicate that there is a Class 2n AVA response for hydrate presence in a brine case while also highlighting the Class 3 AVA responses for hydrates with trapped free gas beneath them. Therefore, AVA attributes such as gas indicator and fluid factor are helpful in highlighting these features. However, instantaneous frequency still had a significant percentage contribution within each of the neurons. Therefore, both weak and strong amplitude BSRs are better identified when using other instantaneous attributes that are helpful in highlighting bed thicknesses and low impedance contrasts, which in turn complements AVA attributes that are sensitive to the presence of gas in the pore space. Figure 2-12 illustrates the enhanced interpretation capabilities for hydrates in the PEG09 and APB13 survey using the proposed SOM workflow.

Additionally, all of the attributes used in the final SOM were able to detect and image the high amplitude BSRs within neurons 23, 34 and 35. Figure 2-13a-d shows these SOM clusters highlighting the high amplitude BSRs and enhancing their interpretability on Line 30 of the APB13 survey. However, these high amplitude BSR clusters only represented a small percentage of the

classified data points within those neurons meaning that the displayed neurons primarily identified anomalous weak BSRs. Similar observations were also noted for the APB13 survey SOM result. Figure 2-14a-d shows how the some of these weaker BSRs are better highlighted using our proposed SOM model and their enhanced interpretability on Line 30 of the APB13 survey. The neurons also exhibited higher weighting towards fluid factor in combination with gas indicator and instantaneous frequency. This higher weighting towards attributes such as gas indicator and fluid factor could be due to how successful they are in identifying the presence of gas and other anomalous fluids within the pore space by revealing Class 2 and 3 AVA anomalies. There may have also been a higher weight towards instantaneous frequency as this attribute is helpful for indicating the edges of low impedance thin beds, such as is the case for weak BSRs (Taner et al. 1979; Subrahmanyam and Rao 2008). A study conducted by Navalpakam et al. (2012) along the Hikurangi Margin found that weak BSRs are primarily caused by low gas saturation where gas is only present within pores or fractures with a patchy distribution. Therefore, attributes such as fluid factor and gas indicator are prime candidates for identifying this patchy gas saturation and further revealing weak BSRs in our study area. The results also helped to detect weak BSRs over the same study area, however, in a different survey. This is because PCA analysis revealed that the PEG09 and APB13 surveys were nearly identical with attributes ranking in the same order in different eigenvectors.

The PCA and SOM results show that the model is applicable to different seismic surveys and can help resolve weak BSRs. Another interesting observation was that SOM result for Line 17 of the APB13 survey detected no weak BSRs in the eastern portion when it did detect these in the PEG09 survey. This is hypothesized to be due to two primary reasons. The first being that these lines are slightly offset from one another as the 2D lines belong to separate surveys. The distance

between the PEG09 and APB13 survey lines is approximately 3500 m, which could be enough for the weak BSR from Line 06 in the PEG09 survey to fade. Another reason is that there appears to be no minor anomalies within the seismic amplitude and attributes. When looking closer at the fluid factor attribute over the eastern portion of Line 17 from the APB13 survey, there were no anomalies observed from Line 06 of the PEG09 survey. Therefore, it is hypothesized that the SOM for APB13 did not map the missing weak BSR as there most likely was no weak BSRs in that region. If there were no observed Class 2n AVA anomalies, it is possible that there are no hydrates present in the pore space. This could be due to the fact that there is not a homogeneous generation of methane throughout the entire Pegasus basin (based on the models presented in Plaza-Faverola et al. 2012, Kroeger et al. 2015, and Kroeger et al. 2019). Additionally, it could be that the migration pathways feeding other or older populations of methane into the area do not exist for some structural or geologic reason. Hydrate accumulations near structural highs are primarily controlled by fluid focusing and transport of CH4 (Henrys et al. 2009; Plaza-Faverola et al. 2012; Crutchley et al. 2019). However, in areas where the generation and/or migration of microbial methane are not present, no gas hydrates can form.

A prominent diagnostic feature of hydrate-bearing sediments is an increase in both the P- and S-wave velocities once hydrate saturation exceeds approximately 40% (Dai et al. 2004; Dai et al. 2008a, 2008b; Yun et al. 2007; Waite et al. 2009). There exists a wide range of models that are based on the amount of hydrate and the growth between hydrate and the sediment (Dai et al. 2004; Xu et al. 2004; Waite et al. 2009; Zhang et al. 2020). However, these models exhibit a wide range of elastic properties for hydrate-bearing sediments (Dai et al. 2004; Waite et al. 2009). Overall, these models nevertheless demonstrate that even a small amount of hydrate present within the sediments will create an increase in acoustic velocities (Dai et al. 2004; Waite et al. 2009). It is

important to note that these models only account for the elastic properties and do not account for inelastic parameters such as attenuation (Dai et al. 2008a). Therefore, it may be difficult to resolve very small hydrate accumulations in the subsurface by only using the seismic amplitude response. This could be circumvented by reprocessing the data to highlight and preserve the amplitude of shallow geologic features to better visualize BSRs (Dai et al. 2004; Dai et al. 2008a). Finally, it is also important to note that there were other neurons that only identified high amplitude BSRs. However, this study is focused on better identifying weaker, less obvious BSRs that may be hidden within the seismic volume. These neurons could be beneficial for quick mapping and analysis of prominent BSRs within a given area when using attributes which are sensitive to the inclusion of gas and help identify thin beds as well as low impedance contrasts.

CONCLUSIONS

Instantaneous attributes that detect changes in the frequency and phase of seismic data tend to cluster together in the PCA to reveal the interface at the base of the GHSZ. The extent and resolution of discontinuous BSRs from preliminary results are significantly improved when AVA attributes, such as gas indicator and fluid factor, were used in combination with instantaneous attributes sensitive to frequency, and small amplitude anomalies. Both weak and strong BSRs are better identified when using instantaneous attributes such as instantaneous frequency, sweetness and thin bed indicator, which compliment AVA attributes such as gas indicator and fluid factor. Individually, some of these attributes have minimal success in identifying the seismically transparent hydrates. However, employing a multi-attribute analysis provides clearer insight and confidence into the identification and distribution of gas hydrates. PCA results for both the PEG09

and APB13 surveys were nearly identical demonstrating that this method for detecting gas hydrates is transferable to other surveys.

ACKNOWLEDGEMENTS

We would like to acknowledge New Zealand Petroleum and Minerals for access to the Pegasus Basin 2D seismic surveys. Thank you to Geophysical Insights and Schlumberger for software license donations to the University of Oklahoma. We would also like to thank the General Bathymetric Chart of the Oceans (GEBCO) Compilation Group for the bathymetric data used in this study. An additional thank you to all of the University of Oklahoma faculty and students as well as the AASPI Consortium for their help and guidance throughout this project. Finally, we would like to thank the anonymous reviewers for the valuable feedback and recommendations for improving this manuscript.

FIGURES

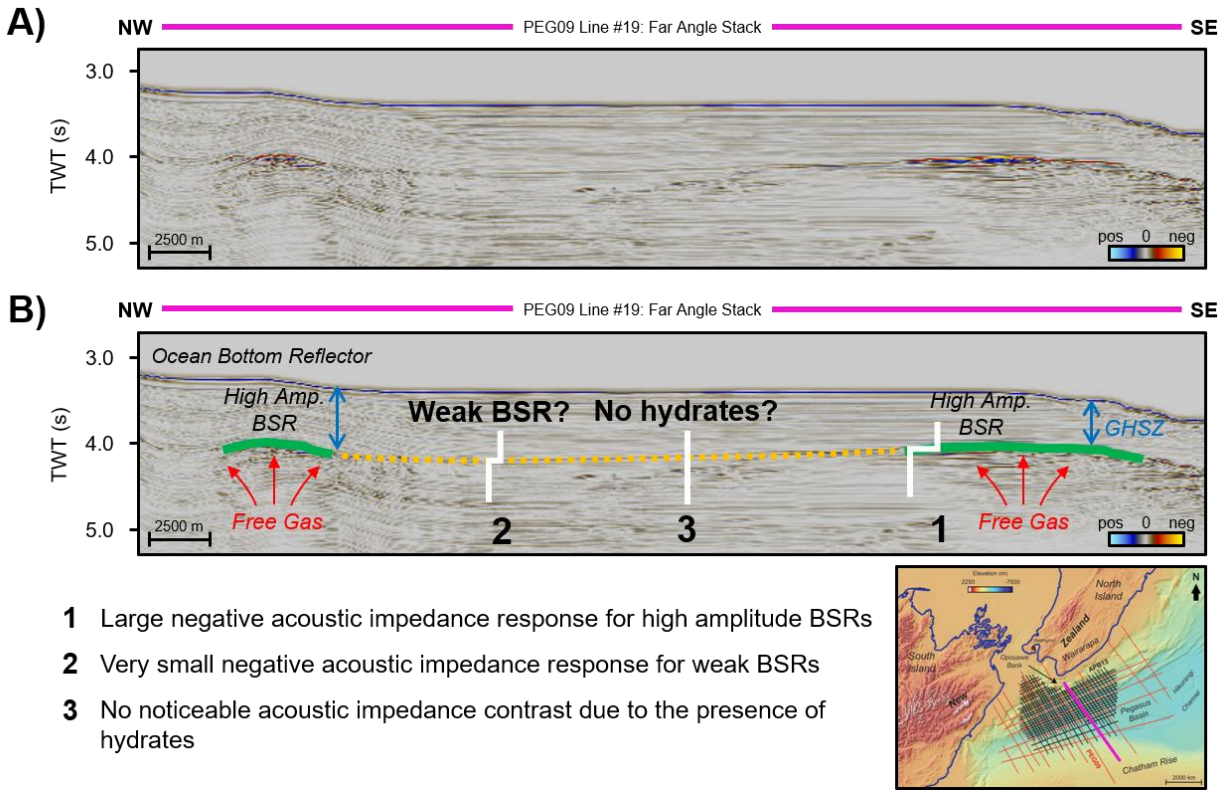

Figure 2-1: A) Cropped far angle stack seismic amplitude section of Line 19 from the PEG09 survey with B) an interpreted section highlighting the expected amplitude responses for high amplitude BSRs, weak BSRs and for regions with no BSR. This figure also provides a reference where the base of the gas hydrate stability zone (GHSZ) is and why high amplitude BSRs have a large acoustic impedance contrast resulting from the trapped free gas below. Bathymetry map taken from the General Bathymetric Chart of the Oceans (GEBCO) Compilation Group 2019.

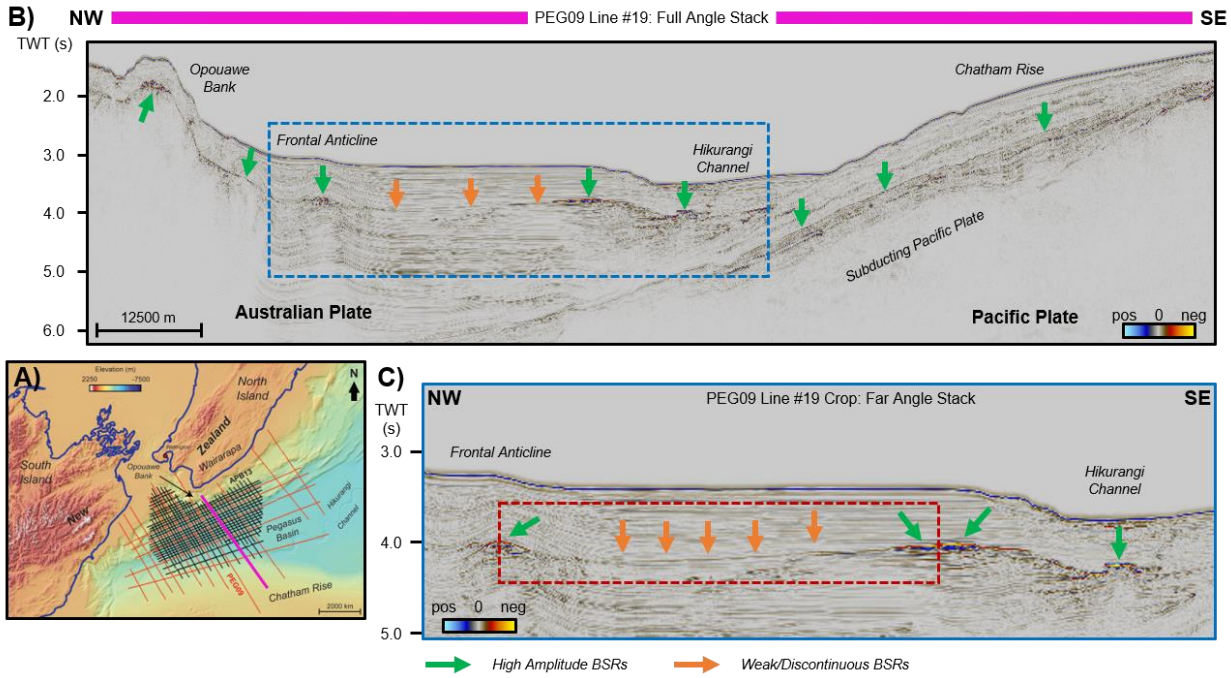

Figure 2-2: A) Study area within the Pegasus Basin, offshore New Zealand. The PEG09 2D survey is denoted in red while the more recent APB13 2D survey is shown in black. B) Shows the entire 2D vertical full angle stack seismic profile of Line 19 from the PEG09 survey, further highlighting key geologic structures and types of BSRs. C) Takes a closer look at the far angle stacks for Line 19 to show the weak/discontinuous BSRs versus the high amplitude BSRs. The far angle stacks helped to better visualize some of the weaker BSRs and further infer the presence of hydrates. The red box shown here references the amplitude section studied in Figure 2-6. Bathymetry map taken from the General Bathymetric Chart of the Oceans (GEBCO) Compilation Group 2019.

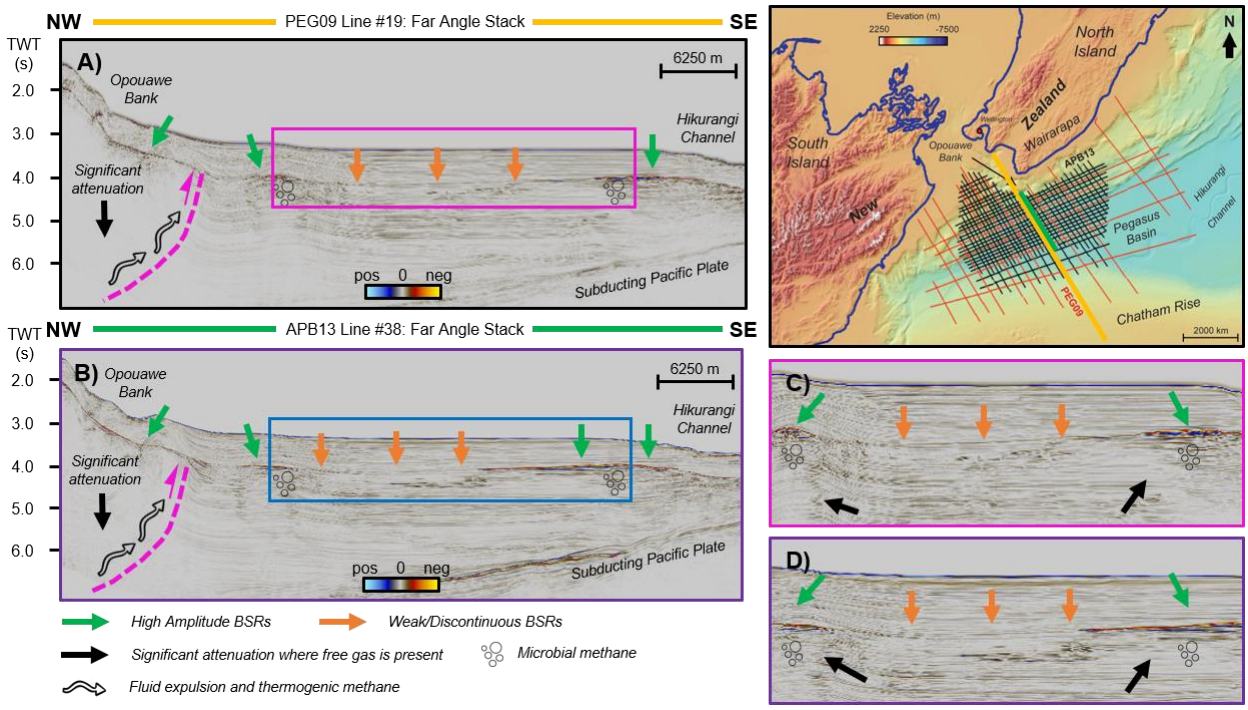

Figure 2-3: A) PEG09 Line 19 B) APB13 Line 38 within the Pegasus Basin, offshore New Zealand. These lines were chosen as they are from two different surveys yet are the closest to each other. C) Shows a zoomed in portion of PEG09 Line 19 to highlight the difference between high amplitude BSRs (shown by the green arrows) and the weak/discontinuous BSRs (shown by the orange arrows). D) shows a zoomed in portion of the APB13 Line 38 also highlighting the difference between high amplitude and weak/discontinuous BSRs. Both surveys show similar high amplitude and weak/discontinuous BSRs. The fluid expulsion and thermogenic methane migration pathways are also shown along with the significant seismic attenuation (black arrows) created from trapped free gas, migrations pathways containing free gas and complex faulting zones (Horizons and faults were modified from Kroeger et al., 2015 and interpreted on a time volume). Fluid expulsion, thermogenic methane pathways and microbial methane modified after Henrys et al. 2009, Plaza-Faverola et al. 2012 and Kroeger et al. 2015. Bathymetry map taken from the General Bathymetric Chart of the Oceans (GEBCO) Compilation Group 2019.

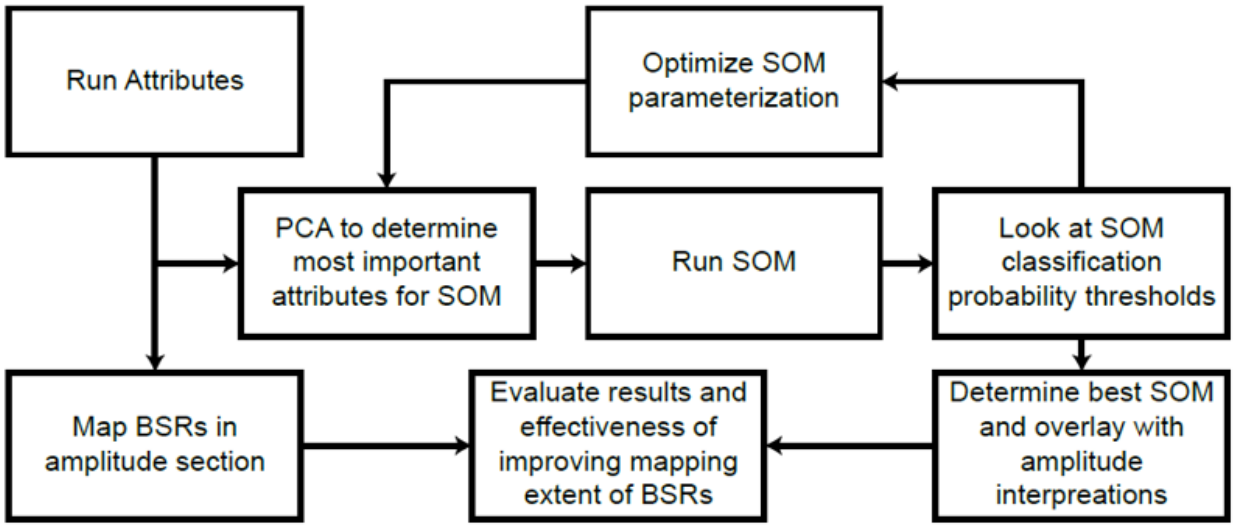

Figure 2-4: Iterative SOM workflow used to evaluate the accuracy and effectiveness of each SOM result. Several combinations of instantaneous and AVA attributes as well as different neuron parameters were evaluated.

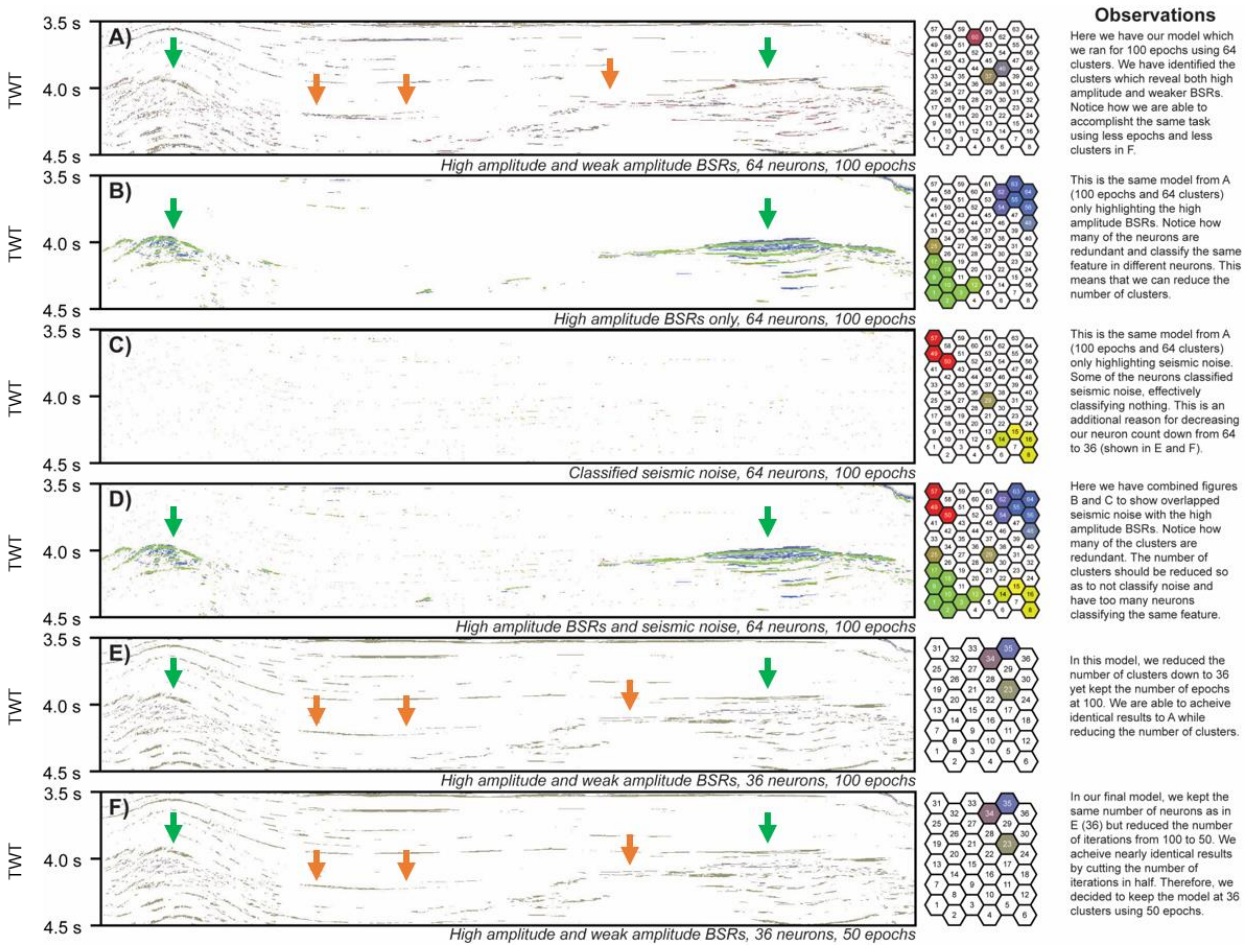

Figure 2-5: Comparison of various SOM models with different epochs and neurons counts run on Line 19 of the PEG09 survey. A) Shows the model with 64 neurons trained for 100 epochs highlighting both strong and weak amplitude BSRs. B) shows that same model with only the high amplitude BSRs whereas C) shows the same model with only classified seismic noise highlighted. D) Shows the SOM model with 64 neurons trained for 100 epochs with classified high amplitude BSRs and seismic noise. Notice how many neurons redundantly classify the high amplitude BSRs and classify seismic noise. The neuron count was then reduced to 36 neurons in E). We then reduced the number of epochs down to 50 in F) to obtain the same result as in E). This shows that by reducing the number of iterations and number of clusters, we are able to obtain the same results from model A) in model F) to achieve a more computationally efficient model. The green arrows represent high amplitude BSRs whereas the orange arrows represent the weak amplitude BSRs better revealed using our model.

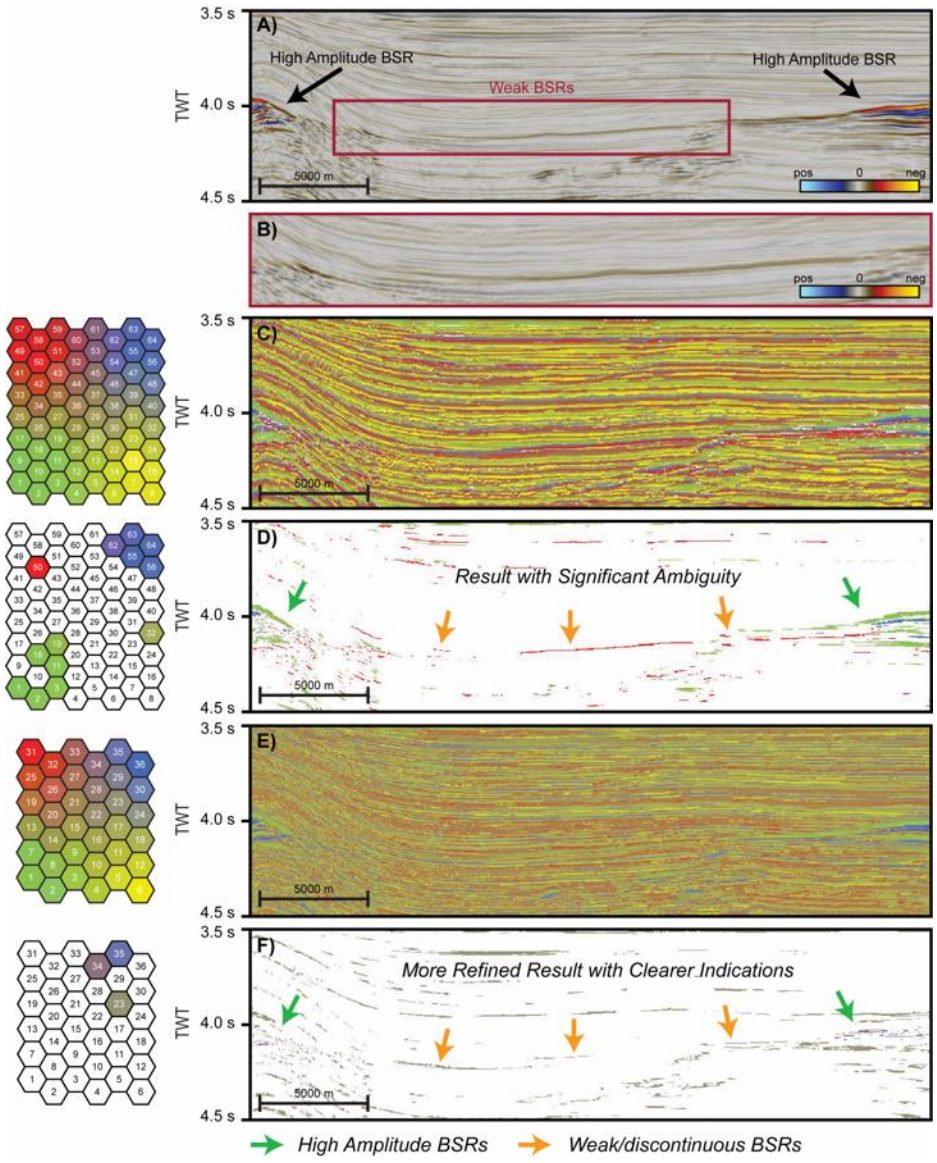

Figure 2-6: Comparison of an unoptimized SOM result compared to an optimized SOM result. A) Shows PEG09 Line 19 amplitude section (refer to Figure 2-2 for location relative to PEG09 2D survey) where weak, discontinuous BSRs are present between two areas of high amplitude BSRs. B) is a closer look at the weak BSR section highlighted in A). C) Shows the result from an optimized SOM with all of the neurons activated and displayed and D) only shows the neurons which highlight the BSRs from C). Although the SOM helps highlight some of the weak BSRs, several similar neurons classified them and the calculation time could be significantly reduced. E) Represents the SOM result with optimized parameters and all neurons displayed whereas F) only shows the neurons which highlight the BSRs. With the SOM parameters optimized, similar results are achieved with a smaller number of neurons and computation time is significantly improved.

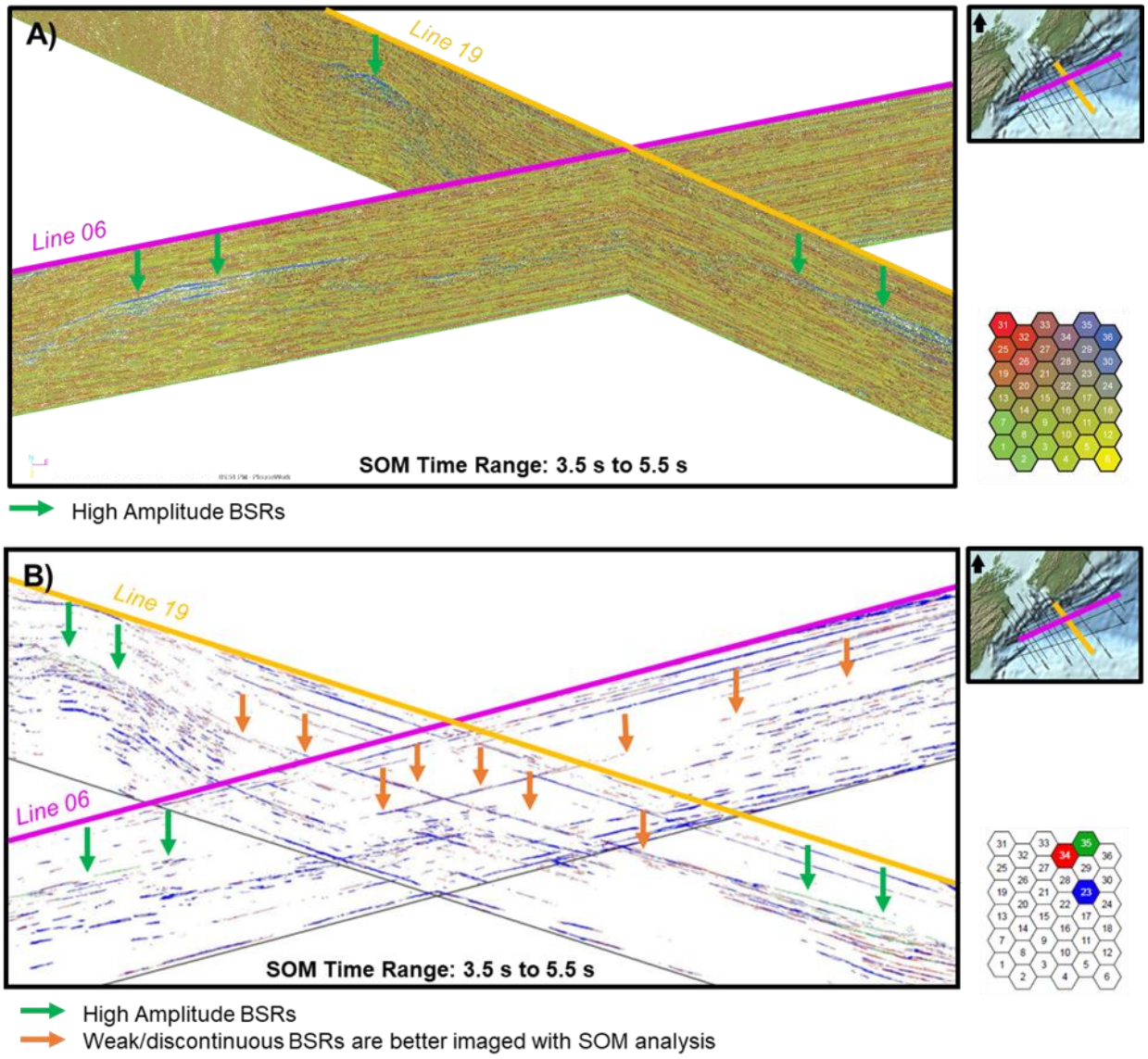

Figure 2-7: A) Raw SOM results for Lines 06 and 19 within the PEG09 2D seismic survey and B) optimized SOM results for Lines 06 and 19 within the PEG09 2D seismic survey revealing the better imaged BSR.

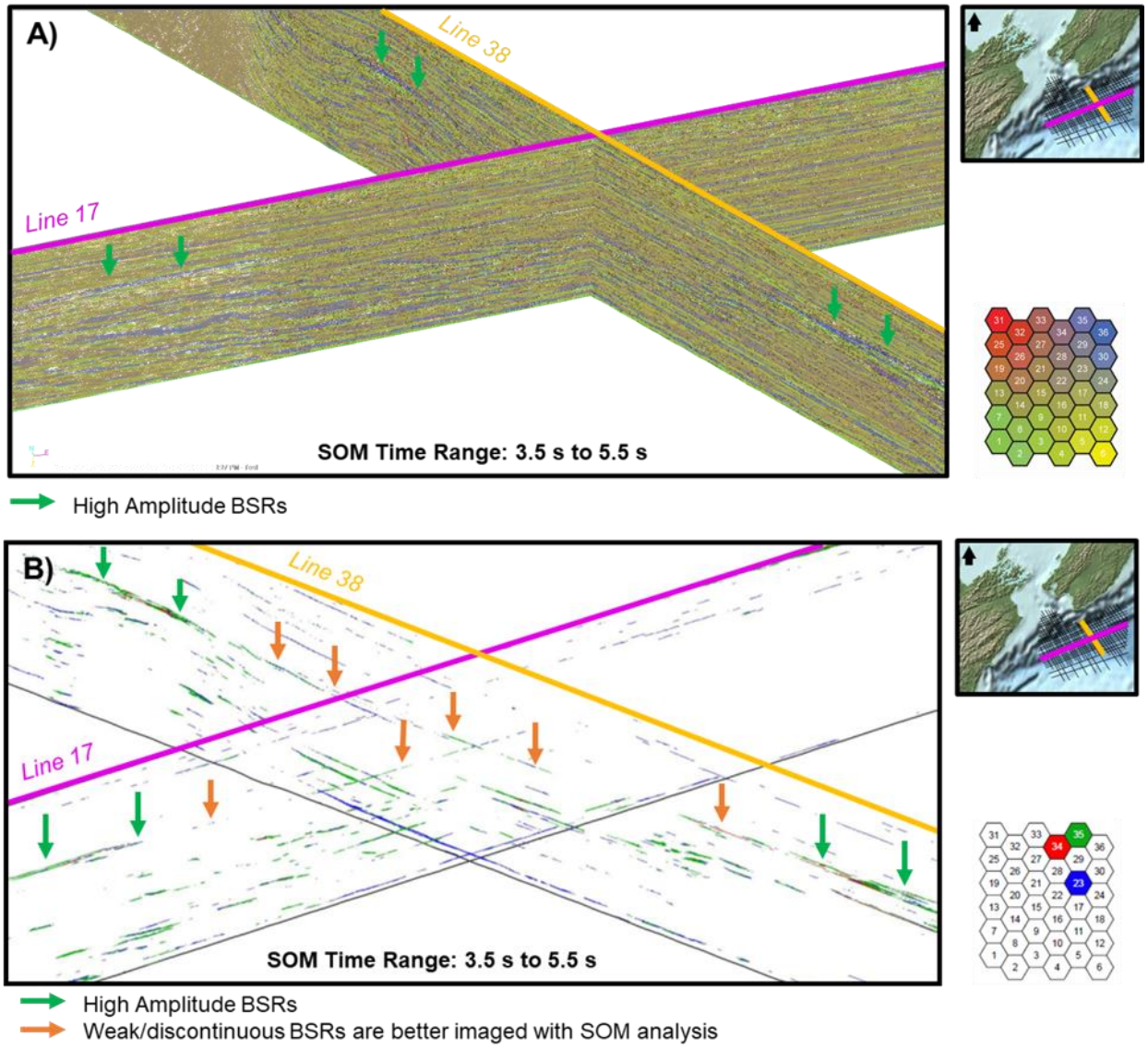

Figure 2-8: A) Raw SOM results for Lines 17 and 38 within the APB13 2D seismic survey and B) optimized SOM results for Lines 17 and 38 within the APB13 2D seismic survey revealing the better imaged BSR.

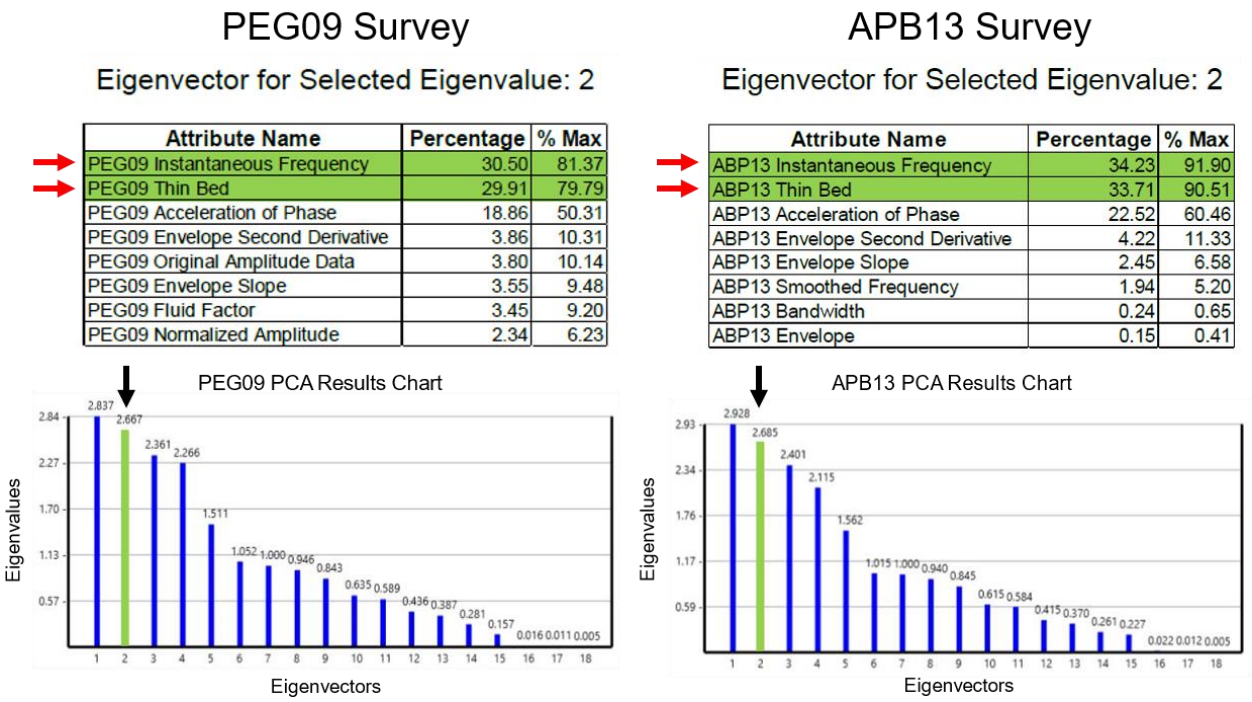

Figure 2-9: Comparison of the PCA results between the PEG09 and APB13 2D seismic surveys showing the evident similarity between them. Attributes are ranked in very similar orders within all eigenvectors with similar eigenvalues (shown by the black and red arrows). These results, along with the similar SOM results, show that this methodology is transferrable.

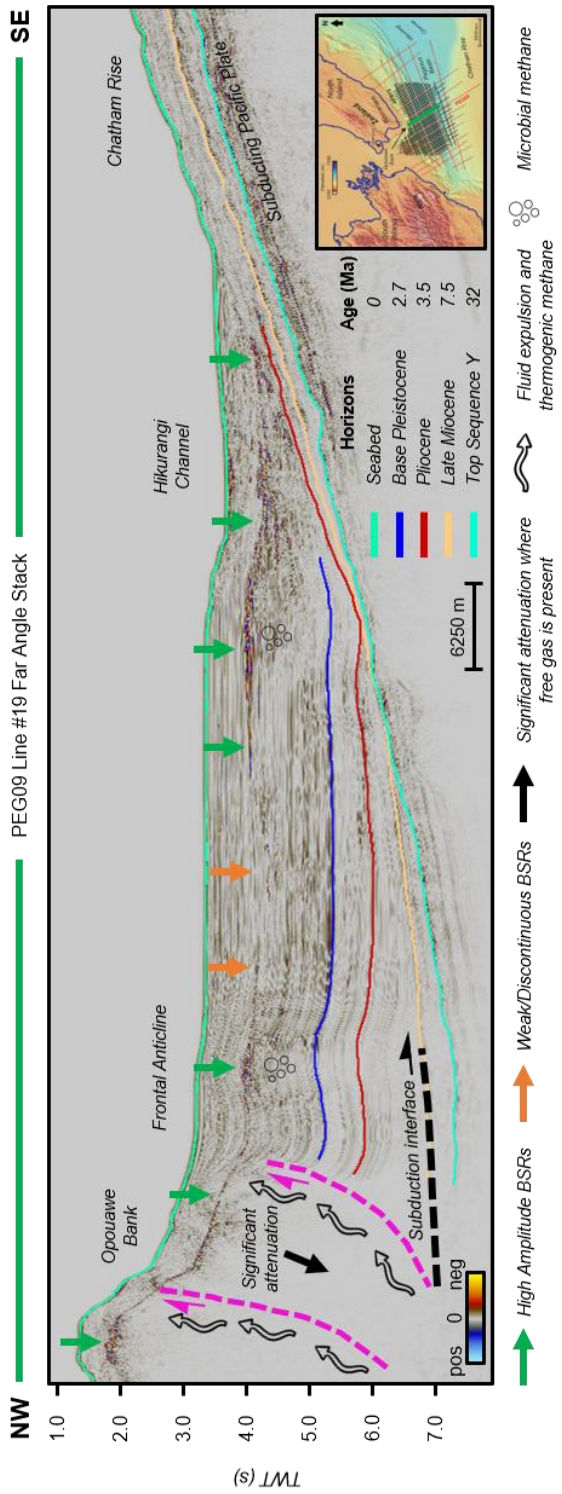

Figure 2-10: Structural and stratigraphic interpretation of Line 19 from the PEG09 survey highlighting the various migration routes for gas within the Pegasus Basin. Horizons and faults were modified from Kroeger et al. 2015 and interpreted on a time volume. Fluid expulsion, thermogenic methane pathways and microbial methane modified after Henrys et al. 2009, Plaza-Faverola et al. 2012 and Kroeger et al. 2015. Bathymetry map taken from the General Bathymetric Chart of the Oceans (GEBCO) Compilation Group 2019.

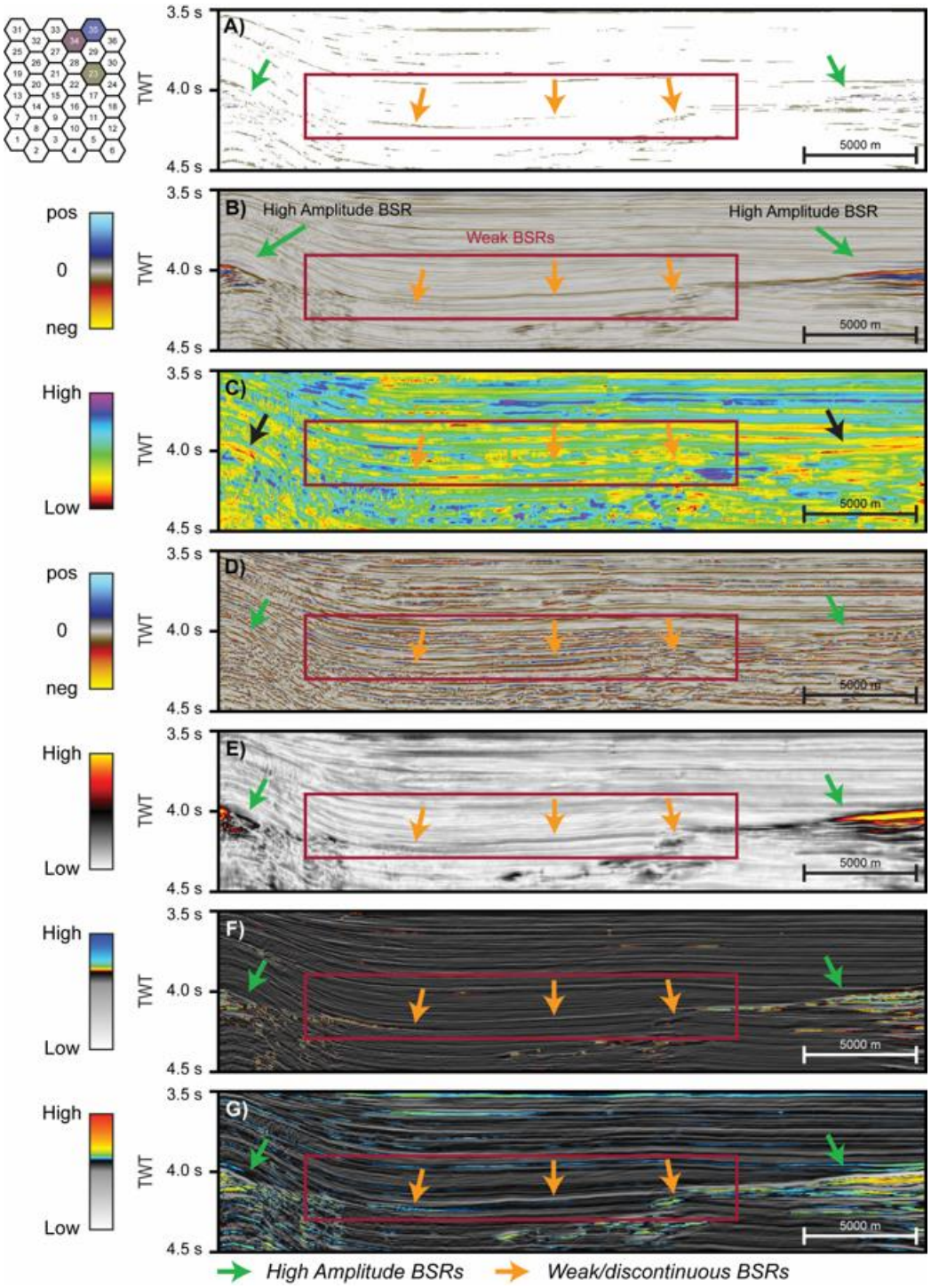

Figure 2-11: A) Optimized SOM results (from Figure 2-6F) for Line 19 of the PEG09 2D survey shown relative to the B) far angle stack amplitude section for Line 19 and all of the seismic attributes used within the SOM: C) instantaneous frequency, D) thin bed, E) sweetness, F) gas indicator, G) shuey fluid factor seismic attributes. It appears that the fluid factor attribute contributed the most towards the SOM result. This is later confirmed by weighted contribution analysis for neurons 23, 34 and 35. Additionally, attributes such as sweetness and AVA attributes were able to detect high amplitude BSR response quite well.

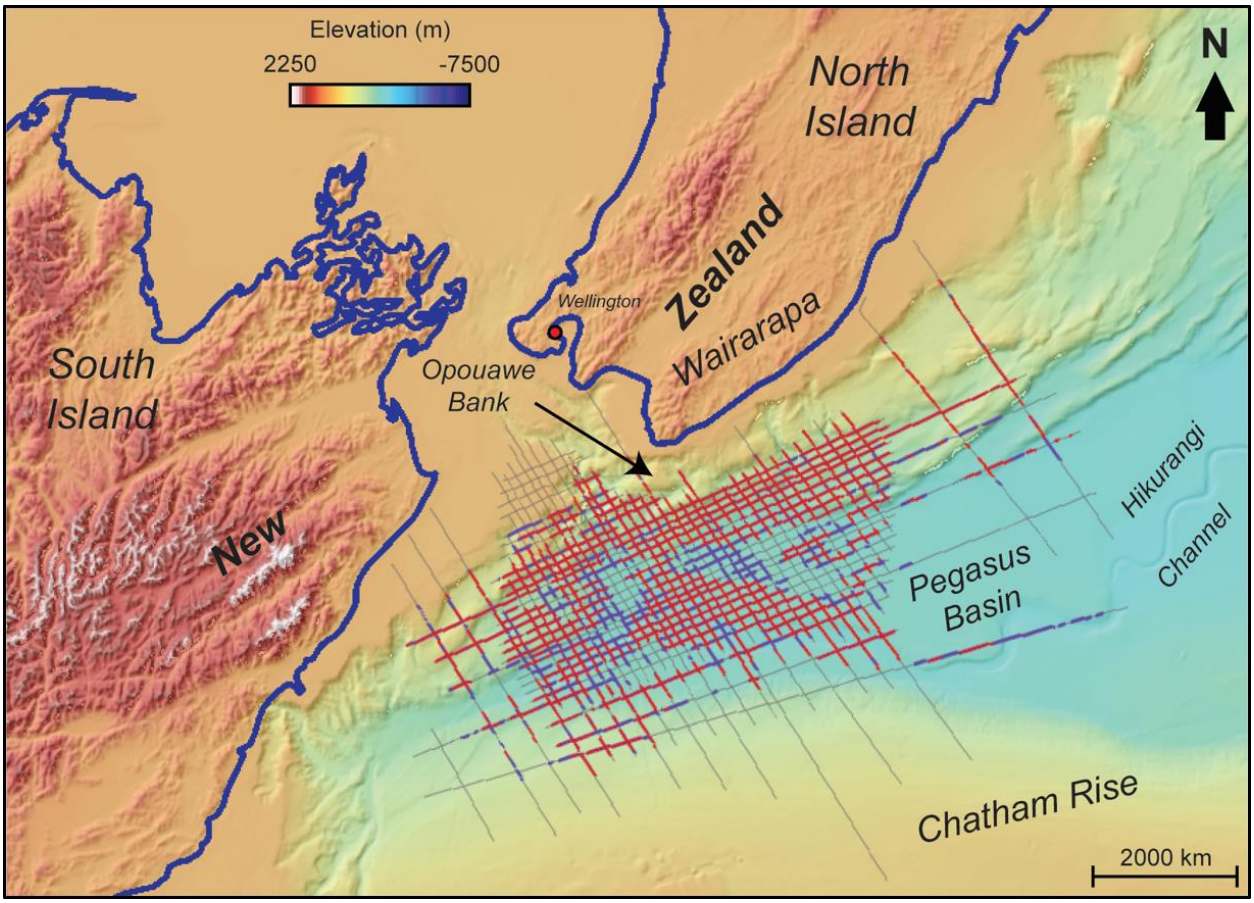

Figure 2-12: Enhanced BSR interpretation capabilities for hydrates in the both the PEG09 and APB13 survey (grey lines) using the proposed SOM. Individual amplitude and seismic attribute interpretations are shown in red whereas the improved interpretation using our proposed SOM model is shown in purple. Bathymetry map taken from the General Bathymetric Chart of the Oceans (GEBCO) Compilation Group 2019.

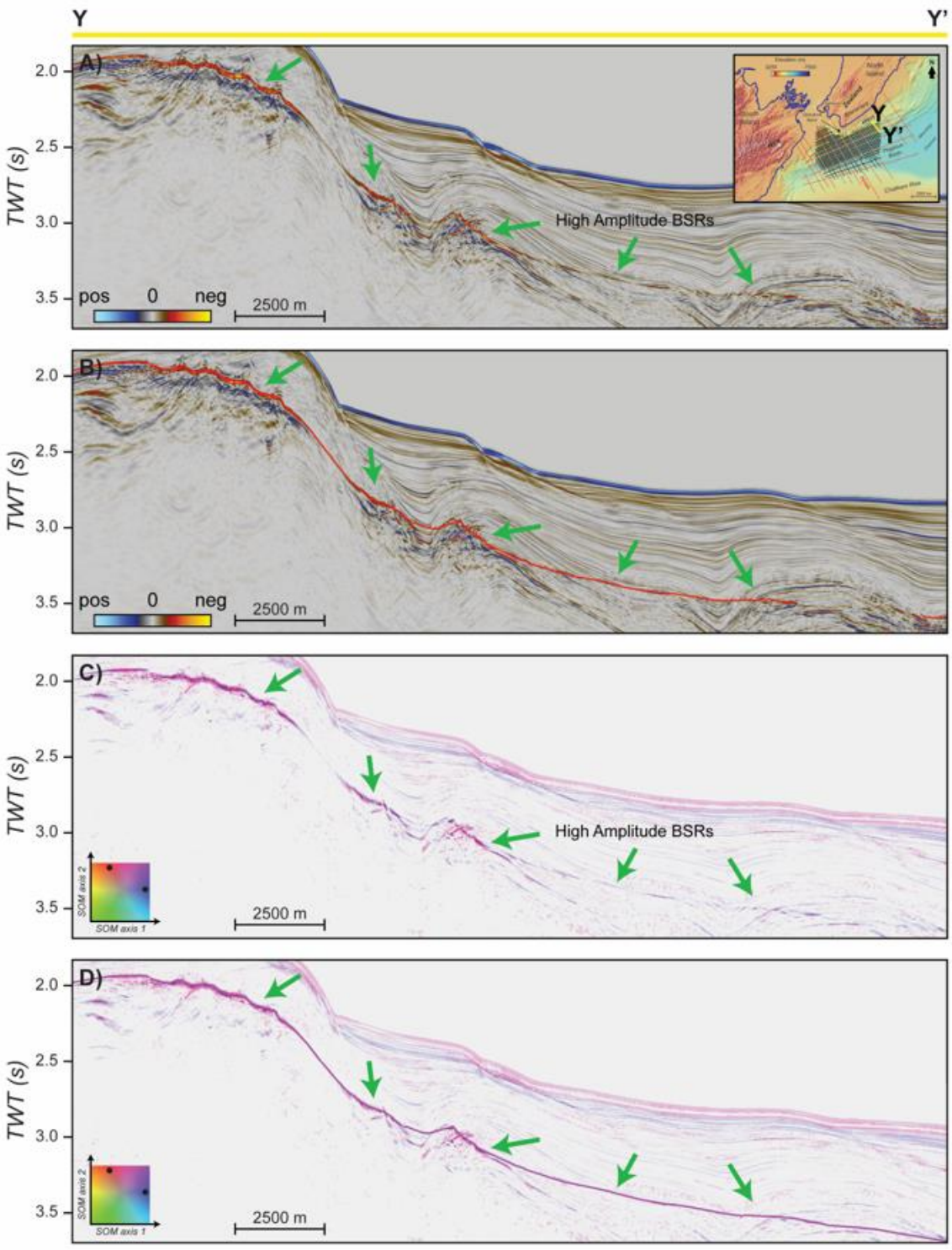

Figure 2-13: A) Far angle stack Line 62 from the APB13 survey with B) the interpreted BSRs (in red) whereas C) shows the SOM results from another software and D) the enhanced interpretability (in purple) as a result of the proposed SOM model. The green arrows are pointing to high amplitude BSRs. Bathymetry map taken from the General Bathymetric Chart of the Oceans (GEBCO) Compilation Group 2019.

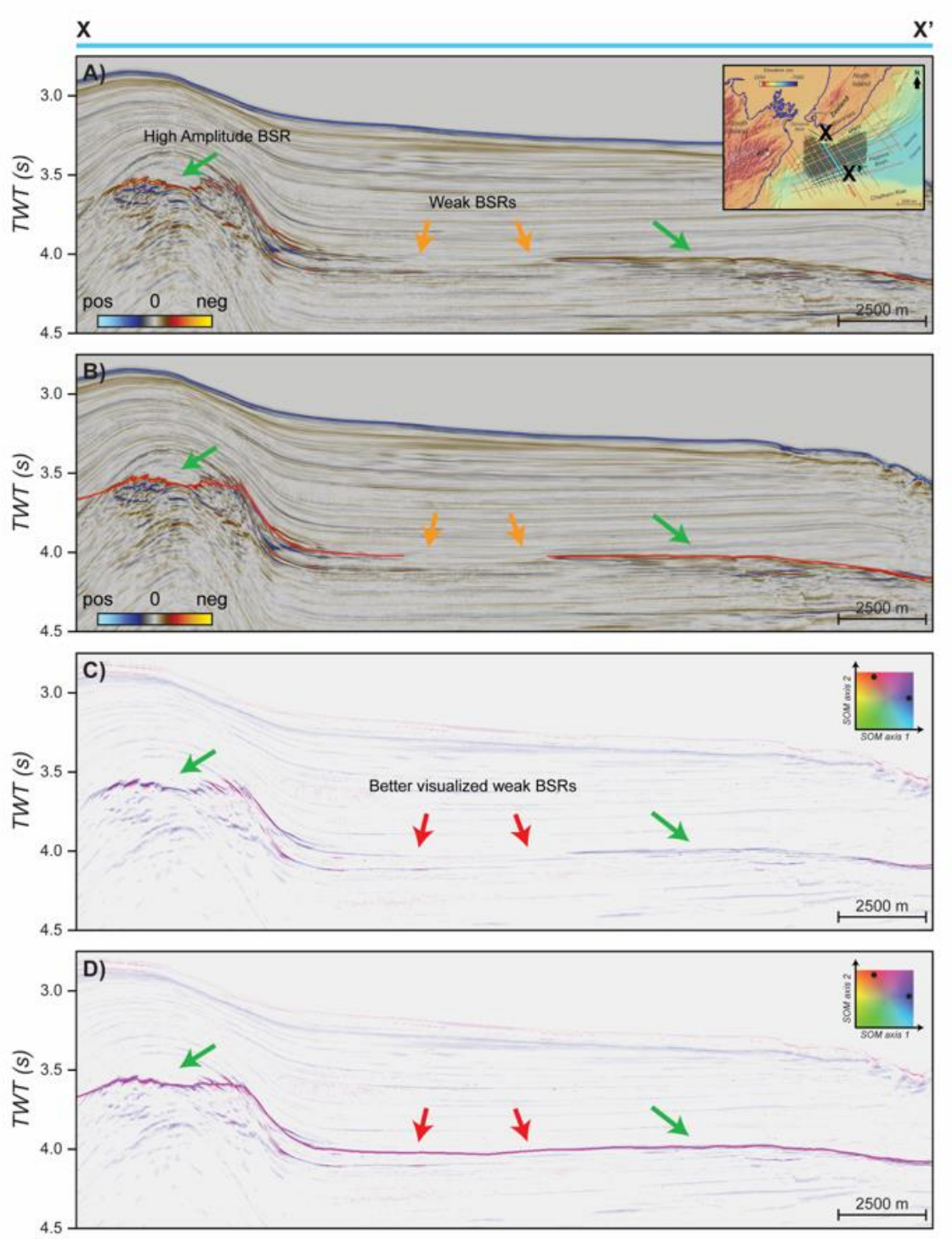

Figure 2-14: A) Far angle stack Line 30 from the APB13 survey with B) the interpreted BSRs (in red) whereas C) shows the SOM results from another software and D) the enhanced interpretability (in purple) as a result of the proposed SOM model. The green arrows are pointing to high amplitude BSRs, the orange arrows are pointing to the weak amplitude BSRs and the red arrows are pointing to the improved imaging of the weak amplitude BSRs using the SOM model. Bathymetry map taken from the General Bathymetric Chart of the Oceans (GEBCO) Compilation Group 2019.

TABLES

Instantaneous Attribute Name	*Definition*	*Uses*	*Sources*
Hilbert	90-degree transform/rotation of the seismic trace complex trace.	These attributes are useful to highlight discontinuities such as faults or lithology changes (Taner et al. 1979; Chopra and Marfurt 2005). These attributes are also helpful for analyzing AVA anomalies as both attributes are proportional to reflectivity (Taner et al. 1979; Subrahmanyam and Rao 2008).	Taner et al. 1979; Chopra and Marfurt 2005; Subrahmanyam and Rao 2008
Envelope	Calculated from the complex trace to highlight the signal's instantaneous energy.		
Envelope Slope	Calculated from the complex trace to highlight the signal's change in reflectivity.		
Instantaneous Frequency	Calculated by taking the time derivative of phase.	This attribute is beneficial for analyzing bed thicknesses and for indicating the edges of low impedance thin beds, such as in the case of weak BSRs (Taner et al. 1979; Subrahmanyam and Rao 2008).	Taner et al. 1979; Subrahmanyam and Rao 2008
Sweetness	Computed by dividing the envelope by the square root of instantaneous frequency.	First discovered by Radovich and Oliveros (1998), sweetness is a relative value helpful for determining relative net-to-gross ratios and to identify "sweet spots" in hydrocarbon exploration (Hart 2008; Koson et al. 2014).	Radovich and Oliveros 1998; Hart 2008; Koson et al. 2014
Thin Bed (also known as thin bed indicator)	Calculated by subtracting the derivative of instantaneous frequency from instantaneous frequency. This is achieved by extracting the location of where instantaneous frequencies change directions or become negative within the seismic data (Taner 2001). Taner (2001) attributes these sign reversals resulting from wavelets arriving close to one another.	Large variations of instantaneous frequency will help identify the location of these thin beds and highlight them within the seismic response (Taner 2001; Subrahmanyam et al. 2008).	Taner 2001; Subrahmanyam and Rao 2008

AVA Attribute Name	*Definition*	*Uses*	*Sources*
Gas Indicator	Calculated by multiplying the intercept by the natural log of the gradient's absolute value.	This attribute has been traditionally used to highlight gas sands with a Class 2 AVA response.	Veeken 2007
Shuey's Fluid Factor	Calculated from using the intercept and the gradient.	Another AVA atrtibute that is useful for highlighting Class 2 AVA sands.	Shuey 1985; Smith and Gidlow 2003

Table 2-1: Definitions, uses and sources for all of the attributes presented within the hydrates study.

REFERENCES

Anardarko New Zealand Ltd (2014a) Seismic Data Processing Report - APB-13-2D Pegasus Basin 2D PEP54858. NZP&M, Ministry of Business, Innovation & Employment (MBIE). New Zealand Unpublished Petroleum Report PR5171.

Anardarko New Zealand Ltd (2014b) APB-13-2D Pegasus Basin 2D Quality Assurance Report PEP 54861 Marine 2D Seismic Survey PEP 54858. NZP&M, Ministry of Business, Innovation & Employment (MBIE). New Zealand Unpublished Petroleum Report PR5172.

Bedle H (2019) Seismic attribute enhancement of weak and discontinuous gas hydrate bottom-simulating reflectors in the Pegasus Basin, New Zealand. Interpretation 7(3):SG11-SG22.

Best AI, Priest JA, Clayton CR, and Rees EV (2013) The effect of methane hydrate morphology and water saturation on seismic wave attenuation in sand under shallow sub-seafloor conditions. Earth and Planetary Science Letters 368:78-87.

Bland KJ, Uruski CI, Isaac MJ (2015) Pegasus Basin, eastern New Zealand: A stratigraphic record of subsidence and subduction, ancient and modern. New Zealand Journal of Geology and Geophysics 58(4):319-343.

Chopra S, Marfurt KJ (2005) Seismic attributes—A historical perspective. Geophysics 70(5):3SO-28SO.

Chopra S, Castagna JP (2014) AVO. Society of Exploration Geophysicists. https ://doi. org/10.1190/1.9781560803201.

Chopra S, KJ Marfurt (2018) Seismic facies classification using some unsupervised machine-learning methods. SEG Technical Program Expanded Abstracts 2018:2056-2060.

Crutchley GJ, Kroeger KF, Pecher IA, Gorman AR (2019) How tectonic folding influences gas hydrate formation: New Zealand's Hikurangi subduction margin. Geology 47(1):39-42.

Crutchley GJ, Maslen G, Pecher IA, Mountjoy JJ (2016) High-resolution seismic velocity analysis as a tool for exploring gas hydrate systems: An example from New Zealand's southern Hikurangi margin. Interpretation 4(1):SA1-2.

Dai J, Xu H, Snyder F, Dutta N (2004) Detection and estimation of gas hydrates using rock physics and seismic inversion: Examples from the northern deepwater Gulf of Mexico. The Leading Edge 23(1):60-66.

Dai J, Snyder F, Gillespie D, Koesoemadinata A, Dutta N (2008a) Exploration for gas hydrates in the deepwater, northern Gulf of Mexico: Part I. A seismic approach based on geologic model, inversion, and rock physics principles. Marine and Petroleum Geology 25(9):830-844.

Dai J, Banik N, Gillespie D, Dutta N (2008b) Exploration for gas hydrates in the deepwater, northern Gulf of Mexico: Part II. Model validation by drilling. Marine and Petroleum Geology 25(9):845-859.

Dewangan P, Mandal R, Jaiswal P, Ramprasad T, Sriram G (2014) Estimation of seismic attenuation of gas hydrate bearing sediments from multi-channel seismic data: A case study from Krishna–Godavari offshore basin. Marine and Petroleum Geology 58:356-367.

Dickens GR (2003) A methane trigger for rapid warming? Science 229(5609):1017-1017. https://doi.org/10.1126/science.1080789.

Dvorkin J, Nur A (1996) Elasticity of high-porosity sandstones: Theory for two North Sea data sets. Geophysics 61(5):1363-1370.

Dvorkin J, Prasad M, Sakai A, Lavoie D (1999) Elasticity of marine sediments: Rock physics modeling. Geophysical Research Letters 26(12):1781-1784.

Dvorkin J, Nur A, Uden R, Taner T (2003) Rock physics of a gas hydrate reservoir. The Leading Edge 22(9):842-847.

Dvorkin J, Uden R (2004) Seismic wave attenuation in a methane hydrate reservoir. The Leading Edge 23(8):730-732.

Ecker C, Dvorkin J, Nur AM (2000) Estimating the amount of gas hydrate and free gas from marine seismic data. Geophysics 65(2):565-573.

Englezos P (1993) Clathrate hydrates. Industrial & Engineering Chemistry Research 32(7):1251-1274.

Faure K, Greinert J, Pecher IA, Graham IJ, Massoth GJ, De Ronde CE, Wright IC, Baker ET, Olson EJ (2006) Methane seepage and its relation to slumping and gas hydrate at the Hikurangi margin, New Zealand. New Zealand Journal of Geology and Geophysics 49(4):503-516.

Field ME, Barber JHJ (1993) A submarine landslide associated with shallow seafloor gas and gas hydrates off Northern California. Submarine landslides: selected studies in the US exclusive economic zone. US Geological Survey 2002:151–157.

Finley PD, Krason J (1988) Geological evolution and analysis of confirmed or suspected gas hydrate localities No DOE/MC/21181-1950, vol 12. Geoexplorers International, Inc., Denver.

GEBCO Compilation Group (2019) GEBCO 2019 grid.

Griffin AG, Bland KJ, Field B, Strogen DP, Crutchley G, Lawrence MJ, Kellett R (2015) Reservoir characterization of the East Coast and Pegasus basins, Eastern North Island, New Zealand. AAPG and SEG International Conference and Exhibition, Melbourne.

Guerin G, Goldberg D, Meltser A (1999) Characterization of in situ elastic properties of gas hydrate-bearing sediments on the Blake Ridge. Journal of Geophysical Research Solid Earth 104(B8):17781-17795.

Haacke RR, Westbrook GK, Hyndman, RD (2007) Gas hydrate, fluid flow and free gas: Formation of the bottom-simulating reflector. Earth and Planetary Science Letters 261(3-4):407-420.

Hart BS (2008) Channel detection in 3-D seismic data using sweetness. AAPG Bulletin 92(6):733-742.

He L, Matsubayashi O, Lei X (2006) Methane hydrate accumulation model for the Central Nankai accretionary prism. Marine Geology 227(3-4):201-214.

Henrys SA, Woodward DJ, Pecher IA (2009) Variation of bottom-simulating-reflection strength in a high-flux methane province, Hikurangi margin, New Zealand. AAPG Memoir 89:481-489.

Hillman JI, Cook AE, Sawyer DE, Küçük HM, Goldberg DS (2017) The character and amplitude of 'discontinuous' bottom-simulating reflections in marine seismic data. Earth and Planetary Science Letters 459:157-169.

Holbrook SW, Hoskins H, Wood WT, Stephen RA, Lizarralde D (1996) Methane hydrate and free gas on the Blake Ridge from vertical seismic profiling. Science 273(5283):1840-1843.

Jolliffe IT (2002) Mathematical and statistical properties of population principal components. In: Joliffe IT (ed) Principal component analysis, 2nd edn. Springer, New York, pp 10-28.

Katz HR (1981) Probable gas hydrate in continental slope east of the North Island, New Zealand. Journal of Petroleum Geology 3(3):315-324.

Katz HR (1982) Evidence of gas hydrates beneath the continental slope, East Coast, North Island, New Zealand. New Zealand Journal of Geology and Geophysics 25(2):193-199.

Kennett JP, Cannariato KG, Hendy IL, Behl RJ (2000) Carbon isotopic evidence for methane hydrate instability during Quaternary interstadials. Science 288(5463):128-133.

Kim HS, Cho GC, Lee JY, Kim SJ (2013) Geotechnical and geophysical properties of deep marine fine-grained sediments recovered during the second Ulleung Basin Gas Hydrate expedition, East Sea, Korea. Marine and Petroleum Geology 47:56-65.

Kohonen T (1990) The self-organizing map. Proceedings of the IEEE 78(9):1464-1480.

Koson S, Chenrai P, Choowong M (2014) Seismic attributes and their applications in seismic geomorphology. Bulletin of Earth Sciences of Thailand 6(1):1-9.

Kroeger KF, Plaza-Faverola A, Barnes PM, Pecher IA (2015) Thermal evolution of the New Zealand Hikurangi subduction margin: Impact on natural gas generation and methane hydrate formation–A model study. Marine and Petroleum Geology 63:97-114.

Kroeger KF, Crutchley GJ, Kellett R, Barnes PM (2019) A 3-D Model of Gas Generation, Migration, and Gas Hydrate Formation at a Young Convergent Margin (Hikurangi Margin, New Zealand). Geochemistry, Geophysics, Geosystems 20(11):5126-5147.

Lewis KB, Collot JY, Lallem SE (1998) The dammed Hikurangi Trough: a channel-fed trench blocked by subducting seamounts and their wake avalanches (New Zealand–France GeodyNZ Project). Basin Research 10(4):441-468.

Liu T, Liu X (2018) Identification of morphologies of gas hydrate distribution based on amplitude variation with angle analysis. Geophysics 83(3):B143-B154.

Makogon YF, Holditch SA, Makogon TY (2007) Natural gas hydrates— a potential energy source for the 21st Century. Journal of Petroleum Science and Engineering 56(1–3):14–31.

Navalpakam RS, Pecher IA, Stern T (2012) Weak and segmented bottom simulating reflections on the Hikurangi Margin, New Zealand—Implications for gas hydrate reservoir rocks. Journal of Petroleum Science and Engineering 88:29-40.

Nimblett J, Ruppel C (2003) Permeability evolution during the formation of gas hydrates in marine sediments. Journal of Geophysical Research Solid Earth, 108(B9).

Plaza-Faverola A, Klaeschen D, Barnes P, Pecher I, Henrys S, Mountjoy J (2012) Evolution of fluid expulsion and concentrated hydrate zones across the southern Hikurangi subduction margin, New Zealand: An analysis from depth migrated seismic data. Geochemistry, Geophysics, Geosystems 13:8.

Priest JA, Best AI, Clayton CR (2006) Attenuation of seismic waves in methane gas hydrate-bearing sand. Geophysical Journal International, 164(1):149-159.

Radovich BJ, Oliveros RB (1998) 3-D sequence interpretation of seismic instantaneous attributes from the Gorgon field. The Leading Edge 17(9):1286-1293.

Riedel M, Willoughby EC, Chopra S (2010) Geophysical characterization of gas hydrates. Society of Exploration Geophysicists, Tulsa.

Roden R, Chen CW (2017) Interpretation of DHI characteristics with machine learning. First Break 35(5):55-65.

Roden R, Smith T, Sacrey D (2015) Geologic pattern recognition from seismic attributes: Principal component analysis and self-organizing maps. Interpretation 3(4):SAE59-SAE83.

Roy A (2013) Latent space classification of seismic facies. Dissertation, University of Oklahoma.

Ruppel CD (2011) Methane hydrates and contemporary climate change. Nature Education Knowledge 2(12):12.

Sacrey D, Roden R (2014) Understanding Attributes and Their Use in the Application of Neural Analysis–Case Histories Both Conventional and Unconventional. Search and Discovery Article 41473.

Shuey RT (1985) A simplification of the Zoeppritz equations. Geophysics 50(4):609-614.

Singh SC, Minshull TA, Spence GD (1993) Velocity structure of a gas hydrate reflector. Science 260(5105):204-207.

Smith GC, Gidlow M (2003) The fluid factor angle and the crossplot angle. SEG Technical Program Expanded Abstracts 2003:185-188.

Spence GD, Haacke RR, Hyndman RD (2010) Seismic indicators of natural gas hydrate and underlying free gas. Society of Exploration Geophysicists, Tulsa.

Subrahmanyam D, Rao PH (2008) Seismic attributes–A review. In: 7th International Conference & Exposition on Petroleum Geophysics, Hyderabad:398-404.

Taner MT (2001) Seismic attributes. CSEG Recorder 26(7):49-56.

Taner MT, Koehler F, Sheriff RE (1979) Complex seismic trace analysis. Geophysics 44(6):1041-1063.

Turco F, Crutchley GJ, Gorman AR, Mountjoy JJ, Hillman JI, Woelz S (2020) Seismic velocity and reflectivity analysis of concentrated gas hydrate deposits on the southern Hikurangi Margin (New Zealand). Marine and Petroleum Geology 120:104572.

Veeken PCH (2006). Seismic Stratigraphy, Basin Analysis and Reservoir Characterization. Elsevier, Boston.

Waite WF, Santamarina JC, Cortes DD, Dugan B, Espinoza DN, Germaine J, Jang J, Jung JW, Kneafsey TJ, Shin H, Soga K (2009) Physical properties of hydrate-bearing sediments. Reviews of Geophysics 47(4):RG4003.

Walsh MR, Hancock SH, Wilson SJ, Patil SL, Moridis GJ, Boswell R, Collett TS, Koh CA, Sloan ED (2009) Preliminary report on the commercial viability of gas production from natural gas hydrates. Energy Economics 31(5):815-823.

Wood WT, Ruppel C (2000) Seismic and Thermal Investigations of the Blake Ridge Gas Hydrate Area: A Synthesis. In: Proceedings of the Ocean Drilling Program, scientific results, Ocean Drilling Program, pp 253-264.

Xu W, Ruppel C (1999) Predicting the occurrence, distribution, and evolution of methane gas hydrate in porous marine sediments. Journal of Geophysical Research Solid Earth 104(B3):5081–5095

Xu H, Dai J, Snyder F, Dutta N (2004) Seismic detection and quantification of gas hydrates using rock physics and inversion. In: Taylor CE, Kwan JT (eds) Advances in the Study of Gas Hydrates. Springer, Boston, pp 117-139.

Yoo DG, Kang NK, Bo YY, Kim GY, Ryu BJ, Lee K, Lee GH, Riedel M (2013) Occurrence and seismic characteristics of gas hydrate in the Ulleung Basin, East Sea. Marine and Petroleum Geology 47:236-247.

Yun TS, Francisca FM, Santamarina JC, Ruppel C (2005) Compressional and shear wave velocities in uncemented sediment containing gas hydrate. Geophysical Research Letters 32:10.

Yun TS, Santamarina JC, Ruppel C (2007) Mechanical properties of sand, silt, and clay containing tetrahydrofuran hydrate. Journal of Geophysical Research Solid Earth 112(B4).

Zhang L, Ge K, Wang J, Zhao J, Song Y (2020) Pore-scale investigation of permeability evolution during hydrate formation using a pore network model based on X-ray CT. Marine and Petroleum Geology 113:104-157.

APPENDIX A

Initial BSR SOM Results and Final BSR SOM Results

This appendix illustrates the various SOMs that were computed for characterizing both high- and weak-amplitude BSRs within the Pegasus Basin, offshore New Zealand before achieving the final SOM (Appendix A, Figures 1a-d). The various attributes and SOM parameters used to compute these are shown under Appendix A, Table 1. While the high- and weak-amplitude BSRs are well highlighted in the first SOM, it took many neurons to illustrate them. However, as we optimized the attributes to be included within the SOM, note how the number of neurons decreases to identify the BSRs present within the section. It took ten neurons with the first SOM, seven neurons with the second SOM, and finally three neurons with the optimized SOM (Appendix A, Figures 1b-d). The final SOM was also able to capture the same features from SOM 1 and 2 with significantly fewer neurons. Thus, the final SOM is more computationally efficient.

Furthermore, there was a prominent laterally continuous feature within SOM 2 which was suppressed in the final SOM results (black arrow in Appendix A, Figure 1b). This feature was not expressed in any of the previous SOMs. The difference between these SOMs was that instantaneous frequency was used in the final SOM whereas it was not included in SOM 2 (Appendix A, Table 1). Therefore, it appears that frequency was instrumental for only highlighting both the high- and weak-amplitude BSRs, and not other features which may be present above the GHSZ.

Finally, the weak BSRs were best highlighted in the final SOM. While there were indications present within SOM 1, they were not as laterally continuous as the weak BSRs in the other SOMs. These weak BSRs were better visualized in the second SOM, however, several neurons were necessary to accomplish this. The final SOM was able to capture the same weak

BSRs present within both SOMs while also requiring significantly fewer neurons. Therefore, the final SOM was not only more computationally efficient, but was also able to better reveal the weak BSRs present within the section.

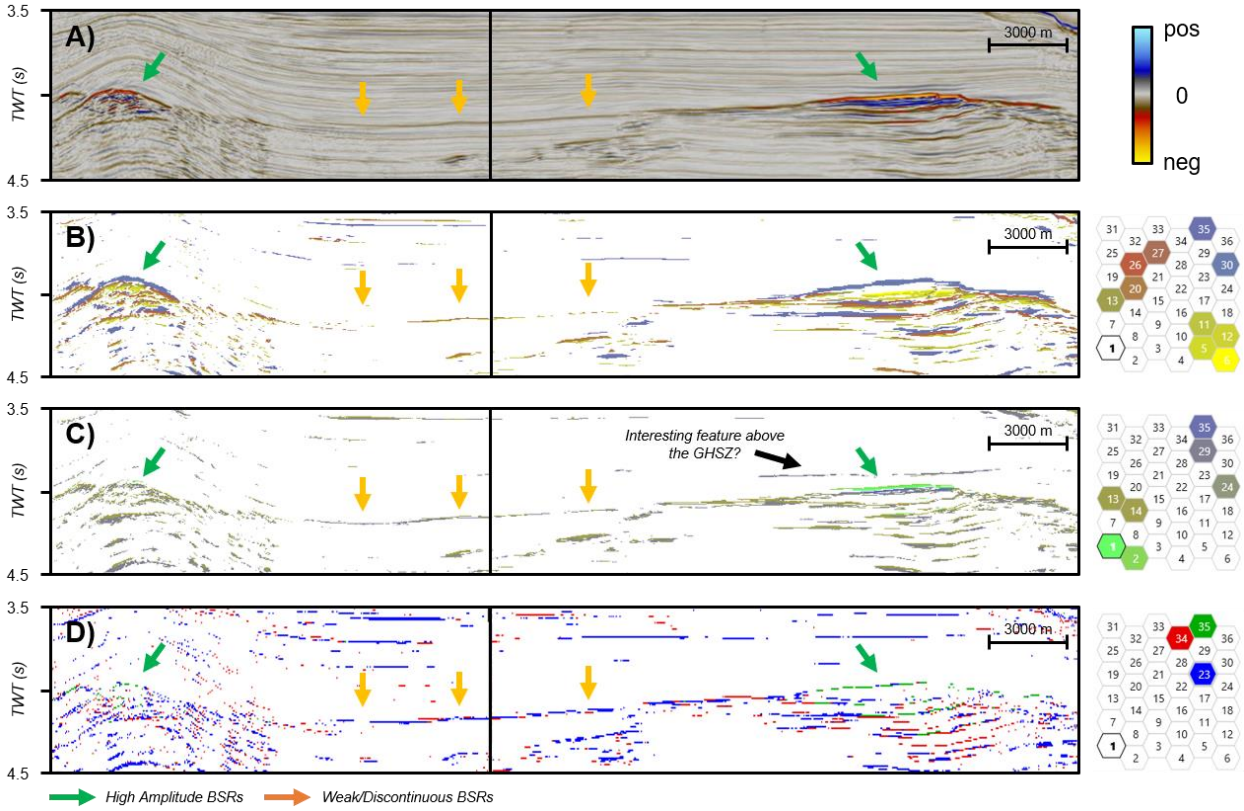

Appendix A, Figure 1: Cropped far angle stack seismic amplitude section of Line 19 from the PEG09 survey with B) SOM 1, C) SOM 2 and D) the final optimized SOM. High amplitude BSRs are shown by the green arrow whereas the weak BSRs are shown by the orange arrow. Table 1 within Appendix A features the various attributes and SOM parameters used to generate these results.

SOM Model	*Attributes Used*	*Iterations*	*Number of Neurons*
B) SOM 1	Relative Acoustic Impedance Sweetness Thin Bed Indicator Far Angle Stack Amplitude Gas Indicator	50	36
C) SOM 2	Relative Acoustic Impedance Sweetness Thin Bed Indicator Far Angle Stack Amplitude Fluid Factor Gas Indicator	50	36
D) Final SOM	Instantaneous Frequency Sweetness Thin Bed Indicator Far Angle Stack Amplitude Fluid Factor Gas Indicator	50	36

Appendix A, Table 1: The various attributes and SOM parameters used for computing the results shown within Appendix A.

CHAPTER 3: Unsupervised Machine Learning, Multi-Attribute Analysis for Identifying Low Saturation Gas (LSG) Reservoirs within the Deepwater Gulf of Mexico and Offshore Australia

Julian Chenin and Dr. Heather Bedle.

The University of Oklahoma, School of Geosciences.

This paper has been submitted to the Journal of Marine Petroleum Geology.

Keywords: machine learning, unsupervised, self-organizing maps, seismic interpretation, direct hydrocarbon indicator, low-saturation gas, Gulf of Mexico, Scarborough gas field

ABSTRACT

An effective method of identifying and discriminating undersaturated gas accumulations remains unsolved, resulting in uncertainty in hydrocarbon exploration. To address this problem, we use an unsupervised machine learning multi-attribute analysis on 3D post-stack seismic data over several blocks within the deepwater Gulf of Mexico, and within the Carnarvon Basin, offshore Australia. Results reveal that low-saturation gas (LSG) reservoirs can be discriminated from high-saturation gas (HSG) reservoirs by using a combination of instantaneous attributes that are sensitive to small amplitude, frequency, and phase anomalies with self-organizing maps (SOMs). This methodology shows promise for de-risking prospects, even if it is not quantitative, particularly in frontier and exploration basins where wells may not exist or be very limited.

However, this method only proved to be successful within the Gulf of Mexico and yielded limited results with the Carnarvon Basin. This difference is most likely due to the Carnarvon Basin having a different amplitude response resulting from a different burial history and fluid saturations

when compared to the Gulf of Mexico. Therefore, this method is non-transferrable, and a different combination of attributes may be needed in other LSG prone basins.

INTRODUCTION

The discrimination of low-saturation gas (LSG) reservoirs (less than 25%) from commercial quantities of gas remains one of the most challenging problems in petroleum exploration (Zhang and Hilterman, 2005). The ambiguity of LSG is primarily due to the elastic properties of gas, in particular the bulk modulus. The shear modulus is nearly insensitive to the type of fluid filling the rock pores. The bulk modulus is a measure of the rock's incompressibility when a force such as a seismic wave is applied. Due to the elastic properties of gas on the bulk modulus on the rock, a small, uneconomical, amount of hydrocarbon gas included in the pore space of the reservoir rock will reflect seismic energy back to the surface in a similar manner as a larger, and economical, accumulation of gas in the pore space (Figure 3-1). These rock physics relationships with the inclusion of gas, will cause an LSG reservoir to have a similar seismic amplitude response to that of a commercial, high-saturation gas (HSG) reservoir (Hilterman, 2001; O'Brien, 2004). The seismic reflection in both LSG and HSG accumulations created a bright amplitude anomaly within certain lithology and pressure regimes within the Gulf of Mexico and within the Scarborough gas field, offshore Australia (Hilterman, 2001; O'Brien, 2004; Ray et al., 2014). These amplitude responses were analyzed within the King Kong/Lisa Anne and Ursa producing fields within the Gulf of Mexico and within the Scarborough gas field, offshore Australia (Figure 3-2a-b).

Amplitude and rock physics analyses conducted by Zhu (2000), O'Brien (2004), Zhou and Hilterman (2010) and Laiw (2011) to better characterize LSG in the subsurface met limited success under specific conditions that cannot be applied in a typical exploration scenario. In recent years, machine learning techniques have gained a significant foothold within the geoscience community. Recent studies (Roden et al., 2015; Roden and Chen, 2017; Sacrey and Roden, 2018;

Chopra and Marfurt, 2019) have shown promising applications of machine learning techniques to reflection seismic data to aid in the interpretation of geologic patterns. Some of these applications are at the sub-seismic resolution scale since machine learning works on a sample interval basis, as opposed to being limited by the seismic wavelet (Roden et al., 2015; Roden et al., 2017).

This study aims to exploit the advances of machine learning and multi-attribute seismic analyses to test the limits and determine if small seismic waveform variations can be detected and properly attributed to low- and partially-saturated gas reservoirs.

GEOLOGIC SETTINGS

King Kong and Lisa Anne Prospects, Offshore Gulf of Mexico

The King Kong and Lisa Anne (KK/LA) prospects lie approximately 160 mi (257 km) south of New Orleans, within the Green Canyon Phase II seismic survey (over Green Canyon Blocks 473 and 474), offshore Gulf of Mexico (Figure 3-2a and 3-3). These prospects occur in Plio-Pleistocene age sediments, share the same geologic model and are mapped on the same reflector in seismic. These deepwater sand reservoirs were deposited in a salt withdrawal basin from a northerly source controlled by underlying salt bodies (O'Brien, 2004). While the King Kong Prospect exhibits structural four-way closure, the Lisa Anne Prospect is positioned on the hanging wall of a large normal fault. Sand quality within both reservoirs is excellent, with porosities of roughly 30% (O'Brien, 2004). Although both prospects appear to have similar seismic amplitude anomalies, the Lisa Anne proved to be an uncommercial prospect having only about 5-25% gas saturation (O'Brien, 2004).

Ursa Gas Field, Offshore Gulf of Mexico

The Ursa field is a prolific producing deepwater field located approximately 130 mi (210 km) southeast of New Orleans within the Shell Mississippi Canyon seismic survey, in Mississippi Canyon, offshore Gulf of Mexico (Figure 3-2a). The deepwater depositional environment of the Mars-Ursa intraslope basin is controlled by cycles of salt tectonics as well as turbidites. Amalgamated channelized sands and sheet sands act as reservoirs for the system and are overlain by condensed sections (Batzle, 2006). Within the Ursa Well #1, several hydrocarbon pay intervals occur at depths of 12,000 ft and from 17,000 to 20,000 ft within Pliocene to Miocene age sands. Multiple, stacked reservoirs pinchout against the flank of the salt dome within the withdrawal basin flanks. Sand quality is also excellent within the field, with an approximate porosity of 25% (Batzle, 2006). However, well log and AVO analysis revealed that one of the upper reservoir intervals was an LSG interval as the velocity was lower than the oil-saturated intervals (Figure 3-4) (Hilterman, 2001).

Scarborough Gas Field, Offshore Australia

The Scarborough gas field is situated on the Exmouth Plateau, in the Carnarvon Basin, offshore Australia (Figure 3-2b) (Han et al., 2018). The plateau is part of a passive margin between continental and oceanic crust formed as a result of the break-up of Australia and India. Sub-horizontal detachment faults dipping towards the Australian continent undercut the plateau at depths of approximately 6.2 mi (10 km) where the continental crust transitions into oceanic crust (Driscoll and Karner, 1998). The plateau, with dimensions of approximately 248 mi by 372 mi (400 km by 600 km), is bounded by transform faults toward the northeast and southwest (Ray et

al., 2014). A complex series of extension, fracture, uplift, truncation and subsidence have affected the plateau since the Mesozoic era (Ray et al., 2014).

The Scarborough reservoir is a three-tiered fan sequence which consists of Early Cretaceous deepwater turbidite sands deposited in a basin-floor fan setting. With a water depth of about 1970 ft (900 m) and situated between 6240 to 6570 ft (1900 to 2000 m) below sea level, the reservoir is roughly 65 to 100 ft (20 to 30 m) thick (Ray et al., 2014; Han et al., 2018; Foschi and Cartwright, 2020). These turbidite sands were sourced from the fluvio-deltaic Barrow Group, located approximately 31 mi (50 km) south of the field (Han et al., 2018). The Lower Fan unit contains the majority of the gas-in-place with porosities between 20-30%, and is overlain by lower net-to-gross and lower quality Middle and Upper fans (Glenton et al., 2013; Han et al. 2018). The areal extent of the reservoir (gas saturation higher than 50%) was defined using five exploration wells and available 3D seismic coverage (Figure 3-5a-c) (Ray et al., 2014).

The geologic backgrounds for the KK/LA and Ursa fields are fairly similar to one another demonstrating comparable porosities, traps and depths. However, the Scarborough field is significantly shallower with a different basin history and may illustrate a different amplitude response from the Gulf of Mexico fields.

AVAILABLE DATA

Access to full-stack 3D datasets for each reservoir measures the amplitude responses of different gas saturations within the Gulf of Mexico, offshore United States and in the Carnarvon Basin, offshore Australia. While gathers and angle-stacks would be beneficial for our analysis, they were unavailable and were therefore not included within this study. Well logs for the King

Kong and Lisa Anne as well as the Ursa Field were also unavailable as they are proprietary. However, a total of five wells were used in Scarborough gas field, offshore Australia.

Within the Gulf of Mexico, two surveys will be used. The Green Canyon Phase II, post-stack seismic survey covers the KK/LA prospects in the Gulf of Mexico (Figure 3-2a). The second seismic dataset, known as the Shell Mississippi Canyon survey, covers the Ursa gas field (Figure 3-2a). Within the Scarborough gas field, offshore Australia, the Scarborough 3D seismic survey is located about 92 mi (240 km) north of Barrow Island and covers the Scarborough gas field (Figure 3-2b). Five wells were available within the Scarborough 3D survey which all contain gamma ray, resistivity, density and neutron porosity. More details about these three seismic surveys can be found under Table 3-2.

METHODOLOGY

Potential gas prospects have been traditionally identified through the use of seismic reflection data with certain types of seismic amplitude anomalies referred to as Direct Hydrocarbon Indicators (DHIs) (Brown, 2011). Dozens of recognized DHIs exist, and they vary dependent on particulars of each basin – such as depth, lithology, pressure and fluid product. Castagna (1993) and Chopra and Castagna (2014) find that gas in Tertiary Gulf of Mexico rocks often exhibits a DHI AVO class 3 behavior that displays a larger amplitude response in the far angles compared to the near angles In full-stack seismic data, the gas is highlighted as a bright spot (Brown, 2011). Additionally, a velocity-sag anomaly is occasionally observed in seismic time volumes beneath large accumulations, where the seismic reflections appear to be pushed down with increasing time due to the presence of lower velocity gas (Brown, 2011). Furthermore, these DHIs can be identified through flat spots (also referred to as a fluid contact reflection), which appears as a horizontal

reflector that cuts across stratigraphy (Brown, 2011). Although these seismic DHIs point to the presence of gas, they cannot quantify gas saturation to a degree where the economic validity of the reservoir can be reliably determined. DHIs are only indicators that hydrocarbons could be present, and thus, are vulnerable to uncertainty. This low-saturation gas phenomenon is pervasive, occurring in hydrocarbon basins globally from the Gulf of Mexico, to the North Sea, and the Niger Delta (Hilterman, 2001; O'Brien, 2004; Batzle, 2006; Khalid and Ghazi, 2013; Wojcik et al., 2016).

Despite decades of research from primarily the rock physics discipline, minimal improvement in identifying gas saturation variations from seismic data has been achieved (Zhu, 2000; Han and Batzle, 2002; O'Brien, 2004; Zhou and Hilterman, 2010; Laiw, 2011; Wu et al., 2014). A robust method of identifying and discriminating potential LSG occurrences remains unsolved, resulting in an additional factor in hydrocarbon exploration risk. Furthermore, even with well logs available, gas saturations may be unclear. Therefore, I will evaluate whether unsupervised machine learning multi-attribute analysis on 3D, post-stack seismic data with self-organizing maps (SOMs) (Figure 3-6) can discriminate between HGS and LGS reservoirs. This methodology shows promise for de-risking prospects, even if it is not quantitative, particularly in frontier and exploration basins where wells are limited or may not exist.

I begin by applying principal component analysis (PCA) methods to a set of seismic attributes from the 3D post-stack seismic survey within the Green Canyon, Gulf of Mexico. PCA is a linear mathematical technique which reduces a set of variables, such as seismic attributes, to a smaller linear combination subset that represents the majority of the independent information's variation (Jolliffe 2002; Sacrey and Roden, 2014). Therefore, PCA will aid in identifying meaningful combinations of attributes that better delineate between low-saturation and high-

saturation gas reservoirs. This method has been applied to a myriad of geophysical applications (Roden et al., 2015; Roden and Chen, 2017; Roden et al., 2017; Chopra and Marfurt 2019). The first principal component accounts for the most variability in the data. After removing the part of the data represented by the first principal component, the second principal component best represents the most variability in the remaining data. For N attributes, the process continues, resulting in N orthogonal principal components. Although the first principal component highlights the largest linear attribute combinations that best represents the variability of the bulk of the data, it may not identify specific features of interest to the interpreter. Therefore, succeeding principal components were evaluated because they may be associated with low-saturation gas characteristics that were not identified with the first principal component. Additionally, many attributes that are useful for characterizing high-amplitude anomalies, such as attributes sensitive acoustic impedance changes, were pre-selected to be used within the PCA. Nonetheless, PCA will reduce these seismic attributes down to a smaller subset that is representative of most of the data's independent variability.

Following PCA analysis, the attributes deemed the most successful for differentiating between different levels of gas saturation is then incorporated in a SOM. Due to the multidimensional nature of PCA results, SOMs are employed to help visualize these complex relationships (Kohonen, 1990). Once the SOM model is optimized for KK/LA prospects within the Green Canyon Phase II survey, the same model will then be applied to the Ursa (Shell Mississippi Canyon 3D seismic survey) and Scarborough (Scarborough 3D seismic survey) fields to evaluate its effectiveness for differentiating between high and low saturation gas reservoirs.

A SOM is a collection of neurons which classify data samples into categories based on their various geological or geophysical properties. Several SOM hyperparameters, such as the

number of neurons and epochs, were evaluated to determine optimal parameterization. These neuron dimensions and number of epochs were used because they are robust enough to highlight minute changes and details within the seismic data, such as varying gas saturations, while also being computationally efficient. The SOM was run on a 5x5 neuron count (total of 25 neurons) with 100 epochs (iterations) over the entire 3D seismic volume. Neuron dimensions higher than 5x5 tended to classify noise within individual neurons displaying insignificant information.

Inlines (IL) containing noticeable gas saturations, such as IL 2391, showed highly anomalous eigenvalues from the PCA results compared to other lines in the survey (Figure 3-7). Further analyzing these anomalous lines revealed that instantaneous attributes which identify changes in amplitude, frequency and phase tended to cluster together to reveal highly anomalous areas within the seismic. For example, the sweetness and envelope seismic attribute ranked as the highest attribute within the second eigenvector for IL 2391 (Figure 3-7). In Figure 3-7, "Percentage" represents the degree to which the attribute contributed towards that specific eigenvector whereas "Percent Total" lists the variance for each of the attributes from all of the eigenvectors. Sweetness and envelope appeared to contribute the most towards the second eigenvector while also representing 62.00% and 58.04% of the variance for all of the eigenvectors. This signifies that those two attributes captured a significant amount of the variability within the dataset. Following a similar workflow used for the second eigenvector, the highest-ranking attributes from the first few eigenvectors were chosen to be incorporated into the SOM analysis over the entire dataset. These attributes are the full-stack amplitude, envelope, Hilbert, cosine of instantaneous phase, relative acoustic impedance and sweetness.

RESULTS

Once the SOM hyperparameters were optimized, I evaluate the number of attributes to use within the SOM model. This selection was determined through iterative PCA and SOM analysis. The optimized SOM model used the following instantaneous attributes: full-stack amplitude, envelope, Hilbert transform of the amplitude, cosine of instantaneous phase, relative acoustic impedance and sweetness. These attributes for the KK/LA SOM are shown in Figure 3-8a-f and Table 3-1 describes the definitions and uses of these attributes.

KK/LA SOM Results

The goal of the multi-attribute analysis is to qualitatively attempt to distinguish between high and low saturation gas reservoirs. The undersaturated Lisa Anne prospect exhibits a similar amplitude and seismic attribute response to the one observed for the higher-saturated King Kong prospect (Figure 3-8a-f). However, when using an unsupervised, multi-attribute analysis, the King Kong prospect can be differentiated from the undersaturated Lisa Anne prospect (Figure 3-9a-c). Figure 3-9a highlights two very bright amplitude anomalies known as the KK/LA prospects whereas Figure 3-9b shows the raw SOM result for the same line with all of the neurons highlighted. Figure 3-9c displays the SOM results displayed with the anomalous neurons of interest (Neurons 11 and 16). These neurons show the data points exhibiting a probability threshold of less than 10%, meaning that they only had a 0-10% chance of being classified within those clusters. By using this probability cutoff, the SOM highlights the highly anomalous data points that had less than a 10% chance of being grouped with the 25 candidate neurons, thereby displaying anomalous attribute responses. Other neurons grouped noise or different geologic features such as bedding, and other lithology variations. In Figure 3-9c, the top and base of the King Kong prospect

is well defined with the Lisa Anne prospect effectively suppressed and undefined. A 3D analysis revealed that the SOM results continuously follow the amplitude anomalies observed in the seismic data. This continues throughout the two reservoir intervals, with the King Kong reservoir extent clearly defined and the Lisa Anne extents remaining indiscernible (Figure 3-9c).

Ursa SOM Results

The KK/LA SOM model was then applied to the Shell Mississippi Canyon 3D seismic survey over the Ursa gas field, offshore Gulf of Mexico. I used the same seismic attributes that were used in the KK/LA SOM. The attributes for the Ursa SOM are shown in Figure 3-10a-f. Well log and AVO analysis from Hilterman (2001) revealed that one of the upper reservoir intervals was an LSG interval (Figure 3-4 and 3-10a). In Figure 3-10a-f, the LSG interval is marked by circle 1 whereas the productive hydrocarbon intervals are marked by circles 2-5. Looking at all of the attribute responses in Figure 3-10a-f, the LSG interval demonstrates a similar response to the higher hydrocarbon saturated reservoirs in the lower intervals. However, once all of the attributes were combined using the SOM, the LSG interval becomes significantly smaller and less continuous compared to the higher saturated hydrocarbon intervals (Figure 3-11a-c). The LSG interval appears significantly more continuous in the amplitude section of Figure 3-11a and the raw SOM section with all of the neurons highlighted whereas it is less apparent and discontinuous in Figure 3-11c. Figure 3-11c is the same SOM from Figure 3-11b with only the neurons of interest displayed with a probability threshold of 10% applied. The prolific hydrocarbon intervals below the LSG interval appear to be more continuous in the SOM result observed in Figure 3-11c. However, the LSG interval is still somewhat apparent in the Ursa SOM whereas the LSG interval is almost indiscernible in the KK/LA SOM (Figure 3-9b). A recent study by Batzle (2006)

conducted a detailed, 3D reservoir model using fluid substitution to better characterize the Ursa LSG interval. The report found that the Ursa LSG zone may have a higher saturation than was originally thought and could be a commercial hydrocarbon zone (Batzle, 2006). Therefore, this could be a reason why the Ursa LSG zone is still visible in the SOM results, albeit significantly less continuous than the other hydrocarbon intervals. Future work will involve obtaining well data, such as sonic logs, to better characterize the hydrocarbon intervals.

Scarborough SOM Results

Once the SOM was successfully applied to the KK/LA prospects and to the Ursa gas field, the model was then applied to the Scarborough gas field, offshore Australia. The same seismic attributes from the KK/LA and Ursa SOM are shown for the Scarborough gas interval in Figure 3-12a-f. The seismic attributes taken over the Scarborough gas interval exhibit similar responses to one another, where the individual attributes provide no indication of varying gas saturation levels (Figure 3-12a-f). However, once the individual attributes are incorporated together into a SOM, the saturation of the Scarborough gas field can be better characterized (Figure 3-13a-c). A study by Ray et al. (2014) characterized the areal extent of the Scarborough reservoir by applying a Bayesian inversion on controlled source electromagnetic (CSEM) data and from five exploration wells and available 3D seismic coverage (Figure 3-5b). From their synthetic studies, they were able to map the outline of the Scarborough reservoir where gas saturation was higher than 50%. The Scarborough SOM result with a probability threshold of 10% applied appears to match quite well with the saturation outline proposed by Ray et al. (2014) (Figure 3-13c). However, a closer comparison between the amplitude section and SOM result reveals that they are quite similar to one another and map similar extents (Figure 3-13a-c). Therefore, it appears that the SOM model

is limited to better characterizing relative saturations between reservoirs in the same seismic survey. Future work will involve better characterizing the Scarborough gas interval to determine if there are higher saturation locations within the reservoir that would be optimal for further production.

DISCUSSION

Taking a closer look at individual neuron weights from the SOMs, some attributes appeared to represent the entire variability of the dataset while other attributes appeared to contribute only to an individual neuron to represent the amplitude anomalies. Overall, the clustering results from the KK/LA SOM revealed that the instantaneous envelope had a total independence of 35.2%, followed by sweetness with 33.9% and relative acoustic impedance with 12.9%. Total independence represents the weight that the attributes played during clustering over the entire dataset. Therefore, these three attributes clustered 82.0% of the data with the remaining attributes, such as the cosine of instantaneous phase, the Hilbert transform and the full-stack amplitude, further delineated these clusters to differentiate between low and high saturation gas reservoirs. Notice that while these three attributes represented 82.0% of the dataset, they were not always the most prominent within Neurons 11 and 16. Attributes such as the Hilbert, contributed nearly 30% towards Neuron 16 whereas it only represented 11.4% of KK/LA's independent variability (Figure 3-14a). Therefore, the Hilbert attribute played a significant role in classifying the anomalous amplitude responses in the KK/LA SOM. A similar relationship is also observed within the Ursa SOM where the instantaneous envelope, sweetness and relative acoustic impedance, represented 60% of the data's variance compared to the cosine of instantaneous phase, the Hilbert and the full-stack amplitude, which represented the remaining 40% (Figure 3-14b). Yet, these three attributes

did not always have the highest neuron independence. Notice how the Hilbert transform contribution to Neuron 20 of the Ursa SOM contributed over 25% towards that cluster whereas it only represented 14.3% of Ursa's independent variability (Figure 3-14b). This same observation also occurs for Neurons 11 and 16 in the KK/LA survey (Figure 3-14a).

However, when looking at the Scarborough SOM clustering results, an opposite relationship is observed from the KK/LA and Ursa SOMs (Figure 3-14c). Seismic attributes such as the cosine of instantaneous phase, the full-stack amplitude and relative acoustic impedance now represent approximately 85.7% of the independent data's variability when this relationship was the inverse in the KK/LA and Ursa SOMs (Figure 3-14c). Yet these attributes consistently contributed the most towards classifying anomalous amplitudes in Neurons 21, 24 and 25 while the other attributes complimented the classification (Figure 3-14c). In fact, now we observe that attributes such as sweetness and the instantaneous envelope represented 0% of the independent data's variability and played a minor role in the individual neuron classifications. These null values indicate that the KK/LA and Ursa SOM is not properly optimized for the Scarborough gas field (Figure 3-14a-c). These SOM differences could be attributed to different amplitude responses from two different basins, meaning that the amplitude responses with the Gulf of Mexico are different than the amplitudes in the Scarborough gas field. These differences could be due to different burial histories and pressure regimes (Avseth et al., 2013; Chopra and Castagna, 2014). They could also be due to differences in fluid saturations, such as gas and brine (Han and Batzle, 2004; Avseth et al. 2013). Based on these results, the SOM models are only optimized for the within the Gulf of Mexico, as was noted within the KK/LA and Ursa fields (Figure 3-9c and 3-11c), whereas a new combination of attributes is required for the Carnarvon Basin, as was observed within Scarborough SOM (Figure 3-13c). Additionally, it is important to note that these SOMs all used a probability

threshold of 10% to better represent the anomalous data points within the neurons. Therefore, these neurons are highlighting the data points which only had a 0-10% chance of being classified within those clusters. This probability threshold of the model further enhances the visualization capabilities for the interpreter as it allows them to better capture the highly anomalous responses within the data which is not necessarily easily visualized through seismic amplitude and attributes profiles.

Studies from Taner (1979), Taner (2001) and Chopra and Marfurt (2005) noted that instantaneous envelope is useful for highlighting lithology, porosity and hydrocarbons since the attribute is sensitive to subtle changes in acoustic impedance. Additionally, the instantaneous envelope attribute is derived using the Hilbert transform to illustrate the signal's instantaneous energy, which means that it is also using the complex portion of the seismic trace (Taner et al., 1979; Chopra and Marfurt, 2005). Therefore, this attribute could be effective for capturing the subtle amplitude differences between low and high-saturation gas reservoirs within both the real and imaginary seismic trace. When the instantaneous envelope is used in combination with other attributes that are good for identifying DHIs, such as sweetness and relative acoustic impedance, the SOM can qualitatively differentiate between high and low gas saturations in the KK/LA and Ursa fields (Figures 3-9a-c and 3-11a-c). Additionally, attributes such as Hilbert and the cosine of instantaneous phase that are useful for analyzing AVO anomalies and highlighting bed continuity respectively could be further complimenting the other attributes to better classify the anomalous amplitude responses within the SOM (Taner et al., 1979; Chopra and Marfurt, 2005). However, this method proved to be limited in the Scarborough gas field as the results yielded limited qualitative information about reservoir saturation (Figure 3-14a-c). Yet, the Scarborough SOM did

manage to highlight the amplitude anomaly created by the gas fairly well. More work is needed to optimize the SOM model for the Scarborough gas field.

Finally, another important note to consider for LSG is detailed consideration of containment. Most LSG is in a sprung trap – a gas accumulation that leaked from seal failure and residual gas remains (5% to 25% gas saturation) (O'Brien, 2004; Hilterman, 2001; Wojcik et al., 2016; Foschi and Cartwright, 2020). O'Brien (2004) noted that hydrocarbon leakage up the regional normal fault may have been possible for the Lisa Anne prospect. His observed shallow bright spots due to gas pockets and water bottom coring (O'Brien, 2004). While this does decrease the risk hydrocarbon migration, it does suggest an increased risk in containment (O'Brien, 2004). Furthermore, while Hilterman (2001) did not discuss seal integrity in detail, Wojcik et al. (2016) note the importance of incorporating seal risking analysis within other turbidite reservoirs within the Gulf of Mexico. Finally, Foschi and Cartwright (2020) observed seal failure within the Scarborough gas field and characterized a 100 km^2 (38 mi^2) wide leakage zone with more than 500 pockmarks. This suggests that there could be some LSG prone regions within the field. However, many of the wells within the field have considerably large gas saturations (Han et al., 2018). When looking at the SOM results, this is not readily apparent, especially in the case of the unoptimized Scarborough SOM result (Figures 3-9c, 3-11c, and 3-13c). However, seal failure analysis has shown promising results for further characterizing LSG reservoirs and future work would incorporate a detailed seal analysis of the discussed reservoirs (Laiw, 2011; Wojcik et al., 2016; Foschi and Cartwright, 2020).

CONCLUSIONS

Preliminary results suggest that instantaneous attributes which detect changes in the amplitude, frequency and phase tend to cluster together in the PCA to reveal highly anomalous areas within the 3D seismic data volume. SOM results highlighted the top and base of the King Kong prospect while the Lisa Anne LSG prospect remained undetected, showing that there is a noticeable difference between both prospects (Figure 3-9c). Upon applying the KK/LA SOM to the Ursa gas field, the

SOM showed that the Ursa LSG interval becomes significantly suppressed and less continuous compared to the higher saturated hydrocarbon intervals present within the lower intervals (Figure 3-11c). Although the Ursa LSG interval is still apparent in the SOM whereas it was almost indiscernible in the KK/SOM, a study by Batzle (2006) found that the LSG zone may have a higher saturation than was originally thought and could be a commercial hydrocarbon zone. Although these results may not give a definitive saturation result, it does highlight a stark difference between both prospects.

However, it appears that the method is limited to only differentiating between relative hydrocarbon saturations within the same seismic survey. Upon further analyzing the neuron clusters, attributes such as the instantaneous envelope and sweetness represent 0% of the independent data within the Scarborough SOM (Figure 3-14a-c). This suggests that the combination of attributes is unoptimized for the Scarborough SOM. This is most likely due to the Scarborough gas field having a different amplitude response resulting from a different burial history and fluid saturations when compared to the Gulf of Mexico (Avseth et al., 2013; Chopra and Castagna, 2014).

In the instance of a neighboring prospects (as was the case with the KK/LA prospects) or for stacked reservoir systems (such as the Ursa gas field), these results can further be incorporated in hydrocarbon exploration risking to better understand DHIs in the subsurface and prevent uneconomic wells from being drilled. Individually, some of these attributes have no success in differentiating between high and low saturation gas prospects. However, employing a multi-attribute analysis provides clearer insight and confidence into delineating between high and low saturation gas reservoirs. Although not currently available, supplementary research will incorporate seismic gathers, angle stacks, and well data into this method to further improve results.

ACKNOWLEDGEMENTS

We would like to acknowledge USGS National Archive of Marine Seismic Surveys (NAMSS) and the Bureau for Ocean Energy Management (BOEM) for access to the Green Canyon Phase II 3D seismic survey (G3D201407-02), the Shell Mississippi Canyon 3D seismic survey (G3D1304-002A through C) as well as the protraction grid and seafloor outlines. We would like to also thank the Australian government for providing open access to the Scarborough 3D seismic survey. The authors would like to give additional thank you to Geophysical Insights, Schlumberger, and ESRI for software license donations to the University of Oklahoma. We would like to also thank AASPI (Attribute-Assisted Seismic Processing and Interpretation) consortium for their software package and the SDA (Subsurface Detective Agency) consortium for their much-appreciated feedback. Finally, thank you to Mike Forrest and Rocky Roden for their valuable insights and recommendations for improving this manuscript.

FIGURES

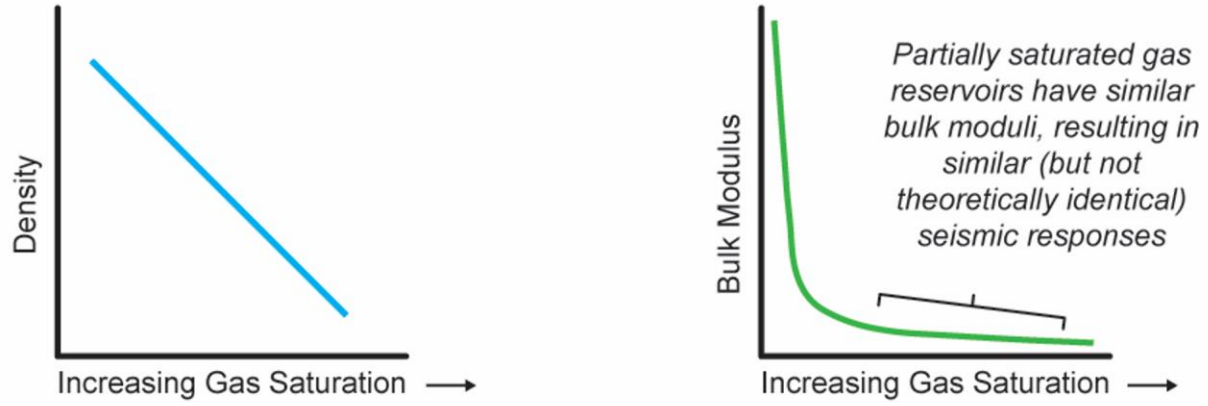

Figure 3-1: Change in rock properties with increasing gas saturation. The bulk modulus quickly decreases with a relatively small amount of gas saturation. This bulk modulus similarity between low and high gas saturation is the crux of the LSG gas differentiation problem.

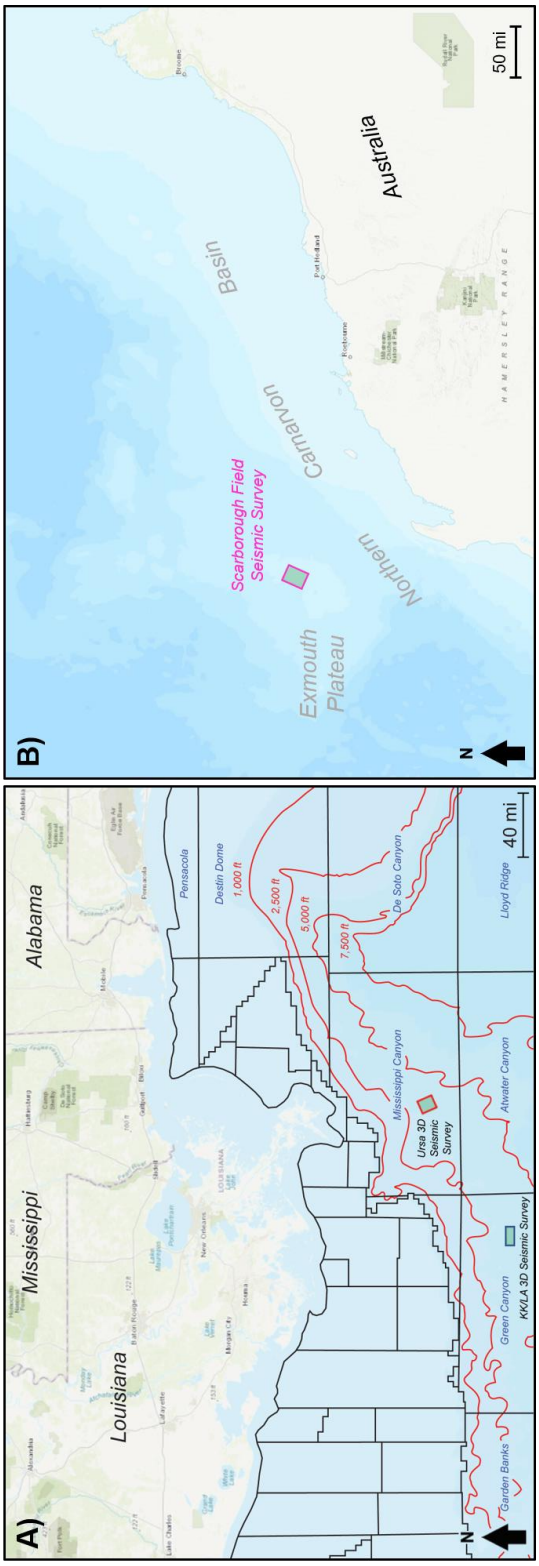

Figure 3-2: Location of the 3D seismic surveys used in this study. Two of these datasets are located A) offshore Gulf of Mexico while the other dataset is located B) offshore Australia within the Northern Carnarvon Basin. Gulf of Mexico protraction grid and seafloor outlines taken from the BOEM.

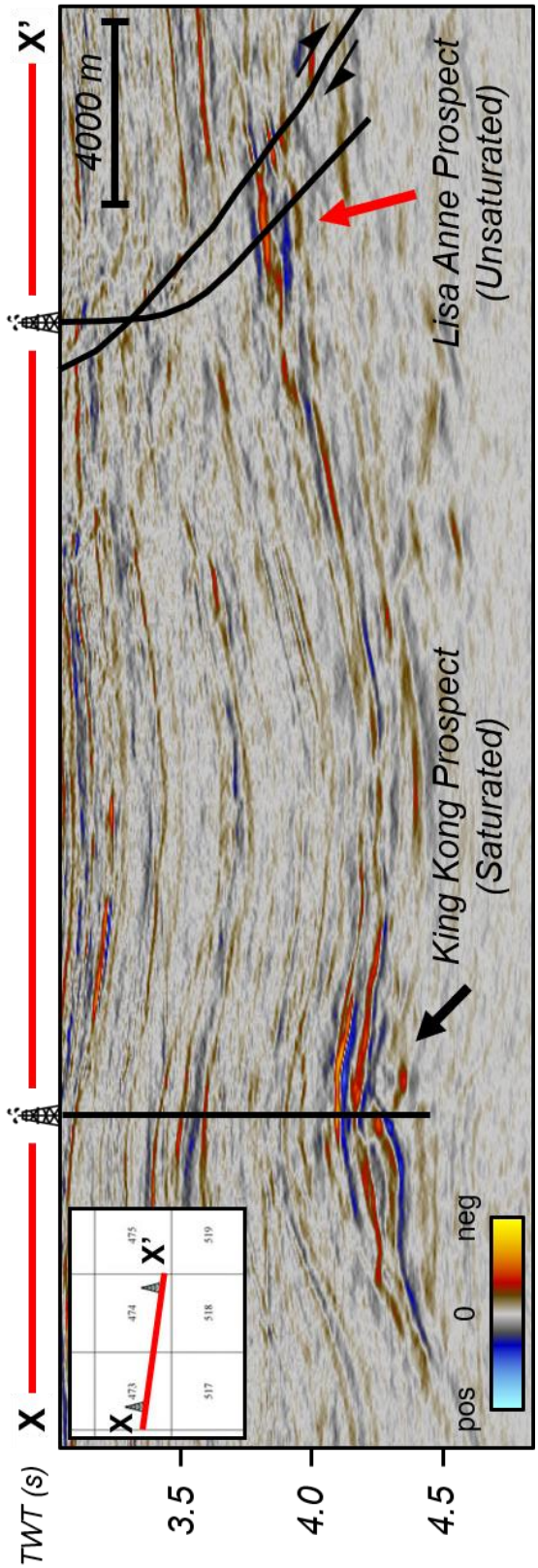

Figure 3-3: Inline 2913 taken through the KK/LA 3D seismic survey across the King Kong and Lisa Anne wells over Green Canyon Block 473 and 474, offshore Gulf of Mexico (modified from O'Brien, 2004).

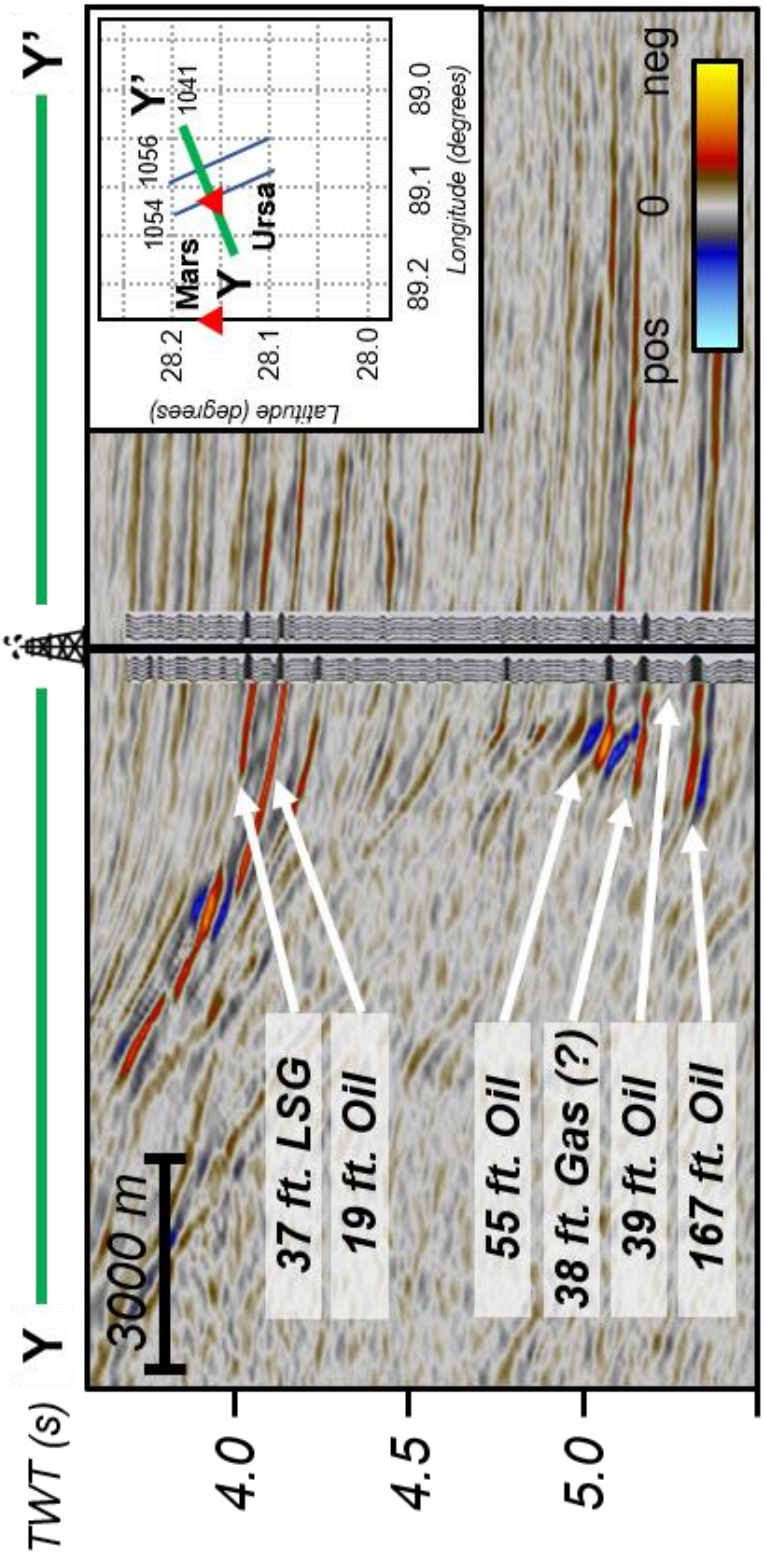

Figure 3-4: Inline 2804 taken through the Ursa Field 3D seismic survey. The hydrocarbon intervals and a synthetic from Hilterman, 2001 are highlighted on the seismic section. Notice how the amplitude for the LSG interval exhibits a similar response to the other hydrocarbon producing intervals (modified after Hilterman, 2001).

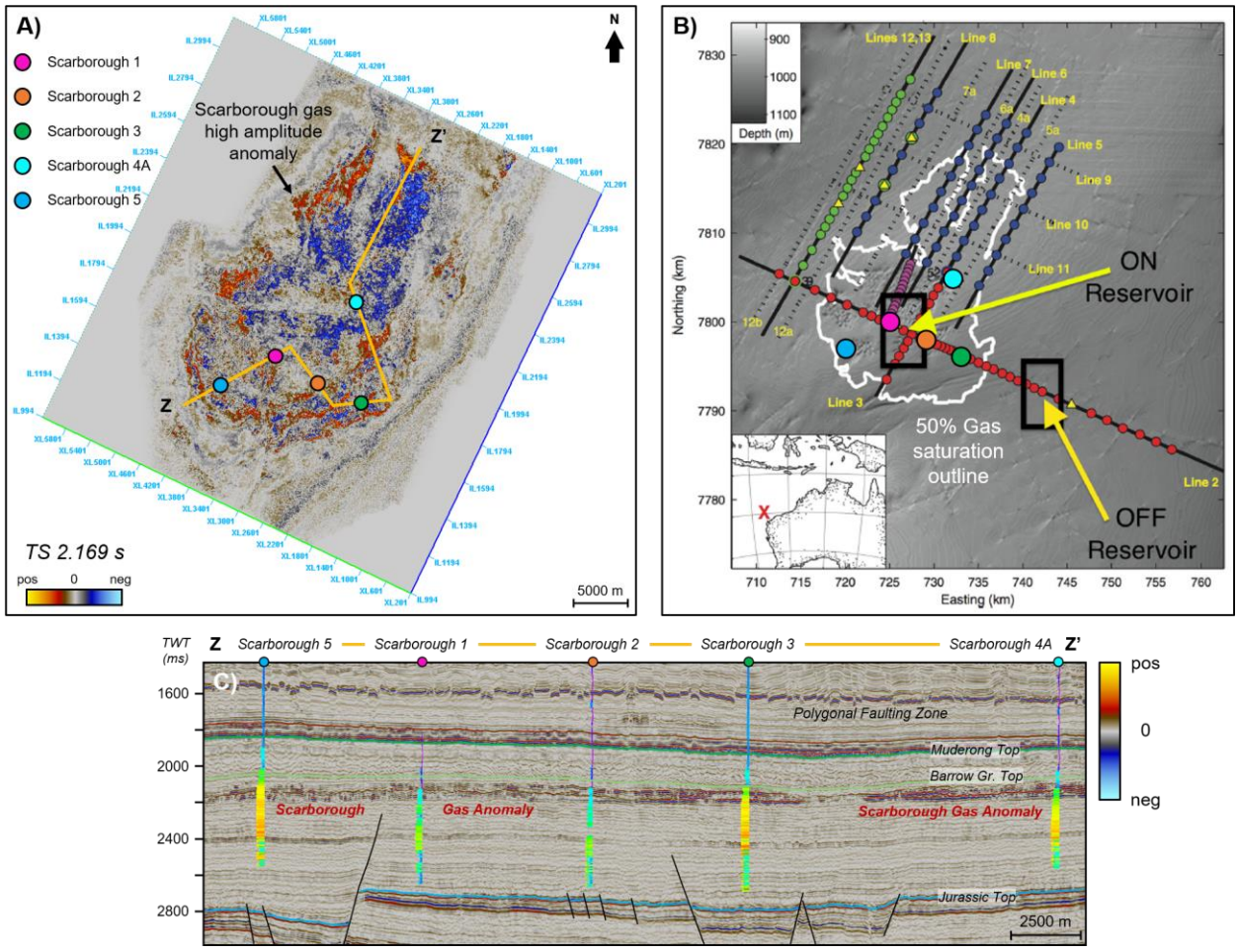

Figure 3-5: A) Horizontal time slice taken at 2.169 s through the Scarborough 3D seismic survey displaying the high amplitude anomaly of the Scarborough gas field. B) CSEM study by Ray et al. (2014) where they defined the 50% gas saturation outline within the Scarborough gas field. C) Interpreted arbitrary seismic section highlighting the Scarborough gas anomaly, key horizons and wells used for this study.

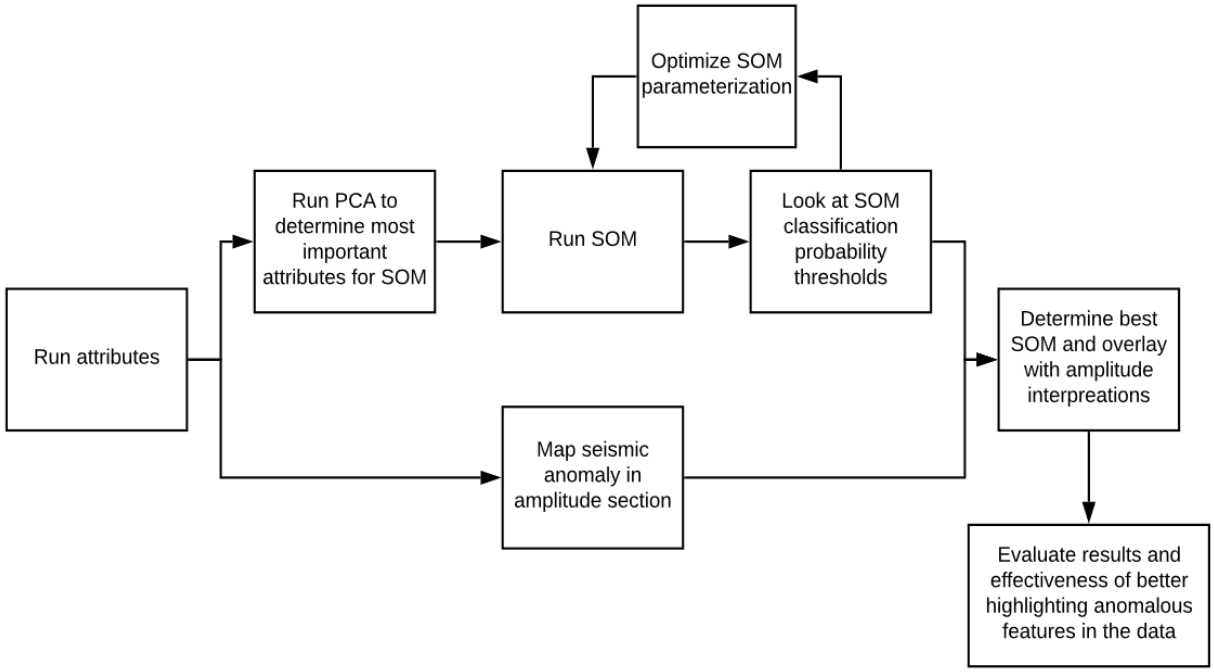

Figure 3-6: Iterative SOM workflow used to evaluate the accuracy and effectiveness of each SOM result. Several combinations of instantaneous attributes and SOM parameters were evaluated.

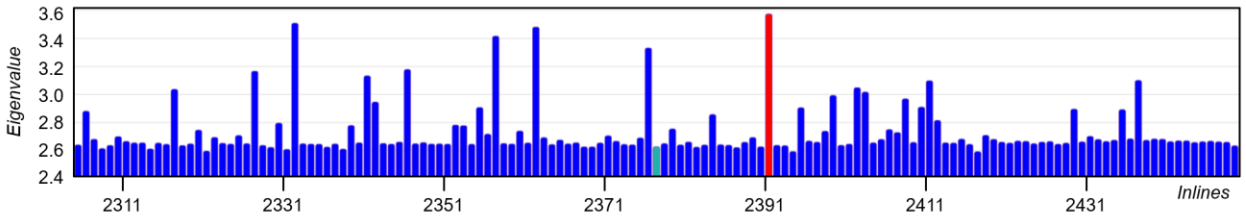

Eigenvalues Chart

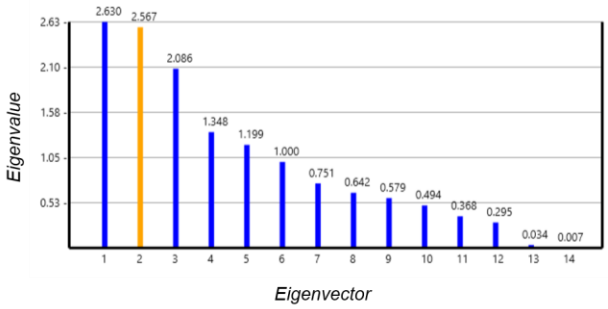

Attributes for Eigenvector 2

Attributes	Percentage	%Total
Sweetness	24.14	62.00
Envelope	22.60	58.04
Attenuation	14.35	36.87
Thin Bed	10.73	27.55
Inst Frequency	10.14	26.06
Envelope Slope	6.83	17.54
Acceleration of Phase	5.72	14.68
Hilbert	2.05	5.27
Amplitude	1.27	3.26
Bandwidth	1.10	2.84
Rel. Acoustic Impedance	0.71	1.83
Inst. Phase	0.31	0.79
Cosine of Phase	0.06	0.14
Inst. Q	0.00	0.00

Attributes for SOM

Attributes	Eigenvector
Sweetness	2
Envelope	2
Rel. AI	3
Hilbert	3
Cos. Phase	4
Amplitude	4

Figure 3-7: PCA results for Inline 2391 of the KKLA 3D seismic survey. The highest-ranking attributes from the first few eigenvectors were chosen to be incorporated into the SOM analysis over the entire dataset. These attributes were envelope, hilbert, the cosine of instantaneous phase, relative acoustic impedance, and sweetness. These attributes were also combined with the full-stack amplitude.

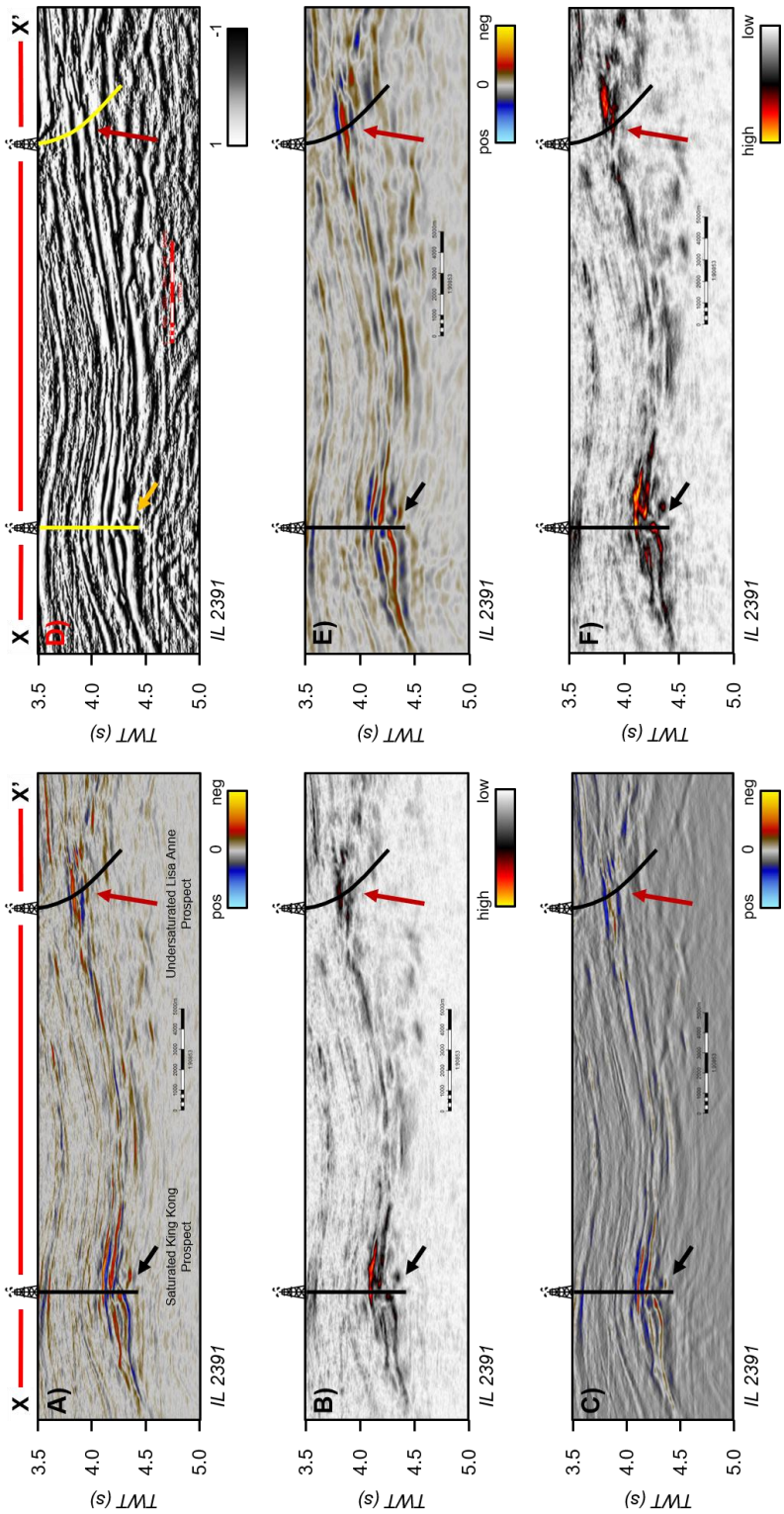

Figure 3-8: All of the attributes from PCA that were used as an input into the KK/LA SOM where A) is the full-stack amplitude B) is the envelope, C) is the Hilbert, D) is the cosine of instantaneous phase, E) is the relative acoustic impedance, and F) is the sweetness. The saturated King Kong Reservoir is shown by the black and orange arrows whereas the undersaturated Lisa Anne prospect is shown by the red arrow.

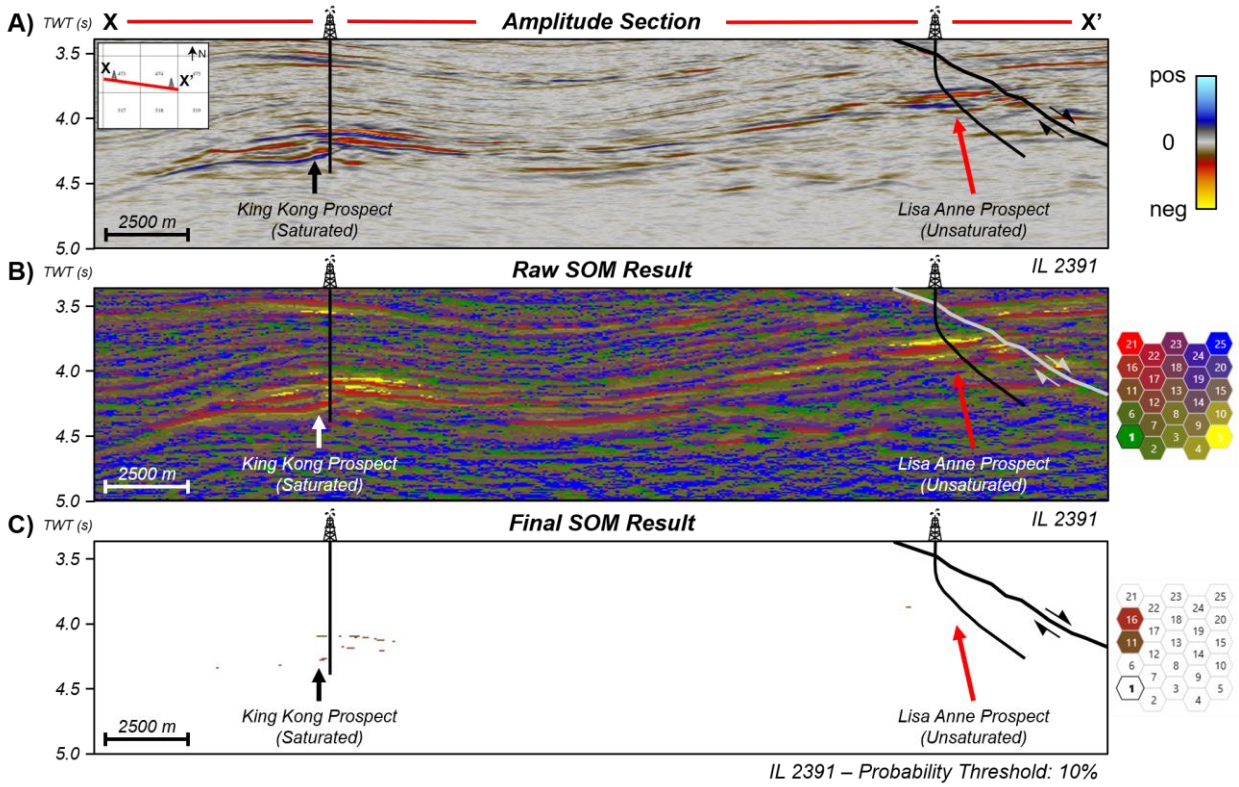

Figure 3-9: A) Post-stack seismic amplitude vertical profile of Inline 2391 illustrating the King Kong and Lisa Anne prospects with B) showing the raw SOM result with all of the neurons displayed. C) Shows the same SOM result with only the neurons of interest displayed with a probability threshold of 10% applied. Here, the SOM marks the top and base of the King Kong prospect (black arrow) while not highlighting the Lisa Anne prospect (red arrow). This demonstrates that the SOM was able to differentiate between a high and low saturation gas reservoir.

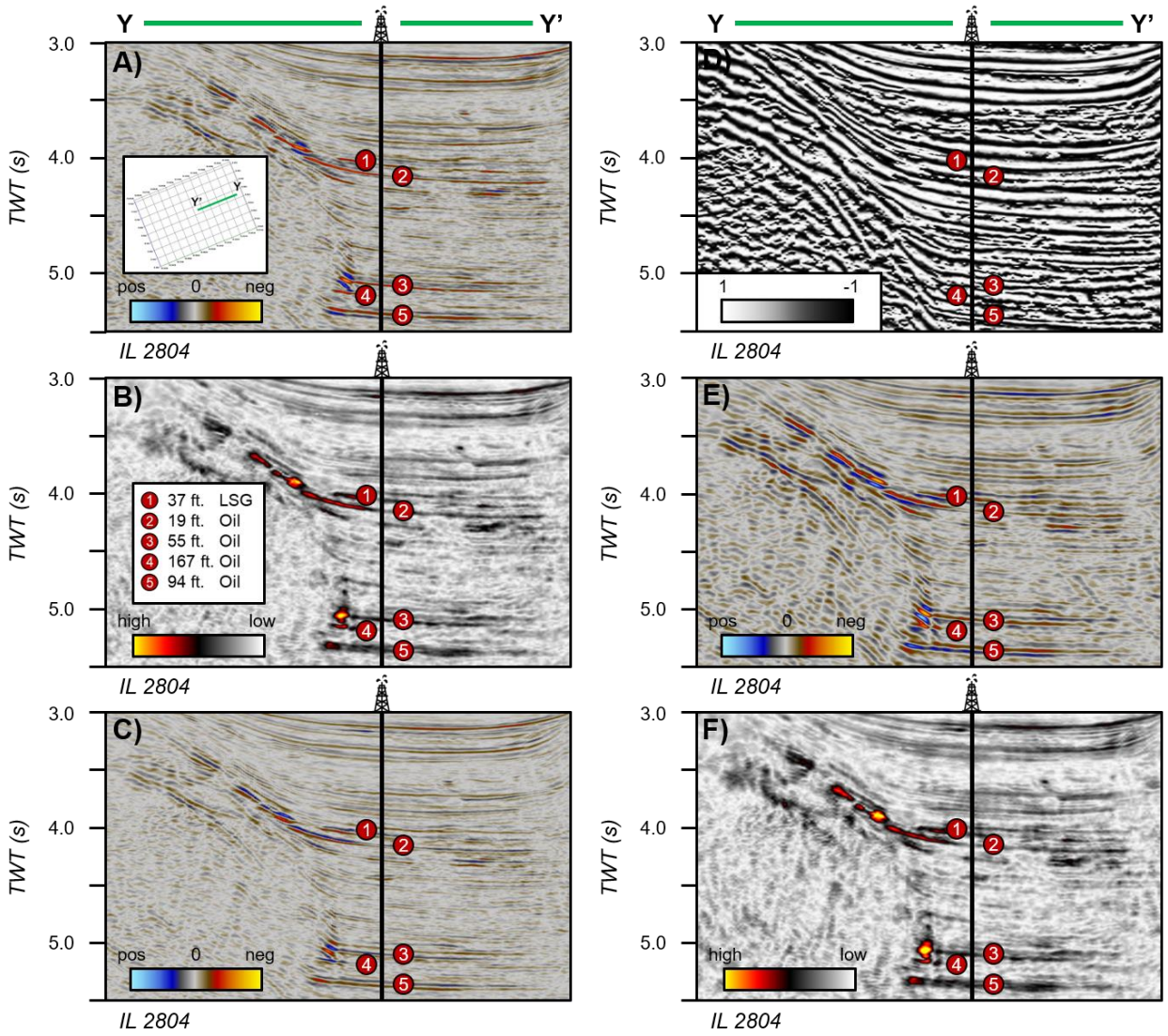

Figure 3-10: All of the attributes from the KK/LA PCA that were used as an input into the Ursa SOM where A) is the full-stack amplitude B) is the envelope, C) is the Hilbert, D) is the cosine of instantaneous phase, E) is the relative acoustic impedance, and F) is the sweetness. The LSG-prone interval is shown by circle 1 whereas the hydrocarbon intervals is shown by circles 2-5. LSG and hydrocarbon intervals modified after Hilterman, 2001.

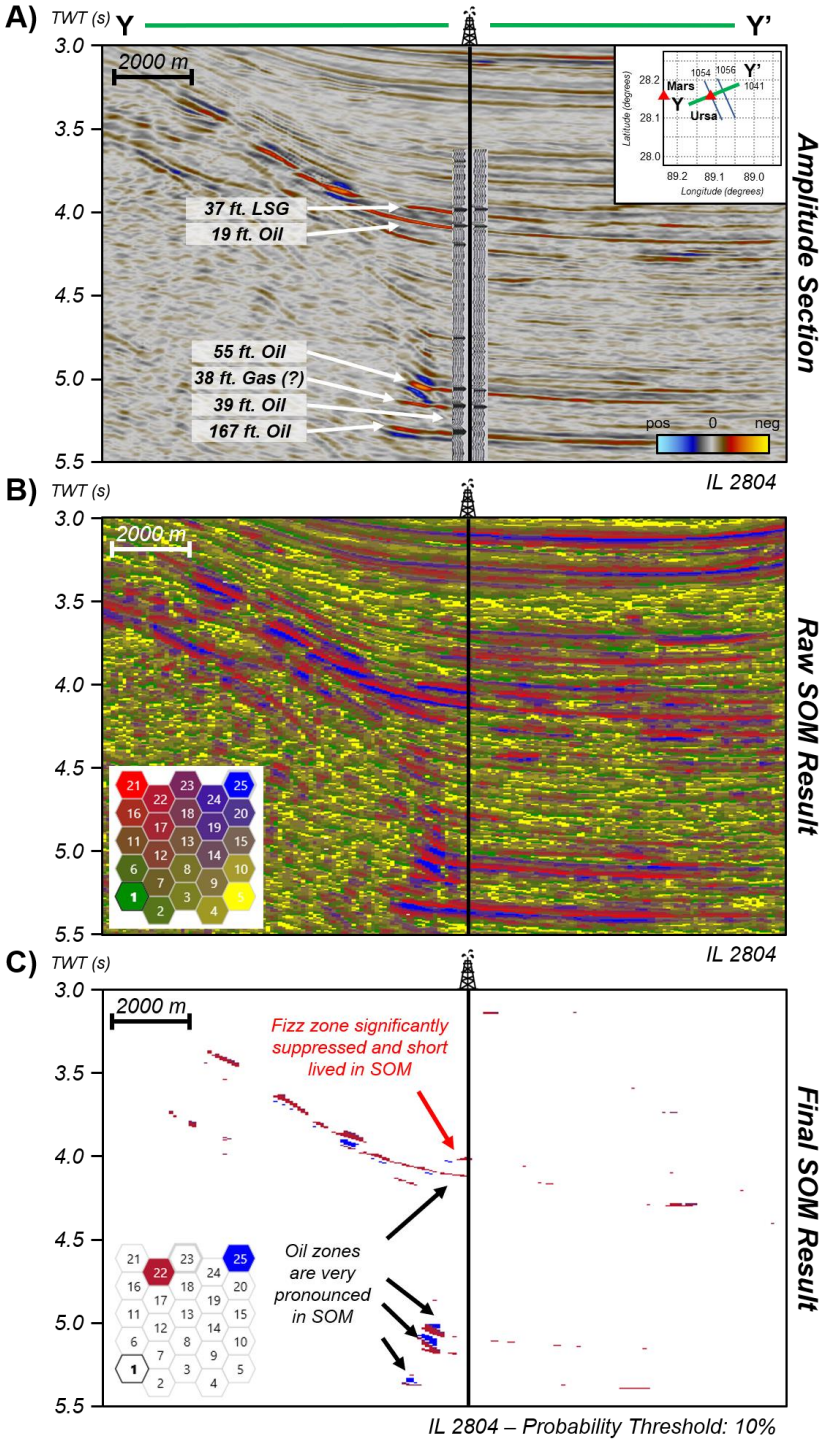

Figure 3-11: A) Post-stack seismic amplitude vertical profile of Inline 2804 illustrating the LSG interval and hydrocarbon intervals within the Ursa gas field whereas B) shows the raw SOM results of that same line. C) Shows the same SOM result with only the neurons of interest displayed with a probability threshold of 10% applied. In this window, the hydrocarbon intervals are better highlighted whereas the LSG interval is significantly suppressed. This demonstrates that the SOM was able to differentiate between a high and low saturation gas reservoir. LSG and hydrocarbon intervals modified after Hilterman, 2001.

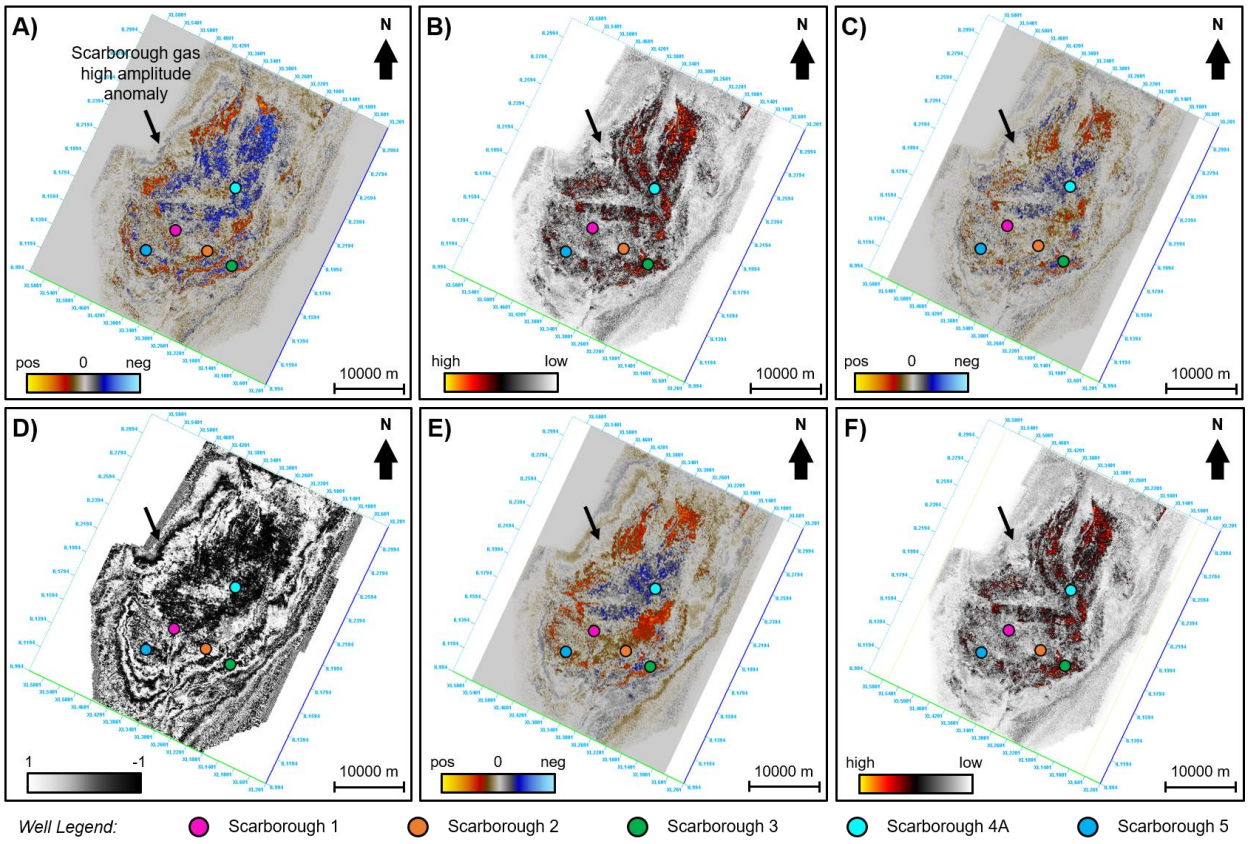

Figure 3-12: All of the attributes taken at time slice 2.169 s from the KK/LA PCA that were used as an input into the Scarborough SOM where A) is the full-stack amplitude B) is the envelope, C) is the Hilbert, D) is the cosine of instantaneous phase, E) is the relative acoustic impedance, and F) is the sweetness.

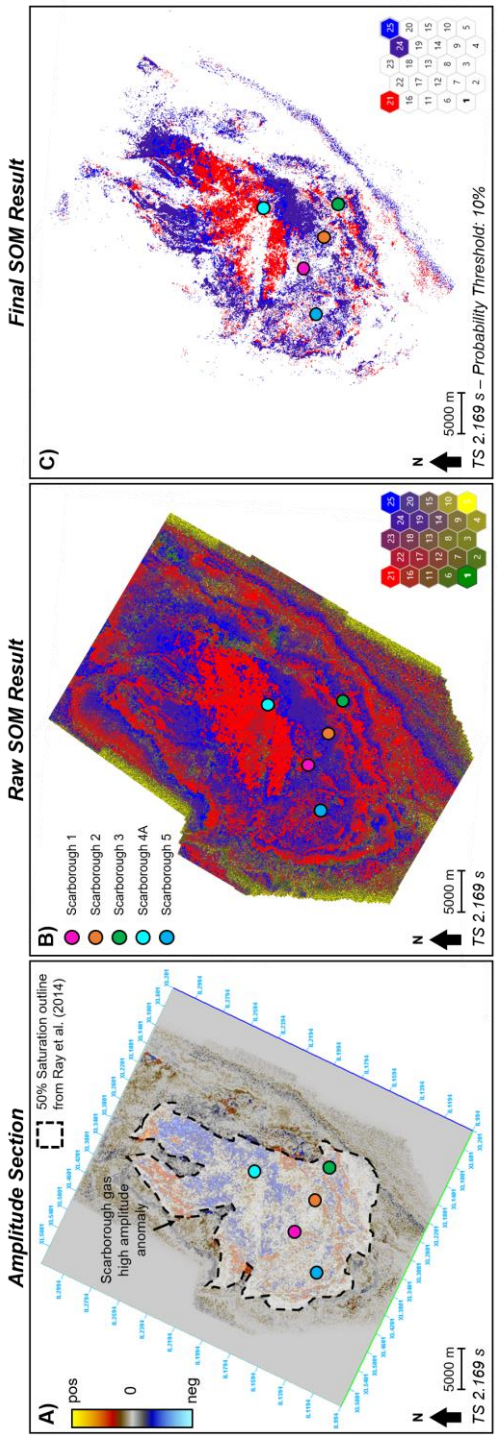

Figure 3-13: A) Post-stack seismic amplitude time slice at 2.169 s illustrating the amplitude anomaly within the Scarborough gas field whereas B) shows the raw SOM results of that same time slice. Shows the same SOM result with only the neurons of interest displayed with a probability threshold of 10% applied. In this view, the entire extent of the gas reservoir is highlighted. This boundary coincides well with Ray et al. (2014)'s 50% saturation line. However, this method proved to be unsuccessful within this survey as it did not give us any qualitative information regarding gas saturation throughout the reservoir.

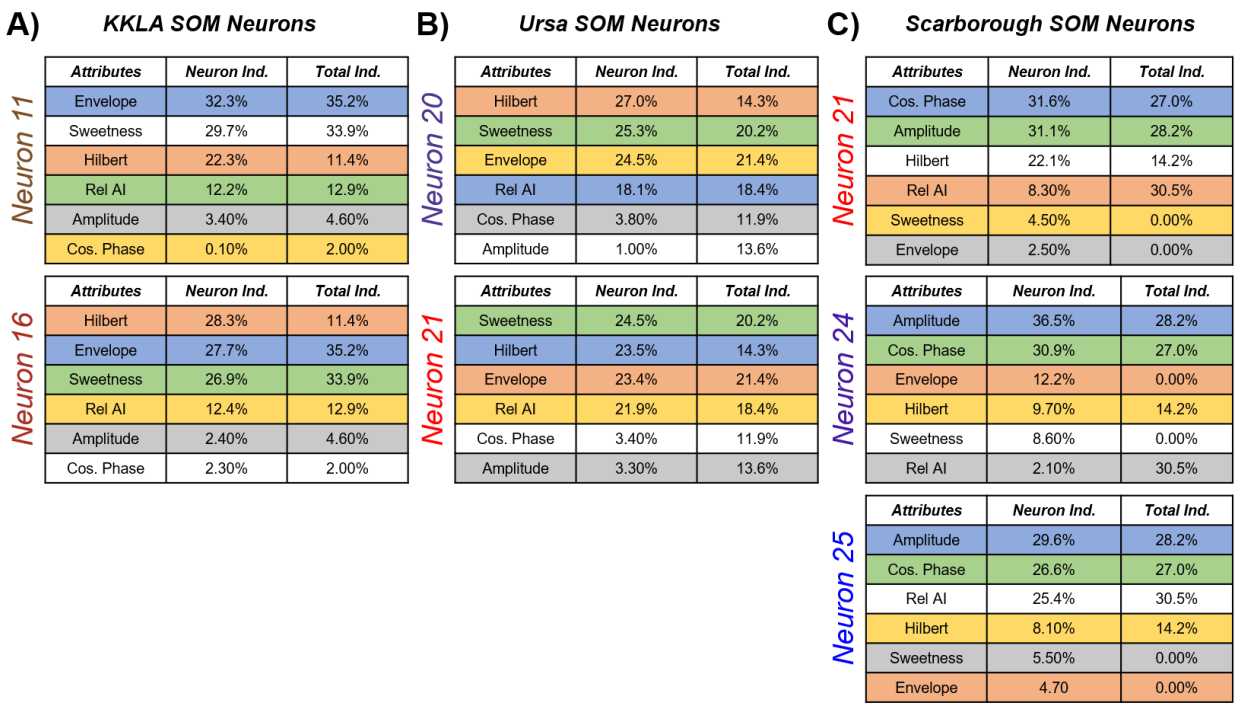

Figure 3-14: Neuron clustering results from A) the KK/LA SOM, B) the Ursa SOM and C) the Scarborough SOM.

TABLES

Instantaneous Attribute Name	*Definition*	*Uses*	*Sources*
Envelope	Calculated from the complex trace to highlight the signal's instantaneous energy.	Instantaneous envelope is useful for highlighting lithology, porosity and hydrocarbons since the attribute is sensitive to subtle changes in acoustic impedance.	Taner et al., 1979; Chopra and Marfurt 2005
Hilbert	90-degree transform/rotation of the seismic trace complex trace.	Useful for highlighting discontinuities, such as faults or lithology changes, and for analyzing AVO anomalies as the attribute is proportional to reflectivity.	
Cosine of Instantaneous Phase	Obtained from taking the cosine of arctangent of the complex trace value divided by the real trace value.	The advantage of using cosine of instantaneous phase as opposed to instantaneous phase is that it is a continuous parameter and does not have a discontinuity at ±180°. This attribute is helpful for detecting unconformities, faults and lateral stratigraphic changes since the attribute tracks reflector continuity. It is also important to note that instantaneous phase is devoid of any amplitude information, therefore, all of the events are represented.	Taner et al., 1979; Taner, 2001; Chopra and Marfurt, 2005
Instantaneous Frequency	Calculated by taking the time derivative of phase.	This attribute is beneficial for analyzing bed thicknesses and for indicating the edges of low impedance thin beds, such as in the case of weak BSRs (Taner et al. 1979; Subrahmanyam and Rao 2008).	Taner et al., 1979; Subrahmanyam and Rao 2008
Relative Acoustic Impedance	Calculated using a running summation on the real trace and applying a high-pass Butterworth filter.	Since the attribute is showing a relative impedance contrast, it can be useful for identifying sequence boundaries, discontinues, and can potentially indicate porosity or fluid content.	Chopra and Marfurt, 2005; Subrahmanyam and Rao, 2008
Sweetness	Computed by dividing the envelope by the square root of instantaneous frequency.	First discovered by Radovich and Oliveros (1998), sweetness is a relative value helpful for determining relative net-to-gross ratios and to identify "sweet spots" in hydrocarbon exploration.	Radovich and Oliveros 1998; Hart 2008; Koson et al., 2014

Table 3-1: Definitions, uses and sources for all of the attributes presented within the LSG study.

Producing Field	*Seismic Survey Name(s)*	*Year*	*Acquisition and Processing*	*Area*	*Data Type*	*Recording Length*	*Sample Interval*	*Polarity*
King Kong/Lisa Anne	G3D201407-02 3D Green Canyon Phase II	1989	Western Geophysical	580 mi^2/1500 km^2	3D post-stack	9.5 s	4 ms	Positive standard
Ursa	G3D1304-002A-C Shell Mississippi Canyon	1988	Shell	480 mi^2/1089 km^2	3D post-stack	9.6 s	4 ms	Positive standard
Scarborough	HEX03A/Scarborough 3D	2004	Western Geophysical	351 mi^2/910 km^2	3D post-stack	6.1 s	2 ms	Negative standard

Table 3-2: Details for all of the seismic surveys used within the LSG study.

REFERENCES

Batzle, M., 2006, Seismic Evaluation of Hydrocarbon Saturation in Deep-Water Reservoirs: Colorado School of Mines, Golden, CO (United States).

Brown, A. R., 2011, Interpretation of Three-Dimensional Seismic Data: Society of Exploration Geophysicists and American Association of Petroleum Geologists.

Castagna, J. P., and M. M. Backus, 1993, Offset-Dependent Reflectivity—Theory and Practice of AVO Analysis: Society of Exploration Geophysicists.

Chopra S., and K. J. Marfurt, 2005, Seismic attributes—A historical perspective: Geophysics, **70**, no. 5, 3SO-28SO.

Chopra, S., and J. P. Castagna, 2014, AVO: Society of Exploration Geophysicists.

Chopra, S., and K. J. Marfurt, 2019, Unsupervised machine learning applications for seismic facies classification: In Unconventional Resources Technology Conference, Denver, Colorado, 22-24 July 2019, 3135-3142.

Driscoll, N. W., and G. D. Karner, 1998, Lower crustal extension across the Northern Carnarvon basin, Australia: Evidence for an eastward dipping detachment: Journal of Geophysical Research: Solid Earth, **103**, no. B3, 4975-4991.

Foschi, M., and J. A. Cartwright, 2020, Seal failure assessment of a major gas field via integration of seal properties and leakage phenomena: AAPG Bulletin, **104**, no. 8, 1627-1648.

Glenton, P. N., J. T. Sutton, J. G. McPherson, M. E. Fittall, M. A. Moore, R. G. Heavysege, and D. Box, 2013, Hierarchical approach to facies and property distribution in a basin-floor fan model, Scarborough Gas Field, North West Shelf, Australia: In IPTC 2013: International Petroleum Technology Conference, cp-350.

Han, D.H. and M. Batzle, 2002, Fizz water and low gas-saturated reservoirs: The Leading Edge, **21**, no. 4, 395-398.

Hilterman, F. J., 2001, Seismic Amplitude Interpretation. Society of Exploration Geophysicists and European Association of Geoscientists and Engineers.

Jolliffe, I.T., 2002, Mathematical and Statistical Properties of Population Principal Components: Principal Component Analysis, 10-28.

Khalid, P., and S. Ghazi, 2013, Discrimination of fizz water and gas reservoir by AVO analysis: a modified approach: Acta Geodaetica et Geophysica, **48**, no. 3, 347-361.

Kohonen, T., 1990, The self-organizing map: Proceedings of the IEEE, **78**, no. 9, 1464-1480.

Laiw, A., 2011, Low Saturation Gas Reservoirs Discrimination – An Integrated Approach: 73rd EAGE Conference and Exhibition.

O'Brien, J., 2004. Seismic amplitudes from low gas saturation sands: The Leading Edge, **23**, no. 12, 1236-1243.

Avseth, P., H. Flesche, and A. J. Van Wijngaarden, 2003, AVO classification of lithology and pore fluids constrained by rock physics depth trends: The Leading Edge, **22**, no. 10, 1004-1011.

Radovich, B. J. and R. B. Oliveros, 1998, 3-D sequence interpretation of seismic instantaneous attributes from the Gorgon field: The Leading Edge, **17**, no. 9, 1286-1293.

Ray, A., K. Key, T. Bodin, D. Myer, and S. Constable, 2014, Bayesian inversion of marine CSEM data from the Scarborough gas field using a transdimensional 2-D parametrization: Geophysical Journal International, **199**, no. 3, 1847-1860.

Roden, R., T. Smith, and D. Sacrey, 2015, Geologic pattern recognition from seismic attributes: Principal component analysis and self-organizing maps: Interpretation, **3**, no. 4, SAE59-SAE83.

Roden, R., T. A. Smith, P. Santogrossi, D. Sacrey, and G. Jones, 2017, Seismic interpretation below tuning with multiattribute analysis: The Leading Edge, **36**, no. 4, 330-339.

Roden, R., and C. W. Chen, 2017, Interpretation of DHI characteristics with machine learning: First Break, **35**, no. 5.

Sacrey, D., and R. Roden, 2014, Understanding Attributes and Their Use in the Application of Neural Analysis–Case Histories Both Conventional and Unconventional: Search and Discovery Article, 41473.

Subrahmanyam, D., and P. H. Rao, 2008, Seismic attributes–A review: In 7th international conference & exposition on petroleum geophysics, Hyderabad, 398-404.

Taner, M. T., F. Koehler, and R. E. Sheriff, 1979, Complex seismic trace analysis: Geophysics, **44**, no. 6, 1041-1063.

Taner, M. T., 2001, Seismic attributes: CSEG Recorder, **26**, no. 7, 49-56.

Veeken, P. C., 2006, Seismic Stratigraphy, Basin Analysis and Reservoir Characterization: Elsevier, Boston, MA.

Wojcik, K. M., E. Gonzalez, and R. E. Vines, 2016, Derisking low-saturation gas in Tertiary turbidite reservoirs: Interpretation, **4**, no. 3, SN31-SN43.

Wu, X., M. Chapman, X. Y. Li, and P. Boston, 2014, Quantitative gas saturation estimation by frequency-dependent amplitude-versus-offset analysis: Geophysical Prospecting, **62**, no. 6, 1224-1237.

Zhou, Z., and F. J. Hilterman, 2010, A comparison between methods that discriminate fluid content in unconsolidated sandstone reservoirs: Geophysics, **75**, no. 1, B47-B58.

Zhu, F., 2000, Shear-Wave Velocity Estimation using Multiple Logs and Multicomponent Seismic AVO Interpretation: Gulf of Thailand.

APPENDIX A

Initial KK/LA SOM Results and Final KK/LA SOM Results

This appendix shows the difference between the initial SOM for the KK/LA survey. The initial SOM was trained for 50 iterations, used 36 neurons with the full-stack amplitude and with the following combination of instantaneous attributes: acceleration of phase, attenuation, bandwidth, envelope, envelope slope, and instantaneous Q (Appendix A, Figures 1d-e). These attributes were selected from the initial PCA results. Notice how the initial SOM was also computed over a larger portion of the survey from 1.5 s to 5.5 s. The final SOM was trained for 50 iterations, used 25 neurons with the full-stack amplitude and used the following combination of instantaneous attributes: envelope, Hilbert, cosine of instantaneous phase, relative acoustic impedance and sweetness (Appendix A, Figures 1b-c). The final SOM was also computed over a smaller interval from 3.4 s to 5.0 s. The smaller interval of the final SOM allows the algorithm to focus on the anomalous features rather than some of the other more common features found throughout the survey, such as continuous geology or faults. Note that while the King Kong prospect is relatively well highlighted, the Lisa Anne prospect is not as well suppressed in the initial SOM compared to the final optimized SOM (Appendix A, Figures 1b-e). The improvement in the SOM results can be directly attributed to a better combination of attributes, a smaller number of neurons and a smaller computation interval.

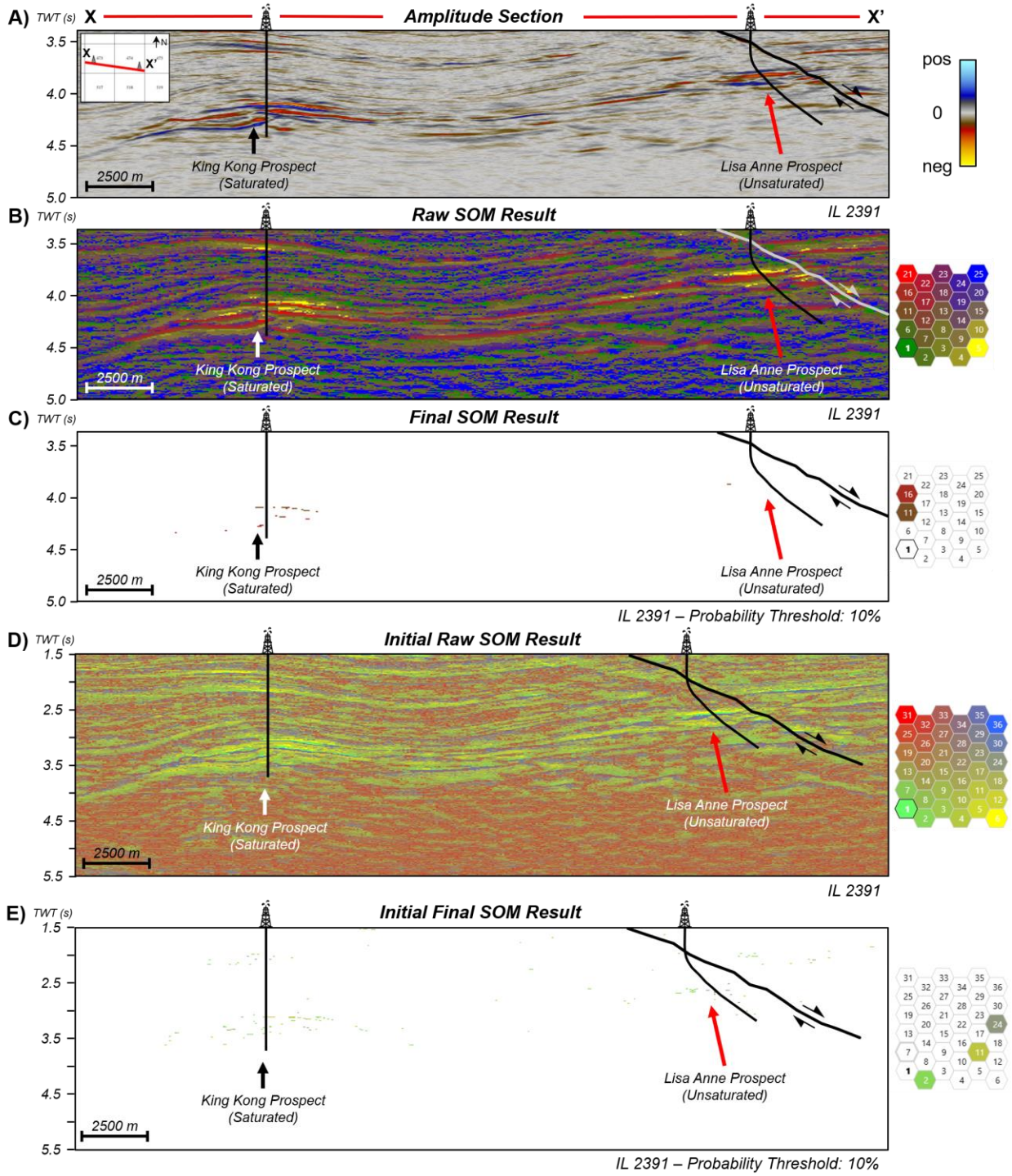

Appendix A, Figure 1: A) Post-stack seismic amplitude vertical profile of Inline 2391 illustrating the King Kong and Lisa Anne prospects with B) showing the raw SOM result with all of the neurons displayed. C) Shows the same SOM result with only the neurons of interest displayed with a probability threshold of 10% applied. D) Shows the initial raw SOM results whereas E) highlights the interpreted initial SOM results with a probability threshold of 10% applied. Note the improvement in the results from the initial SOMs in D and E compared to the optimized SOM in B and C.

CHAPTER 4: Conclusions

Throughout this thesis, I applied and evaluated PCA and SOMs for better characterizing gas in the subsurface. Individually, some of these attributes have minimal success in identifying the seismically transparent hydrates or differentiating between HSG and LSG. However, employing a multi-attribute analysis provides clearer insight and confidence into the identification and distribution of gas hydrates as well as discriminating between HSG and LSG. While the method proved to be transferrable for imaging strong and weak BSRs, it was not as readily transferrable when discriminating between HSG and LSG. This suggests that each SOM model should be optimized for each imaging goal.

In Chapter 2, I further characterized the presence of hydrates in the subsurface by improving the detection of weak BSRs. This was accomplished by using PCA to select the most optimal attributes to be incorporated into the SOM. Once this was done, I then evaluated the optimal hyperparameters for the SOM, such as neuron count, number of attributes and epochs. This was done to ensure computational efficiency while maximizing the imaging capabilities of both strong and weak BSRs. Additionally, we evaluated the transferability of this method by applying the SOM on a different seismic survey within the Pegasus Basin. I was able to confirm the same strong and weak BSRs in both surveys, further proving the transferability of this method. From these studies, I found that both types of BSRs are better identified when using instantaneous attributes such as instantaneous frequency, sweetness and thin bed, which compliment AVA attributes such as gas indicator and fluid factor.

In Chapter 3, I evaluated the viability of using this proposed method for distinguishing between HSG and LSG within two 3D seismic surveys within the deepwater Gulf of Mexico and within another 3D seismic survey within the Carnarvon Basin, offshore Australia. This

methodology was successful within the deepwater Gulf of Mexico, however, yielded limited results within the Carnarvon Basin. This could only be accomplished by looking at various probability thresholds within the clustering results. By using this probability cutoff, the SOM is displaying the highly anomalous data points that had a 10% chance of being grouped within that neuron. Therefore, these anomalous data points are displaying the anomalous amplitude responses. My neuron analysis also revealed that some attributes represented 0% of the Scarborough gas field's independent variability. This suggests that the SOM models are only optimized for the within the Gulf of Mexico, as was noted within the KK/LA and Ursa fields, whereas a new combination of attributes is required for the Carnarvon Basin.

Supplementary research will focus on applying obtaining well information and any other data types to better understand the SOM cluster results. This will provide a better understanding of the geology, further highlighting possible relationships with the geophysical properties of the prospects. Additional work will also optimize the Scarborough SOM to identify potential favorable drilling locations based on anomalous SOM clustering. Also, further research will incorporate containment analysis to better understand the sealing behavior of these LSG reservoirs. Finally, future work will also extend these methods into other basins around the globe, such as other LSG prone regions to test the viability of this method as a universal technique.

Future research could also focus on evaluating the hydrate SOM workflow within permafrost regions. Many hydrate accumulations are located in permafrost regions, with some of the most prominent situated in Northern Alaska and at the Mallik Site in Northwestern Canada (Riedel et al., 2010). My research focused solely on hydrates located in marine settings which has a significantly different depth and pressure regime for the gas hydrate stability zone when compared to permafrost regions (Riedel et al., 2010). Therefore, would the same SOM workflow

apply for characterizing weak BSRs in permafrost regions? Or would the SOM need to be optimized for this different geothermal regime? This would make for an interesting study to evaluate the possible limitations for the hydrate SOM. Furthermore, while these methods have only been tested in specific regions for characterizing anomalous amplitude responses, they could show promise for other seismic classification applications. There have been several studies that have shown the promise of using SOMs for classifying seismic facies in various basins globally (Roy et al., 2013; Zhao et al., 2016; Lubo-Robles et al., 2017; Ha et al., 2019). Finally, how would other supervised and unsupervised machine learning algorithms compare to the SOM results. There are many other algorithms that may be more robust than SOMs, such as probabilistic neural networks and generative topographic maps, that could further improve my presented results (Roy et al., 2014; Zhao et al., 2015b; Lubo et al., 2019).

Finally, other unsupervised, machine learning algorithms may be more effective for better characterizing the anomalous amplitudes presented within both studies. Chopra and Marfurt (2018) noted that SOMs have several limitations. There is no theoretical basis for selecting the optimal training radius, neighborhood function, and learning rate as these hyperparameters are data dependent (Chopra and Marfurt, 2018). Therefore, these hyperparameters will be different for each dataset. Furthermore, there is no cost function. This function could be iteratively minimized to determine the point at which the iterations converge during the classification process, thus indicating the optimal number of iterations for the SOM to run (Chopra and Marfurt, 2018). However, generative topographic mapping (GTM) overcomes these limitations. GTM, is another nonlinear, dimensionality reduction technique that also provides a probabilistic representation of the data vectors in latent space (Chopra and Marfurt, 2018). While SOMs seek the cluster that is closest to a given data point, GTM will also provide some mathematical support for that data point

belonging to that cluster (Zhao et al., 2015b). Therefore, GTM outputs probability estimates of how similar or different and cluster is to attribute behavior (Zhao et al., 2015b). Finally, another unsupervised, machine learning algorithm that could be used are gaussian mixture models (GMMs). Similar to GTM, GMMs overcome several of the SOM limitations since GMMs are parametric models of probability distributions that provide better flexibility and precision in modelling when compared to traditional, unsupervised clustering algorithms (Lubo et al., 2014; Zhao et al., 2015b).

REFERENCES

Chopra, S., and K. J. Marfurt, 2018, Seismic facies classification using some unsupervised machine learning methods. In SEG Technical Program Expanded Abstracts 2018, 2056-2060.

Ha, T. N., K. J. Marfurt, B. C. Wallet, and B. Hutchinson, 2019, Pitfalls and implementation of data conditioning, attribute analysis, and self-organizing maps to 2D data: Application to the Exmouth Plateau, North Carnarvon Basin, Australia: Interpretation, **7**, no. 3, SG23-SG42.

Lubo-Robles, D., T. Ha, S. Lakshmivarahan, and K. J. Marfurt, 2019, Supervised seismic facies classification using Probabilistic Neural Networks: Which attributes should the interpreter use? In SEG Technical Program Expanded Abstracts 2019, 2273-2277.

Lubo-Robles, D., and K. J. Marfurt, 2017, Delineation of thick incised canyons using spectral-decomposition analysis, curvature and Self-Organizing Maps in the Exmouth Plateau, Australia: In SEG Technical Program Expanded Abstracts 2017, 2420-2424.

Lubo-Robles, D., K. J. Marfurt, and V. Jayaram, 2014, Statistical characterization and geological correlation of wells using automatic learning Gaussian mixture models. In Unconventional Resources Technology Conference 2014, 774-783.

Riedel, M., E. C. Willoughby, and S. Chopra, 2010, Geophysical Characterization of Gas Hydrates. Society of Exploration Geophysicists.

Roy, A., A. S. Romero-Peláez, T. J. Kwiatkowski, and K. J. Marfurt, 2014, Generative topographic mapping for seismic facies estimation of a carbonate wash, Veracruz Basin, southern Mexico: Interpretation, **2**, no. 1, SA31-SA47.

Roy, A., B. Dowdell, and K. J. Marfurt, 2013, Characterizing a Mississippian tripolitic chert reservoir using 3D unsupervised and supervised multiattribute seismic facies analysis: An example from Osage County, Oklahoma: Interpretation, **1**, no. 2, SB109-SB124.

Zhao, T., J. Zhang, F. Li, and K. J. Marfurt, 2016, Characterizing a turbidite system in Canterbury Basin, New Zealand, using seismic attributes and distance-preserving self-organizing maps: Interpretation, **4**, no. 1, SB79-SB89.

Zhao, T., V. Jayaram, A. Roy, and K. J. Marfurt, 2015b, A comparison of classification techniques for seismic facies recognition: Interpretation, **3**, no. 4, 29-58.